SECURITY INFORMATION

CONFIDENTIAL

Copy 209
RM L52G01

RESEARCH MEMORANDUM

AN INVESTIGATION OF SEVERAL SUPERSONIC MISSILE CONFIGURATIONS DIRECTED TOWARD MINIMIZING CENTER-OF-PRESSURE TRAVEL

By Robert W. Rainey

Langley Aeronautical Laboratory
Langley Field, Va.

CLASSIFIED DOCUMENT

This material contains information affecting the National Defense of the United States within the meaning of the espionage laws, Title 18, U.S.C., Secs. 793 and 794, the transmission or revelation of which in any manner to unauthorized person is prohibited by law.

NATIONAL ADVISORY COMMITTEE
FOR AERONAUTICS

WASHINGTON
September 23, 1952

CONFIDENTIAL

NATIONAL ADVISORY COMMITTEE FOR AERONAUTICS

RESEARCH MEMORANDUM

AN INVESTIGATION OF SEVERAL SUPERSONIC MISSILE CONFIGURATIONS DIRECTED TOWARD MINIMIZING CENTER-OF-PRESSURE TRAVEL

By Robert W. Rainey

SUMMARY

An investigation was made in the Langley 9-inch supersonic tunnel of several missiles having low-aspect-ratio, cruciform, tandem lifting surfaces with a view toward developing a missile with small variations of center-of-pressure location at various angles of attack and roll. The investigation centered about a basic configuration having equal-span wings and tails. Modifications were introduced in an attempt to determine the magnitude of the wing-tail interference and to minimize the undesirable effects of this interference.

Presented are summaries of the lift, drag, and pitching-moment results and analyses of these results in the form of tail efficiencies or center-of-pressure shifts or both of the missile configurations and various components and combinations of components tested. The angle-of-attack range was from -5° to 15°. The Mach number range was from 1.62 to 2.40, most of the data being obtained at a Mach number of 1.93.

A method of calculating the effects of wing-tail interference upon the lift and pitching moments of missiles is presented and the calculated results are generally in good agreement with the experimental results.

INTRODUCTION

One of the problems encountered in the development of supersonic air-to-air missiles with low-aspect-ratio, cruciform, tandem lifting surfaces is the effects of wing-tail interference upon the static longitudinal stability of the missile. The predominant interference effect is associated with the changes in the induced flow field at the tail with angle of attack which cause nonlinear changes in the resultant

downwash over the tail surfaces. These nonlinearities result in shifts in the location of the missile center of pressure which, in the case of a guided missile, can add prohibitive complications to the control systems.

An experimental investigation has been made in the Langley 9-inch supersonic tunnel to determine the effects of wing-tail interference upon the static longitudinal stability of various missile configurations in the Mach number range of 1.62 and 2.40 at corresponding Reynolds numbers of 0.362×10^6 to 0.262×10^6 per inch. The tests were made in an attempt to develop a missile with little center-of-pressure travel due to changes in angle of attack, roll, and Mach number starting with a basic configuration having equal-span wings and tails and modifying this configuration in order to reduce the interference effects. In order to evaluate the wing-tail interference effects, it is essential to know the aerodynamic characteristics of the body-alone, body-wing, and body-tail combinations, as well as the characteristics of the complete configuration. The data for these various combinations in the present investigation were obtained experimentally and were presented in references 1, 2, and 3. In the present paper a representative part of the experimental data is summarized and analyzed. Also, comparison is made between the experimental wing-tail interference effects and those calculated by use of a method presented in this paper.

SYMBOLS

b	total span of wing
b_t	total span of tail
B	configuration of body
BW	configuration of body and wings
BT	configuration of body and tails
BWT	configuration of body, wings, and tails
C_D	drag coefficient, Drag/qS
$C_{D_{min}}$	minimum drag coefficient
C_L	lift coefficient, Lift/qS

C_{L_α}	variation of C_L with $\alpha\left(\partial C_L/\partial\alpha\right)$
$\left(C_{L_\alpha}\right)_0$	C_{L_α} at $\alpha = 0^\circ$
C_m	pitching-moment coefficient, moments taken about center of gravity, see fig. 1, Pitching moment/qSd
C_{m_α}	variation of C_m with $\alpha(\partial C_m/\partial\alpha)$
$\left(C_{m_\alpha}\right)_0$	C_{m_α} at $\alpha = 0^\circ$
d	maximum body diameter
M	Mach number
q	dynamic pressure
r	body radius
S	maximum body cross-sectional area
t/c	thickness ratio of wing or tail
U	free-stream velocity
α	angle of attack
ϕ	angle of roll of model relative to angle-of-attack plane, positive when model, viewed from rear, is rotated clockwise ($\phi = 0^\circ$ when opposite tail panels are in angle-of-attack plane)
θ	interdigitation angle, angle between a plane through opposite tail panels and a plane through opposite wing panels, positive when wings are rotated clockwise with respect to tails as viewed from the rear. (When θ values are indicated for BW configurations, the subtracted tail is assumed to be present at $\phi = 0^\circ$.)
η_t	tail efficiency calculated using lift data, $\dfrac{C_{L_{BWT}} - C_{L_{BW}}}{C_{L_{BT}} - C_{L_B}}$
ρ	free-stream density

[redacted]

Subscripts:

R root of wing or tail panel

T tip of wing or tail panel

Numerical subscripts of configuration designations refer to particular body, wing, or tail.

Superscripts:

Numerical superscript of W gives value of interdigitation angle θ.

APPARATUS AND TESTS

Wind Tunnel

All tests were made in the Langley 9-inch supersonic tunnel. The tunnel is of the continuous-operation complete-return type in which the stream pressure, temperature, and humidity conditions may be controlled. The air was dried sufficiently at the start of each test so that the condensation effects in the test section were negligible. Within the stagnation chamber ahead of the first minimum are located 11 fine-mesh turbulence-damping screens. The Mach number is varied by interchanging nozzle blocks which form test sections approximately 9 inches square. A schlieren system is provided for qualitative visual-flow observations.

Model Description and Installation

The dimensions and designations of the various models tested are given in figure 1 along with pertinent descriptions of each component. All models, with the exception of the solid-body models, were designed so that the various wing and tail surfaces of the complete configurations could be interchanged, varied in position with respect to each other, or omitted entirely. Body length could be varied by inserting or removing sections in the cylindrical part of the body. Also, nose shapes could be interchanged. In general, the models were found to have been constructed to within ± 0.002 inch of the dimensions indicated in figure 1 with the exception of the cylindrical part of the body which was found to be accurate within ± 0.0003 inch of the designated dimensions.

A schematic drawing of the model installation in the tunnel is shown in figure 2. The model moment reference was adjusted laterally at each test angle of attack so that the reference would be on the axis of the tunnel. It is seen in figure 2 from the estimated limits of the

critical disturbance due to the model and its reflections that with the system employed — in which the effective center of rotation of the model may be selected — the axis of the body tends to stay symmetrically boxed-in by these disturbances without interference. In this way, the longest possible model for a given tunnel width and Mach number may be employed.

All models were sting mounted with a movable windshield that enveloped the sting and faired into the rear of the model with a gap of about 0.015 inch between the rear of the model and the front of the windshield. (See fig. 3.) Before each set of readings was taken at a given angle of attack, the gap between the stern of the model and the movable windshield was carefully adjusted so that a constant opening around the periphery existed. The pressure inside the box enclosing the balances and sting was held approximately constant and just below stream static pressure during each test except when effects of box pressure variation were investigated.

Tests

It was noted during the early part of the test program that, for a clean body configuration, a displacement of the pitching-moment curve at $\alpha = 0^\circ$ was experienced that was larger than at the beginning of the program. It was found that an internal taper at the stern of the body would remove the largest part of the displacement; therefore, all the remaining configurations tested had an internal taper at the stern. Those configurations tested without the tapered stern included $B_2W_1^{45}$, B_2T_1, and $B_2W_1^{45}T_1$ at $M = 2.40$.

It was also noted during the early part of the tests that the elevator settings of the tail T_1, although intended to be constant and at a value near 0°, varied somewhat during the course of testing and changed slightly every time the model was disassembled and reassembled. This variation resulted in increments of lift and pitching moment at zero angle of attack; therefore, during all tests except B_2T_1 and $B_2W_1^{45}T_1$ at $M = 2.40$, the elevators were soldered fixed to the tail panels.

During the tests the effects of varying the box pressure and gap were investigated and it was found that for the gap setting used (0.015 inch) the box pressure could be varied several percent above or below the stream static pressure without affecting the model lift and pitching-moment characteristics. With regard to the drag, the fore drag of each configuration was found to be independent of box pressure and the base pressure was found to be equal to the box pressure. All drag results presented herein were corrected to free-stream base pressure.

During the body-alone B_2 test at $M = 2.40$, it was noted that small protuberances affected the measured characteristics. The protuberance referred to was a flat $\frac{1}{16}$-inch-diameter mirror mounted near the moment reference. (See ref. 1.) Results of other tests (not presented) in which small protuberances were intentionally placed on alternate sides of the body and at different longitudinal stations along the body showed that the asymmetry in the drag curves reversed when the protuberance was placed on alternate sides of the body and that the magnitude of the asymmetry decreased as the protuberance was placed nearer the base of the model. These observations indicated that the change in the character of flow over the body due to small protuberances was sufficient to change the measured characteristics. Other body-alone tests reported in reference 2 further substantiated this conclusion; therefore, solid models of B_2, B_3, and B_4 were constructed with surfaces free of waviness and protuberances for use in body-alone tests. Since larger "protuberances," such as wings, were expected to change the character of flow over the after portions of the body, tests were made of B_2, B_3, and B_4 with transition induced by rings that were installed in the region where the various wings were installed. Each ring was composed of fine salt crystals sparsely distributed in a single layer over a width of about 1/8 inch and a thickness of about 0.013 inch (1.6 percent diameter). The results of these tests are believed to give an indication of the effects of the change in flow character due to the installation of wings upon the characteristics of the body.

PRECISION OF DATA

For all the test Mach numbers, pressure surveys throughout the test section have shown the stream to be uniform within a maximum variation in Mach number of ± 0.01. Less detailed angle surveys have indicated flow deviations of the order of 0.15° or less with respect to the tunnel walls and, also, from past experience, both zero moment and zero lift are generally realized for symmetrical configurations at zero angle of attack. These points are brought out to emphasize the fact that, for the present tests, the most likely reason for an extraneous moment or lift at zero angle of attack is a misalined (other than zero angle with respect to the body axis) wing or tail panel. Measurements of the various wings and tails indicated that inadvertent incidences are present.

All the lifts, drags, and pitching moments were measured by means of external self-balancing mechanical scales. A conservative estimate

of the maximum probable errors in these measurements is given in the following table:

Coefficient \ Mach number	1.62	1.93	2.40
C_L	±0.001	±0.001	±0.001
C_D	±.003	±.003	±.004
C_m	±.013	±.014	±.020

Angles of attack with respect to each other in a given run are accurate to within ±0.01°. The errors in initially referencing the body axis parallel to the tunnel wall do not exceed ±0.03°.

RESULTS AND DISCUSSION

Presented in figures 4 to 15 are the lift, drag, and pitching-moment measurements of the configurations investigated grouped according to Mach number, first $M = 1.93$ at which most of the tests were made, then $M = 1.62$ and $M = 2.40$. In figures 16 to 23 are presented the center-of-pressure locations for B, BW, BT, and BWT and the tail efficiencies for BWT followed, in figures 24 to 28, by comparisons of predicted and experimental results. All these results, as well as the discussions of the results, are presented in order of model build-up, first body-alone, then body-wing, body-tail, and body-wing-tail.

The experimental values of $(C_{L_\alpha})_0$, $(C_{m_\alpha})_0$, and $C_{D_{min}}$ as well as the numbers of the figures presenting measured data are summarized in table I.

Body

The results of body-alone tests are presented in figures 4, 8, and 12 and compared with theories of references 4, 5, and 6 in figure 24.

Lift.- The experimental curves at $M = 1.93$ (fig. 4(a)) indicate that the effects on C_{L_α} of increasing the fineness ratio of a body with the same conical nose from 10.0 to 11.4 are negligible at values of α less than 5°, which indicates that the majority of the lift was

contributed by the nose at small angles of attack as has been predicted. Also, the effects on C_{L_α} of inducing transition about the region of the model behind the nose are small for values of α less than 6° (for example, fig. 4(c)). At higher angles of attack, C_{L_α} increased with α for each body length; also, at a constant α above 6° the lift contributed by the afterbody increased with the length of the afterbody. It was also found that, as transition was induced farther forward, the lift at angles of attack greater than 6° decreased, probably due to the increase in the pressures caused by separation over the lee side of the afterbody. A comparison of the results from models B_3 and B_4 (fig. 4(a)) shows that the change in nose shape affected the lift characteristics only at angles of attack greater than 6°.

Pitching-moment and center-of-pressure location.- The results of all the body-alone tests without transition (see fig. 4(a)) indicate an appreciable reduction in C_{m_α} at about 5° angle of attack which is caused by the flow separation and low pressure recovery on the lee side of the afterbody. This reduction is, in effect, a stabilizing contribution in that the center of pressure progresses rearward very rapidly as the angle of attack is increased from 5° to 10° (for example, fig. 16). It was found that inducing transition from 2 to 6 inches behind the nose of the body would result in an appreciable reduction in the variation of C_{m_α} in this angle-of-attack range due to the increase in the pressures over the lee side of the afterbody. The primary effect in changing the nose shape (compare models B_3 and B_4 in fig. 16) was to move the center of pressure farther forward for the case of model B_4 which had a nose of higher apex angle.

Drag.- As expected, the drag of B_4 is somewhat higher than that of B_2 throughout the angle-of-attack range because of the higher apex angle of the nose. Drag "buckets" disappear with the change in flow character over the afterbody. As transition is induced farther forward on the bodies, $C_{D_{min}}$ increases because of the increase in surface area within the nonlaminar region of flow.

Comparison of experimental and theoretical results.- In figures 24(a) and 24(b) the experimental characteristics of B_2 and B_4 at the three test Mach numbers are compared with the results of the potential theory of references 4 and 6 and the potential-plus-viscous approximation of reference 5. The experimental lifts are in good agreement with the theory of reference 5 throughout the angle-of-attack range in which the flow separation from the lee side of the body was believed nonexistent or of secondary importance; the pitching moments and incremental drags within this α range are in fair agreement. As the separation effects

become more predominant (above $\alpha = 5^{\circ}$) the discrepancies between the experimental and predicted characteristics increase.

Body-Wing

The measured results of the body-wing tests are presented in figures 5, 9, and 13. The experimental lifts and pitching moments of three body-wing combinations are compared in figure 25 with results obtained using infinite and slender-body theory in conjunction with slender-wing theory (ref. 7) and a modified slender-body theory (ref. 8) using the lift-curve slopes for the isolated wings from reference 9.

Experimental results.- In general, for all BW combinations, C_{L_α} increases with α for a given roll angle. For angles of attack up to about 5°, no variation in lift resulted from variations in roll angle. This effect was predicted in reference 7; however, at higher angles of attack the lift of BW combinations is, in general, slightly higher when the roll angle is such that two opposite wing panels are in the angle-of-attack plane. It is also noted that shifting the longitudinal location of W_1^{45} forward about 0.8 body diameter on the cylindrical part of B_4 results in no change in the lift of the combination. (See fig. 5(b).)

The center-of-pressure locations presented in figure 17 show that, in general, as the angle of attack increases, the center-of-pressure locations move rearward. In comparison to the body-alone analysis, the rearward center-of-pressure movements of the BW combinations are much less; this decrease suggests that the contribution of the exposed wing panels is such as to reduce the rearward center-of-pressure movement and also that there is a reduction in the stabilizing effects of the flow over the afterbody caused by the effects on the flow of the body-wing juncture and the pressure field of the wing tip. The effect of roll is to reduce the rearward center-of-pressure movement as opposite wing panels move out of the angle-of-attack plane.

Comparison of experimental and theoretical results.- The results of tests of configurations $B_4W_7^{0}$, $B_4W_8^{0}$, and $B_4W_9^{0}$ were selected to compare with the theories of references 7 and 8 because these configurations represent a BW combination in which the wing span was varied systematically; these experimental and theoretical results are presented in figure 25 and in the following table (for 0° angle of attack):

	$(C_{L_{\alpha_W}})_B$	$C_{L_{\alpha_{BW}}}$	$(C_{m_{\alpha_W}})_B$	$C_{m_{\alpha_{BW}}}$	$\frac{C_{m_{\alpha_{BW}}}}{C_{L_{\alpha_{BW}}}}$
$B_4W_7{}^0$					
Infinite-body and slender-wing theory, ref. 7	0.046	0.046	0.049	0.049	1.07
Slender-body and slender-wing theory, ref. 7	.046	.081	.049	.209	2.58
Modified slender-body theory	.026	.061	.025	.185	3.03
Experimental results	.016	.059	.016	.231	3.91
$B_4W_8{}^0$					
Infinite-body and slender-wing theory, ref. 7	0.089	0.089	0.102	0.102	1.15
Slender-body and slender-wing theory, ref. 7	.089	.124	.087	.247	1.97
Modified slender-body theory	.053	.088	.057	.217	2.47
Experimental results	.039	.082	.047	.262	3.19
$B_4W_9{}^0$					
Infinite-body and slender-wing theory, ref. 7	0.145	0.145	0.016	0.176	1.21
Slender-body and slender-wing theory, ref. 7	.145	.180	.171	.331	1.84
Modified slender-body theory	.087	.122	.104	.264	2.16
Experimental results	.072	.115	.109	.324	2.82

where $(C_{L_{\alpha_W}})_B = C_{L_{\alpha_{BW}}} - C_{L_{\alpha_B}}$ and $(C_{m_{\alpha_W}})_B = C_{m_{\alpha_{BW}}} - C_{m_{\alpha_B}}$. From these tabulated results, it can be seen that the modified slender-body theory of reference 8 predicts $(C_{L_{\alpha_W}})_B$, $C_{L_{\alpha_{BW}}}$, and $(C_{m_{\alpha_W}})_B$ with greater accuracy than the other two theories considered. Although $C_{m_{\alpha_{BW}}}$ calculated by the method of reference 8, was only in fair agreement with the experimental results, the center-of-pressure location obtained by using this theory was in better agreement. At the higher angles of attack the discrepancies, as shown in figure 25, between experiment and the aforementioned theories are believed to be caused by the viscous cross forces on the afterbody and are reduced somewhat by using the lifts and pitching moments computed by the potential-plus-viscous theory of reference 5.

Body-Tail Combination

In figures 6, 10, 14, and 15 are presented the results of the BT combination tests. Comparisons of the experimental lifts and pitching moments of two BT configurations are made with the results of theories presented in references 8, 10, and 11.

Experimental results.- For all BT configurations C_{L_α} increases with α for a given roll angle, though to a lesser extent for B_4T_5 and B_4T_7, the two BT configurations with larger span — body-diameter ratios. (See fig. 6.) The effect of roll angle on the lift of these two configurations, as well as B_2T_6, is negligible; however, for B_2T_1 and B_4T_4 (see figs. 6(a) and 6(b)) the lift of the combination is reduced as the two opposite tail panels are rolled out of the angle-of-attack plane. Similarly, there are smaller effects of roll on C_m for B_4T_5 and B_4T_7 than for the other BT configurations resulting in small effects on the center-of-pressure location due to roll. In general, the center-of-pressure location for all BT configurations is stationary or moves slightly rearward as α increases from 0° into the low angle-of-attack range. In the medium and higher angle-of-attack range the center-of-pressure movement is definitely forward. This forward movement is in contrast to the rearward center-of-pressure travels exhibited by the B and BW configurations.

Comparison of experimental and theoretical results.- The results of tests of configurations B_2T_1 and B_4T_5 are compared with the theoretical results obtained using the methods of references 8, 10, and 11 in figure 26 and in the following table (for 0° angle of attack and $M = 1.93$):

	$\left(C_{L_{\alpha T}}\right)_B$	$C_{L_{\alpha BT}}$	$\left(C_{m_{\alpha T}}\right)_B$	$C_{m_{\alpha BT}}$	$\frac{C_{m_\alpha}}{C_{L_\alpha}}$
B_2T_1					
Morikawa, reference 11	0.081	0.116	-0.391	-0.258	-2.22
Stewart and Maghreblian, reference 10	.055	.090	-.264	-.131	-1.46
Modified slender-body theory	.069	.104	-.331	-.198	-1.90
Experimental	.064	.107	-.292	-.128	-1.20
B_4T_5					
Morikawa, reference 11	0.330	0.365	-1.277	-1.117	-3.06
Steward and Meghreblian, reference 10	.188	.223	-.728	-.568	-2.55
Modified slender-body theory	.232	.267	-.896	-.736	-2.75
Experimental	.228	.271	-.771	-.556	-2.06

where $\left(C_{L_{\alpha_T}}\right)_B = C_{L_{\alpha_{BT}}} - C_{L_{\alpha_B}}$ and $\left(C_{m_{\alpha_T}}\right)_B = C_{m_{\alpha_{BT}}} - C_{m_{\alpha_B}}$. Here again, as shown previously in the table of BW results, the modified slender-body theory (ref. 8) overestimates $\left(C_{L_{\alpha_T}}\right)_B$ and $\left(C_{m_{\alpha_T}}\right)_B$, and the addition of the lift and pitching moment of the body alone, which are underestimated by the potential theory, results in excellent agreement for $C_{L_{\alpha_{BT}}}$ and fair agreement for $C_{m_{\alpha_{BT}}}$. It is noted that the method of reference 10 predicts $\left(C_{m_{\alpha_T}}\right)_B$ closer than either of the other two methods with the result of better agreement of the center-of-pressure location of both BT configurations. This agreement is believed to be somewhat fortuitous since the lift carry-over from the wing onto the body as indicated by the low predictions of $\left(C_{L_{\alpha_T}}\right)_B$ is not considered in this method.

Body-Wing-Tail Combination

Presented in figures 7, 11, 14, and 15 are the results of the BWT tests. Comparisons of experimental and calculated lifts, pitching moments, center-of-pressure locations and tail efficiencies are presented in figures 27 and 28 for four configurations, each with 0° and 45° interdigitation angles.

Experimental results.- The first series of BWT configurations tested are considered to be typical air-to-air missiles having equal-span wings and tails. With such configurations, most of the tail operates within a region of high downwash and/or reduced dynamic pressure produced by the wing which, at some angles of attack, results in a loss of tail lift accompanied by a forward center-of-pressure movement. The gross effects of the vorticity behind the wing upon the tail have been assessed by use of the tail efficiency parameter η_t where

$$\eta_t = \frac{C_{L_{BWT}} - C_{L_{BW}}}{C_{L_{BT}} - C_{L_B}}$$

$$= \frac{\left(C_{L_T}\right)_{BW}}{\left(C_{L_T}\right)_B}$$

For the η_t value at $\alpha = 0^\circ$, the slopes of the above-mentioned quantities at $\alpha = 0^\circ$ were used. It is seen that this parameter is the

ratio of the lift of the tail in the presence of the body wing to the lift of the tail in the presence of the body (the tail efficiency may also be defined in terms of pitching moments). If the effects of the wing upon the tail are zero, then $\eta_t = 1.00$. Assessment of wing-tail interference has also been made by use of the center-of-pressure locations.

For the BWT configuration having inline, equal-span wings and tails, the effectiveness of the tail was less at low angles of attack and increased as the tail was displaced with respect to the vorticity behind the wing. For example, for configuration $B_2W_1{}^0T_1$, the effects of the wing upon the tail are so pronounced that near $\alpha = 0^\circ$ the pitching moment about the test pitching-moment reference is unstable (see fig. 7(a)); as α increases η_t increases (see fig. 19(a)) and the center of pressure moves rearward. The effect of roll angle is small.

For the configurations with $\theta = 45^\circ$, the vorticity is initially displaced with respect to the tail because of the geometry of the configuration; therefore, the tail translates through the high effective downwash region at some medium angle of attack. For $B_2W_1{}^{45}T_1$ at $\phi = 0^\circ$, the effects of the vorticity cause a loss in tail lift and a reduction in C_m at angles of attack above about 6° that are reflected in large variations in η_t and center-of-pressure location. (See fig. 19(c).) Systematic variations in roll angle from 0° to 45° result in higher tail efficiencies and less center-of-pressure travel throughout the high α range as the roll angles progress from 0°.

The preceding results suggested the possibility that an intermediate interdigitation angle might reduce the large variation of η_t through the action of asymmetrical displacement of the tail with respect to the vortex sheets. The results of the same basic configuration with 30° interdigitation angle $(B_2W_1{}^{30}T_1)$ presented in figure 19(b) indicate that at $\phi = 0^\circ$ the variation in η_t and center-of-pressure location are decreased (as compared with $B_2W_1{}^0T_1$ and $B_2W_1{}^{45}T_1$); however, the variations with roll angle are very erratic. Also, induced rolling moments are present at angles of attack for all roll angles of attack including 0° and 45°. (See ref. 2.)

The foregoing results, particularly for the interdigitated configurations, suggested the possibility of decreasing the variations in η_t and in the center-of-pressure location through the use of a tail having lifting surfaces displaced with respect to the vorticity behind the wing. Figures 11(b) and 21(b) present the results of tests at $M = 1.62$ of

the same B_2W_1 combination with a ring tail T_3; the geometry of T_3 was such that a major portion of the lifting surface of this tail was outboard of the vorticity behind the wing at low and moderate angles of attack. The use of T_3 reduces the center-of-pressure travel throughout the α range from 0.79 body diameter for $B_2W_1{}^{45}T_1$ to 0.40 body diameters for $B_2W_1{}^{45}T_3$ at $\phi = 0^\circ$ (figs. 21(a) and (b)). Although the drag throughout the test α range is increased about 25 percent, the use of the ring tail might present a partial solution to the wing-tail interference problem for this type of missile.

At this stage in the test program it was realized that, in order to simulate more nearly typical air-to-air missiles with the seeker antenna in the nose, the nose shape should be changed from the conical on B_2 to the shape on B_4; therefore, the configuration $B_4W_1{}^{45}T_1$ was devised and tested at two roll angles. The results presented in figure 19(d) indicate that the η_t and center-of-pressure characteristics are similar to those of $B_2W_1{}^{45}T_1$ with the exception that the minimum η_t is delayed to a higher α. This delay results from purely geometric considerations whereby, as a result of the short distance between wing and tail, a higher angle of attack is required in order to translate the tail into the regions of greatest vorticity. This effect was further investigated through the use of $B_4W_4{}^{45}T_1$. The wing W_4 was devised with a highly swept leading edge in order to reduce further the distance between wing and tail and still maintain a center-of-pressure location for $B_4W_4{}^{45}$ comparable to that of $B_4W_1{}^{45}$. As indicated in figure 19(e), the center of pressure and η_t characteristics are not improved. This lack of improvement is believed to be due primarily to the releases of vorticity well ahead of the trailing edge of the wing, effectively reducing the angle of attack at which the tail is translated into regions of high vorticity. The reduction of dynamic pressure due to the wing in the region occupied by the tail also contributed to the loss of tail lift and subsequently resulted in the lack of improvement of center of pressure and η_t characteristics.

Thus far, all BWT configurations discussed have had equal-span wings and tails; with the exception of the ring-tailed BWT configurations little improvement in the η_t and center-of-pressure characteristics had been noted. It appeared in order at this time to diverge from such configurations to configurations having larger-span tails which would extend parts of the tail outside of the regions of high vorticity.

An approach to this class of BWT configurations was made by testing two tails of different spans in combination with $B_4W_{1A}{}^{45}$. The configuration $B_4W_{1A}{}^{45}$ (see fig. 1) was the same as $B_4W_1{}^{45}$ with the exception that the wing W_1 was installed 0.650 inch closer to the nose. The results of tests of $B_4W_{1A}{}^{45}T_4$ and $B_4W_{1A}{}^{45}T_6$ (see fig. 19(e)) indicate that the increased tail spans are sufficient to result in much lower variations of η_t and center of pressure than are exhibited by $B_4W_1{}^{45}T_1$; in fact, the use of T_6 results in a maximum center-of-pressure travel of 0.29 body diameter throughout the test angle-of-attack range of 14° as compared with 0.85 body diameter for $B_4W_1{}^{45}T_1$.

In order to investigate further the effects of systematic changes in wing-tail-span ratios, three canard-type configurations were designed and tested utilizing the same BT combination (B_4T_5) and varying the span of the triangular forward lifting surfaces $(W_7,\ W_8,$ and $W_9)$. The results of these tests (see figs. 7(f) to 7(h) and figs. 19(f) to 19(k)) indicate that, for the canard-type missile also, the static stability characteristics become worse as the wing-tail-span ratio increases. For the inline configurations, $B_4W_7{}^0T_5$, $B_4W_8{}^0T_5$, and $B_4W_9{}^0T_5$ at $\alpha = 0°$, the tail efficiency decreases and the center of pressure moves forward as the wing span increases; for these configurations, there are minor effects due to roll angle. For the interdigitated configurations, $B_4W_7{}^{45}T_5$, $B_4W_8{}^{45}T_5$, and $B_4W_9{}^{45}T_5$, as the wing-tail-span ratio increases the lowest value of η_t decreases and the center-of-pressure movement throughout the α range increases because of the increased wing-tail interference. There are slight effects due to the variation in roll angle.

Further development of the canard-type configurations consisted in two variations in the wing plan form in combination with the same BT combination. The two configurations, $B_4W_{10}T_5$ and $B_4W_{13}T_5$, were tested in order to assess the combined effects of variation in spanwise loading (and, consequently, spanwise vorticity distribution), wing-body interference, and component characteristics upon the η_t and center-of-pressure characteristics while maintaining approximately the same wing-tail-span ratio; these data are presented in figures 19(l) to 19(o). The change from $W_{10}{}^0$ to $W_{13}{}^0$ results in a small decrease in η_t and a forward shift in center-of-pressure location of about 0.25 body diameter at $\phi = 0°$ and $\phi = 45°$ throughout the test angles of attack. For the interdigitated configurations, changing from $W_{10}{}^{45}$ to $W_{13}{}^{45}$

causes a slight decrease in η_t at both roll angles with a forward movement in the center-of-pressure location of about 0.20 body diameter at $\phi = 0^\circ$ and from 0.20 to 0.40 body diameter at $\phi = 45^\circ$ at the test angles of attack.

All the canard-type configurations discussed thus far have exhibited rearward center-of-pressure travels from 0.45 body diameter to about 1.0 body diameter caused by changes in angle of attack or angle of roll or combinations of each. Undoubtedly, a part of this center-of-pressure travel was contributed by the BW combinations (see figs. 17(b) and 17(c)); also, no forward center-of-pressure travel was exhibited by B_4T_5 as had been exhibited by all of the other BT combinations (see figs. 18(a) and 18(b)). The next configuration was therefore designed in an effort to reduce the rearward center-of-pressure travel of the BW combination and to increase the forward center-of-pressure travel of the BT combination. The tail T_7 was a modification of T_5 to approach more nearly the geometry of T_1 because the center-of-pressure travel of B_2T_1 was forward. The wing W_{11} was designed to compensate for the change in C_m due to the reduction in tail lift.

The results of the tests of $B_4W_{11}{}^0T_7$ (see fig. 19(p)) show that, although the η_t variation is greater (as compared with that for $B_4W_{10}{}^0T_5$ and $B_4W_{13}{}^0T_5$), the center-of-pressure travel is reduced to about 0.32 body diameter at $\phi = 0^\circ$ and $\phi = 45^\circ$ throughout the test angle-of-attack range; however, the center-of-pressure travel for changes of combined angle of attack and roll is about 0.55 body diameter which exceeds that exhibited by $B_4W_{13}{}^0T_5$. Improvement is noted, however, for the configuration $B_4W_{11}{}^{45}T_7$ (see fig. 19(q)), with combined angles of attack and roll resulting in a center-of-pressure travel of only 0.35 body diameter. Thus, this configuration is deemed superior, with regard to static stability characteristics, to all the other canard-type configurations tested. In view of this fact, additional tests were made of this configuration at $M = 2.40$ (figs. 15 and 23(b)). Tests scheduled at $M = 1.62$ were only partially completed because of difficulties with the balance system. Comparison of the results at $M = 1.93$ and $M = 2.40$ indicates that the center-of-pressure travel is reduced and η_t is increased as the Mach number is increased (fig. 29(b)); similar results are also indicated in the case of $B_2W_1{}^{45}T_1$ where the maximum center-of-pressure travels are 0.75, 0.60, and 0.55 body diameter at Mach numbers of 1.62, 1.93, and 2.40, respectively.

One other configuration of interest that was reported in reference 3 was $B_4W_{11}{}^0W_8{}^{45}T_7$; this unusual configuration consisted of $B_4W_{11}{}^0T_7$ with the wing W_8 installed at 45° interdigitation angle at about the center-of-gravity location. This configuration was tested in an attempt to reduce the rearward center-of-pressure travel of $B_4W_{11}{}^0T_7$ as α increased by inserting $W_8{}^{45}$ which provides an additional vortex system at medium and high angles of attack. This vortex system increases the effective downwash within which the inboard parts of T_7 operate, thereby reducing effectiveness of the tail. (Compare figs. 19(p) and 19(r).) These effects upon the center-of-pressure travel are detrimental at low angles of attack; however, at medium and high angles of attack, the rate of change of center-of-pressure travel with α is reduced and the maximum center-of-pressure travel between $\alpha = 3°$ and $\alpha = 14°$ is 0.15 body diameter for $B_4W_{11}{}^0W_8{}^{45}T_7$ as compared with 0.25 for $B_4W_{11}{}^0T_7$.

Comparison of experimental and theoretical results.- Presented in figures 27 and 28 are comparisons of the experimental and theoretical C_L, C_m, η_t, and center-of-pressure locations for four missile configurations at 0° and 45° interdigitation angles. The theoretical characteristics were calculated by use of the methods discussed in the appendix. As indicated in figure 27, the calculated lifts and pitching moments are in good agreement with the experiment except in the case of $B_2W_1{}^{45}T_1$ at the medium angles of attack; this discrepancy is due to the difference between the experimental and calculated η_t values within this α range. (See fig. 28(b).)

The difficulties involved in making a more accurate prediction of η_t for such a configuration (having equal-span cruciform wings and tails with wings interdigitated 45°) consisted of, first, making a more accurate prediction of the vortex locations with respect to the lifting tail panels (fig. 30) and, second, making a more realistic approximation of the division of load between the upper and lower pairs of wing panel. By use of the schlieren photographs available, it was determined that at medium and high angles of attack the calculated vortex positions were outboard of the experimental positions. Although, for the calculations, this results in a larger part of the tail being in a region of downwash, the inboard stations which contributed the greatest magnitude of section lift are operating within a region of lower downwash, thereby reducing the loss of lift experienced by these inboard parts. Furthermore, this reduction in loss of lift apparently more than compensates for the greater loss of lift experienced by the outboard parts of the tail and results in an increase in η_t. (See fig. 28(b).)

With regard to the division of loads between upper and lower wing panels, it was assumed in the calculations that the lower panels carried two-thirds of the total lift supported by the four panels at all angles of attack; it is recognized that a variation in division of load with angle of attack would be more realistic.

The two aforementioned difficulties were not apparent in the calculations of the canard-type configurations because of the large geometry of the tail relative to that of the wing, nor should they be apparent in the case of missiles having wing-tail-span ratios significantly greater than 1.

Despite the difficulties involved, the discrepancies between the calculated and experimental center-of-pressure locations are never greater than 0.55 body diameter and, for the majority of the cases considered, are no greater than 0.35 body diameter.

Visual flow observations.- In figure 31 are presented schlieren photographs taken in a plane perpendicular to the angle-of-attack plane of $B_2W_1{}^0T_1$ and $B_2W_1{}^{45}T_1$ at $\phi = 0^\circ$ and at various angles of attack. For the inline configurations the vortices behind the wing panels appear to move farther inboard in the plane normal to the tail as α increases. This movement was due to the presence of the body and the induced effects of one vortex upon the other. At angles of attack less than $\alpha = 10^\circ$, the vortices were shed at the wing tip and, at $\alpha = 10^\circ$ and 13°, the initial location of the vortices moved inboard.

The same results with regard to the initial vortex locations are noted for $B_2W_1{}^{45}T_1$ with the paths of the four vortices being easily distinguished. The effects of the body are obvious and cause the lower pair of vortices to move outboard and the upper pair inboard. Of interest is the fact that at $\alpha = 10^\circ$ the tail is in the path of the two lower vortices as noted by the disappearance of the vortices behind the tail panels; a portion of the tail was thus subjected to higher downwash which resulted in a maximum loss of tail lift as is indicated by the force data. At $\alpha = 13^\circ$ the tail is out of the region occupied by the vortices.

CONCLUSIONS

The results of an investigation at supersonic speeds, primarily at $M = 1.93$ and a Reynolds number of 0.32×10^6 per inch, of a number of cruciform missile configurations and their components indicate the following conclusions:

(1) By use of the method presented in this paper the predicted effects of wing-tail interference upon the lift and static stability of the various missile configurations investigated were generally in good agreement with the experimental results. The method satisfactorily predicts the effects of changes of interdigitation angle and systematic changes in wing-tail-span ratio at angles of attack up to 14°.

(2) The effects of wing-tail interference become increasingly detrimental to the static stability of a missile as the wing and tail spans become equal.

(3) For the missile configurations that were tested at various Mach numbers, the tail efficiencies increased with an increase in Mach number.

(4) The use of the ring tail presents a possible solution to the wing-tail interference problem for missiles having equal-span wings and tails if higher drags can be tolerated.

(5) The configuration having the least center-of-pressure travel throughout the test angle-of-attack range from 0° to 15° and at all roll angles was $B_4W_{11}{}^{45}T_7$; the maximum center-of-pressure travel due to the combined effects of angles of attack and roll was approximately 0.35 body diameter.

(6) In general, the variation of lift and pitching-moment coefficients with angle of attack of the body-wing and body-tail combinations increase with angle of attack, and the variation of lift coefficient with angle of attack predicted by the modified-slender-body theory are in excellent agreement with the experimental values.

(7) Effects of viscosity upon the lift and pitching-moment characteristics of the body-alone configurations tested in this investigation are appreciable and only fair prediction is possible by available methods.

Langley Aeronautical Laboratory
National Advisory Committee for Aeronautics
Langley Field, Va.

APPENDIX

DISCUSSION OF THEORETICAL METHOD USED TO CALCULATE THE TAIL EFFICIENCIES AND CENTER-OF-PRESSURE TRAVELS OF BWT CONFIGURATIONS AT ZERO ROLL ANGLE

Calculation of Tail Efficiencies

For calculative purposes, it has been found convenient to reduce the basic tail efficiency equation

$$\eta_t = \frac{C_{L_{BWT}} - C_{L_{BW}}}{C_{L_{BT}} - C_{L_B}} \tag{1}$$

to the form

$$\eta_t = 1 - \frac{\left(\Delta C_{L_T}\right)_W}{\left(C_{L_T}\right)_B} \tag{2}$$

where

$\left(\Delta C_{L_T}\right)_W$ loss of tail lift due to the addition of the wing

$\left(C_{L_T}\right)_B$ lift of the tail in the presence of the body

In order to calculate $\left(\Delta C_{L_T}\right)_W$, it was assumed that the vorticity shed from each wing panel was concentrated into one discrete vortex, fully rolled up at the trailing edge of the wing, with the spanwise location at the centroid of the vorticity. The strength of each vortex Γ was determined from the spanwise loading of its respective panel; for the planar-wing condition (see ref. 12)

$$\Gamma = \frac{l_R}{\rho U} \tag{3}$$

where

l_R section lift at root of wing panel

For the interdigitated cruciform configurations, approximations were made regarding the relative strengths of the upper and lower pairs of vortices which will be discussed later in this section. The effect of the body on calculating Γ was assumed to be zero.

The positions of the vortices with respect to the tail (see fig. 30) was determined for the inline configurations by calculating the path of two vortices, in the presence of a circular cylinder, from their initial position at the trailing edge of the wing to a plane passing through the tail normal to the wind. (See ref. 12). For the interdigitated canard-type configurations, it was believed that, because of the large geometry of the tail, secondary variations in the vortex locations with respect to the tail would have little effect upon η_t; therefore, it was assumed that the vortices were emitted from the centroid of the vorticity and traveled in a free-stream direction from the wing to the tail. The use of this assumption for $B_2W_1{}^{45}T_1$ was not possible since equal-span wings and tails were used and a variation in the location of the vortices with respect to the tail would result in a primary change in the lift of the tail. For this configuration, at $\alpha = 10^\circ$ the path of each vortex was traced in one step from the wing to the plane passing through the tail by solving for the velocities induced by the vortices from the other three wing panels, by the four image vortices within the body, and by the flow due to the body. The vortex under inspection was displaced as required by the resultant of the induced flows. The vortices were then assumed to have a linear variation due to changes in α from $\alpha = 0^\circ$ to $\alpha = 14^\circ$, passing through the locations determined for $\alpha = 10^\circ$.

The apparent fallacies of this procedure are recognized, namely, that solutions for the vortex travel should be obtained at several angles of attack and at each angle of attack the travel of the vortex downstream from the wing should be accomplished in several steps rather than one. This more rigorous solution is time consuming and has been neglected.

The strengths and locations of the trailing vortices were then used to calculate the induced velocities in the plane of the tail. It was then possible to determine the loss of tail lift due to the addition of the wing by the method given in reference 13 and the following relation:

$$\left(\Delta C_{L_T}\right)_W = \int_{d/2}^{b_t/2} v(Z)F(Z)dZ \qquad (4)$$

where

$v(Z)$ vertical component of induced velocities due to the wing

$F(Z)$ spanwise loading of reversed tail

The lift of the tail in the presence of the body is given by the relation

$$\left(C_{L_T}\right)_B = \int_{d/2}^{b_t/2} \epsilon(Z)F(Z)dZ \qquad (5)$$

where

$\epsilon(Z)$ vertical component of induced velocity about the body $= \alpha\left(1 + \frac{r^2}{Z^2}\right)$

Z distance from body center line to spanwise location under inspection

By substituting the values of $\left(\Delta C_{L_T}\right)_W$ and $\left(C_{L_T}\right)_B$ found in equations (4) and (5) into equation (2), the solution of η_t was completed. Comparisons with the experimental results were made in figure 28.

In order to determine the effect of changing the division of load between the upper and lower pair of wing panels for the interdigitated configuration $B_2W_1{}^{45}T_1$, calculations of η_t were made using different ratios of loading between the upper and lower wing panels. As the loading was progressively increased on the lower, or leading, wing panels, the tail efficiency decreased; this decrease was to be expected since the vortices shed from the lower panels were more closely associated with the loading on the tail surfaces at angles of attack. It was evident from this comparison that an approximation of the division of load had to be made in order to predict more closely the tail efficiency of interdigitated configurations. For the present calculations, a ratio of 2 to 1 between the circulation of the lower and upper pairs of panels, respectively, has been used. For information and guidance in this particular problem, further experimental investigation appears in order.

Calculation of the Center-of-Pressure Location

In order to calculate the center-of-pressure locations of BWT configurations (including the effects of wing-tail interference), equation (1) was converted to the form

$$C_{L_{BWT}} = C_{L_{BW}} + \eta_t\left(C_{L_{BT}} - C_{L_B}\right)$$

$$= C_{L_{BW}} + \eta_t\left(C_{L_T}\right)_B \tag{6}$$

A similar equation was written in terms of pitching moments as

$$C_{m_{BWT}} = C_{m_{BW}} + \eta_t\left(C_{m_{BT}} - C_{m_B}\right)$$

$$= C_{m_{BW}} + \eta_t\left(C_{m_T}\right)_B \tag{7}$$

Equation (7) is valid only if the tail efficiencies defined using lifts and pitching moments are of equal magnitude; examination of the experimental data has indicated that there is rarely a difference greater than 10 percent in the ratio of η_t obtained by using pitching moments to η_t obtained by using lifts. When converted into center-of-pressure location, this 10-percent difference is of the order of 1/8 body diameter.

The lifts and pitching moments of the BW and BT combinations were computed by use of the modified slender-body theory of reference 8 and the charts of reference 9. The quantities $\left(C_{L_T}\right)_B$ and $\left(C_{m_T}\right)_B$ were then determined by the relations

$$\left(C_{L_T}\right)_B = C_{L_{BT}} - C_{L_B}$$

and

$$\left(C_{m_T}\right)_B = C_{m_{BT}} - C_{m_B}$$

where C_{L_B} and C_{m_B} were computed using the potential-plus-viscous approximation of reference 5. The lift and pitching moments of the BWT configurations were then calculated through the use of equations (6) and (7); comparisons with the experimental results were made in figure 27. From these quantities the center-of-pressure locations were determined and compared with the experimental results in figure 28.

REFERENCES

1. Rainey, Robert W.: Langley 9-Inch Supersonic Tunnel Tests of Several Modifications of a Supersonic Missile Having Tandem Cruciform Lifting Surfaces. Three-Component Data Results of Models Having Ratios of Wing Span to Tail Span Equal to 1. NACA RM L9L30, 1951.

2. Rainey, Robert W.: Langley 9-Inch Supersonic Tunnel Tests of Several Modifications of a Supersonic Missile Having Tandem Cruciform Lifting Surfaces. Three-Component Data Results of Models Having Ratios of Wing Span to Tail Span Equal to and Less Than 1 and Some Static Rolling Moment Data. NACA RM L50G07, 1951.

3. Rainey, Robert W.: Langley 9-Inch Supersonic Tunnel Tests of Several Modifications of a Supersonic Missile Having Tandem Cruciform Lifting Surfaces. Three-Component Data Results of Models Having Ratios of Wing Span to Tail Span Less Than 1. NACA RM L50I29a, 1951.

4. Munk, Max M.: The Aerodynamic Forces on Airship Hulls. NACA Rep. 184, 1924.

5. Allen, H. Julian: Estimation of the Forces and Moments Acting on Inclined Bodies of Revolution of High Fineness Ratio. NACA RM A9I26, 1949.

6. Van Dyke, Milton D.: First-Order and Second-Order Theory of Supersonic Flow Past Bodies of Revolution. P-125, The RAND Corp. (Santa Monica, Calif.), Dec. 1949.

7. Spreiter, John R.: The Aerodynamic Forces on Slender Plane- and Cruciform-Wing and Body Combinations. NACA Rep. 962, 1950. (Supersedes NACA TN's 1897 and 1662.)

8. Nielsen, Jack N., and Kaattari, George E.: Method for Estimating Lift Interference of Wing-Body Combinations at Supersonic Speeds. NACA RM A51J04, 1951.

9. Lapin, Ellis: Charts for the Computation of Lift and Drag of Finite Wings at Supersonic Speeds. Rep. No. SM-13480, Douglas Aircraft Co., Inc., Oct. 14, 1949.

10. Stewart, Homer J., and Meghreblian, Robert V.: Body-Wing Interference in Supersonic Flow. Progress Rep. No. 4-99, Jet Propulsion Lab., C.I.T., 1949.

11. Morikawa, George: Supersonic Wing-Body Lift. Jour. Aero. Sci. vol. 18, no. 4, Apr. 1951, pp. 217-228.

12. Lagerstrom, P. A., and Graham, M. E.: Aerodynamic Interference in Supersonic Missiles. Rep. No. SM-13743, Douglas Aircraft Co., Inc., July 1950.

13. Alden, Henry L., and Schindel, Leon H.: The Calculation of Wing Lift and Moments in Nonuniform Supersonic Flows. Guided Missiles Program, M.I.T. Meteor Rep. No. 53, May 1950.

TABLE I.- SUMMARY OF EXPERIMENTAL VALUES OF $(C_{L_\alpha})_0$, $(C_{m_\alpha})_0$, AND $C_{D_{min}}$

Configuration	Roll angle ϕ, deg	M = 1.62				M = 1.93				M = 2.40			
		$(C_{L_\alpha})_0$	$(C_{m_\alpha})_0$	$C_{D_{min}}$	Figure	$(C_{L_\alpha})_0$	$(C_{m_\alpha})_0$	$C_{D_{min}}$	Figure	$(C_{L_\alpha})_0$	$(C_{m_\alpha})_0$	$C_{D_{min}}$	Figure
B_1	--	-----	-----	-----	-----	0.043	0.151	0.104	4(a)	-----	-----	-----	-----
B_2	--	0.042	0.160	0.113	8	.043	.164	.104	4(a), 4(b)	0.047	0.158	0.110	12
B_2 (1)	--	.043	.146	.177	8	.043	.164	.154	4(b)	.049	.166	.140	12
B_3	--	-----	-----	-----	-----	.043	.191	.104	4(a)	-----	-----	-----	--
B_4	--	.044	.187	.130	8	.043	.215	.107	4(a), 4(c)	.044	.204	.130	12
B_4 (2)	--	.044	.176	.210	8	.043	.204	.156	4(c)	.044	.204	.210	12
B_4 (3)	--	-----	-----	-----	-----	.043	.205	.171	4(c)	-----	-----	-----	--
B_4 (4)	--	-----	-----	-----	-----	.043	.210	.190	4(c)	-----	-----	-----	--
$B_2W_1{}^{45}$	0	.132	.117	.195	9	.127	.127	.174	5(a)	.125	.102	.183	13
$B_2W_1{}^{45}$	15	.130	.117	.195	9	.126	.128	.174	5(a)	-----	-----	-----	--
$B_2W_1{}^{45}$	30	.130	.128	.195	9	.124	.128	.174	5(a)	-----	-----	-----	--
$B_2W_1{}^{45}$	45	.129	.117	.195	9	.125	.128	.174	5(a)	-----	-----	-----	--
$B_4W_1{}^{45}$	0	-----	-----	-----	-----	.123	.095	.171	5(b)	-----	-----	-----	--
$B_4W_{1A}{}^{45}$	0	-----	-----	-----	-----	.122	.173	.175	5(b)	-----	-----	-----	--
$B_4W_4{}^{45}$	0	-----	-----	-----	-----	.156	.095	.188	5(b)	-----	-----	-----	--
$B_4W_7{}^{0}$	0	-----	-----	-----	-----	.059	.231	.200	5(c)	-----	-----	-----	--
$B_4W_7{}^{0}$	45	-----	-----	-----	-----	.058	.236	.200	5(c)	-----	-----	-----	--
$B_4W_8{}^{0}$	0	-----	-----	-----	-----	.082	.262	.208	5(c)	-----	-----	-----	--
$B_4W_8{}^{0}$	45	-----	-----	-----	-----	.082	.264	.208	5(c)	-----	-----	-----	--
$B_4W_9{}^{0}$	0	-----	-----	-----	-----	.115	.324	.215	5(c)	-----	-----	-----	--
$B_4W_9{}^{0}$	45	-----	-----	-----	-----	.115	.328	.215	5(c)	-----	-----	-----	--
$B_4W_{10}{}^{0}$	0	-----	-----	-----	-----	.091	-.406	.222	5(d)	-----	-----	-----	--
$B_4W_{10}{}^{0}$	45	-----	-----	-----	-----	.094	.398	.222	5(d)	-----	-----	-----	--
$B_4W_{11}{}^{0}$	0	-----	-----	-----	-----	.100	.411	.241	5(e)	.098	.383	.252	13
$B_4W_{11}{}^{0}$	45	-----	-----	-----	-----	.099	.420	.241	5(e)	.096	.404	.252	13
$B_4W_{13}{}^{0}$	0	-----	-----	-----	-----	.099	.441	.255	5(d)	-----	-----	-----	--
$B_4W_{13}{}^{0}$	45	-----	-----	-----	-----	.097	.435	.255	5(d)	-----	-----	-----	--
$B_4W_{11}{}^{0}W_8{}^{45}$	0	-----	-----	-----	-----	.136	.385	.282	5(e)	-----	-----	-----	--
$B_4W_{11}{}^{0}W_8{}^{45}$	45	-----	-----	-----	-----	.137	.398	.282	5(e)	-----	-----	-----	--
B_2T_1	0	.112	-.181	.155	10(a)	.107	-.128	.141	6(a)	.105	-.097	.165	14
B_2T_1	15	.113	-.181	.155	10(a)	.107	-.128	.141	6(a)	-----	-----	-----	--
B_2T_1	30	.113	-.181	.155	10(a)	.108	-.130	.141	6(a)	-----	-----	-----	--
B_2T_1	45	.113	-.181	.155	10(a)	.108	-.129	.141	6(a)	-----	-----	-----	--
B_2T_3	0	.165	-.475	.220	10(b)	-----	-----	-----	----------	-----	-----	-----	--
B_2T_3	45	.162	-.470	.220	10(b)	-----	-----	-----	----------	-----	-----	-----	--
B_2T_6	0	-----	-----	-----	-----	.120	-.238	.201	6(b)	-----	-----	-----	--
B_2T_6	45	-----	-----	-----	-----	.117	-.209	.201	6(b)	-----	-----	-----	--
B_4T_4	0	-----	-----	-----	-----	.115	-.149	.279	6(b)	-----	-----	-----	--
B_4T_4	45	-----	-----	-----	-----	.116	-.153	.279	6(b)	-----	-----	-----	--
B_4T_5	0	-----	-----	-----	-----	.271	-.536	.190	6(c)	-----	-----	-----	--
B_4T_5	45	-----	-----	-----	-----	.261	-.535	.190	6(c)	-----	-----	-----	--
B_4T_7	0	-----	-----	-----	-----	.217	-.495	.182	6(c)	.200	-.410	.195	15
B_4T_7	45	-----	-----	-----	-----	.213	-.467	.182	6(c)	.196	-.343	.195	15
$B_2W_1{}^{0}T_1$	0	-----	-----	-----	-----	.143	.064	.210	7(a)	-----	-----	-----	--
$B_2W_1{}^{0}T_1$	15	-----	-----	-----	-----	.143	.062	.210	7(a)	-----	-----	-----	--

(1) Transition 5" aft of nose.
(2) Transition 2" aft of nose.
(3) Transition 4" aft of nose.
(4) Transition 6" aft of nose.

TABLE I.- SUMMARY OF EXPERIMENTAL VALUES OF $(C_{L_\alpha})_0$, $(C_{m_\alpha})_0$, AND $C_{D_{min}}$ - Concluded

Configuration	Roll angle ϕ, deg	M = 1.62				M = 1.93				M = 2.40			
		$(C_{L_\alpha})_0$	$(C_{m_\alpha})_0$	$C_{D_{min}}$	Figure	$(C_{L_\alpha})_0$	$(C_{m_\alpha})_0$	$C_{D_{min}}$	Figure	$(C_{L_\alpha})_0$	$(C_{m_\alpha})_0$	$C_{D_{min}}$	Figure
$B_2W_1{}^0T_1$	30	-----	------	-----	-----	0.143	0.061	0.210	7(a)	-----	------	-----	--
$B_2W_1{}^0T_1$	45	-----	------	-----	-----	.148	.061	.210	7(a)	-----	------	-----	--
$B_2W_1{}^{30}T_1$	0	-----	------	-----	-----	.170	-.098	.215	7(b)	-----	------	-----	--
$B_2W_1{}^{30}T_1$	15	-----	------	-----	-----	.170	-.094	.215	7(b)	-----	------	-----	--
$B_2W_1{}^{30}T_1$	30	-----	------	-----	-----	.170	-.099	.215	7(b)	-----	------	-----	--
$B_2W_1{}^{30}T_1$	45	-----	------	-----	-----	.170	-.101	.215	7(b)	-----	------	-----	--
$B_2W_1{}^{30}T_1$	60	-----	------	-----	-----	.170	-.101	.215	7(b)	-----	------	-----	--
$B_2W_1{}^{30}T_1$	75	-----	------	-----	-----	.170	-.099	.215	7(b)	-----	------	-----	--
$B_2W_1{}^{45}T_1$	0	0.185	-0.142	0.240	11(a)	.175	-.120	.211	7(c)	0.177	-0.133	0.218	14
$B_2W_1{}^{45}T_1$	15	.185	-.145	.240	11(a)	.177	-.122	.211	7(c)	-----	------	-----	--
$B_2W_1{}^{45}T_1$	30	.189	-.141	.240	11(a)	.181	-.120	.211	7(c)	-----	------	-----	--
$B_2W_1{}^{45}T_1$	45	.187	-.141	.247	11(a)	.176	-.120	.211	7(c)	-----	------	-----	--
$B_2W_1{}^0T_3$	0	.210	-.258	.300	11(b)	-----	-----	-----	----	-----	------	-----	--
$B_2W_1{}^0T_3$	45	.215	-.258	.300	11(b)	-----	-----	-----	----	-----	------	-----	--
$B_2W_1{}^{45}T_3$	0	.216	-.331	.300	11(b)	-----	-----	-----	----	-----	------	-----	--
$B_2W_1{}^{45}T_3$	45	.212	-.305	.300	11(b)	-----	-----	-----	----	-----	------	-----	--
$B_4W_1{}^{45}T_1$	0	-----	------	-----	-----	.172	-.161	.215	7(d)	-----	------	-----	--
$B_4W_1{}^{45}T_1$	15	-----	------	-----	-----	.179	-.147	.215	7(d)	-----	------	-----	--
$B_4W_1{}^{45}T_1$	$22\frac{1}{2}$	-----	------	-----	-----	.179	-.145	.215	7(d)	-----	------	-----	--
$B_4W_1{}^{45}T_1$	30	-----	------	-----	-----	.179	-.144	.215	7(d)	-----	------	-----	--
$B_4W_1{}^{45}T_1$	45	-----	------	-----	-----	.176	-.154	.215	7(d)	-----	------	-----	--
$B_4W_{1A}{}^{45}T_4$	0	-----	------	-----	-----	.182	-.129	.347	7(e)	-----	------	-----	--
$B_4W_{1A}{}^{45}T_6$	0	-----	------	-----	-----	.194	-.178	.291	7(e)	-----	------	-----	--
$B_4W_4{}^{45}T_1$	0	-----	------	-----	-----	.201	-.099	.219	7(e)	-----	------	-----	--
$B_4W_7{}^0T_5$	0	-----	------	-----	-----	.261	-.464	.300	7(f)	-----	------	-----	--
$B_4W_7{}^0T_5$	45	-----	------	-----	-----	.254	-.456	.300	7(f)	-----	------	-----	--
$B_4W_7{}^{45}T_5$	0	-----	------	-----	-----	.274	-.496	.300	7(f)	-----	------	-----	--
$B_4W_7{}^{45}T_5$	45	-----	------	-----	-----	.264	-.459	.300	7(f)	-----	------	-----	--
$B_4W_8{}^0T_5$	0	-----	------	-----	-----	.255	-.374	.310	7(g)	-----	------	-----	--
$B_4W_8{}^0T_5$	45	-----	------	-----	-----	.254	-.351	.310	7(g)	-----	------	-----	--
$B_4W_8{}^{45}T_5$	0	-----	------	-----	-----	.288	-.423	.310	7(g)	-----	------	-----	--
$B_4W_8{}^{45}T_5$	45	-----	------	-----	-----	.281	-.396	.310	7(g)	-----	------	-----	--
$B_4W_9{}^0T_5$	0	-----	------	-----	-----	.255	-.191	.315	7(h)	-----	------	-----	--
$B_4W_9{}^0T_5$	45	-----	------	-----	-----	.255	-.188	.315	7(h)	-----	------	-----	--
$B_4W_9{}^{45}T_5$	0	-----	------	-----	-----	.310	-.321	.315	7(h)	-----	------	-----	--
$B_4W_9{}^{45}T_5$	45	-----	------	-----	-----	.307	-.304	.315	7(h)	-----	------	-----	--
$B_4W_{10}{}^0T_5$	0	-----	------	-----	-----	.268	-.243	.315	7(i)	-----	------	-----	--
$B_4W_{10}{}^0T_5$	45	-----	------	-----	-----	.260	-.218	.315	7(i)	-----	------	-----	--
$B_4W_{10}{}^{45}T_5$	0	-----	------	-----	-----	.291	-.275	.315	7(i)	-----	------	-----	--
$B_4W_{10}{}^{45}T_5$	45	-----	------	-----	-----	.288	-.270	.315	7(i)	-----	------	-----	--
$B_4W_{13}{}^0T_5$	0	-----	------	-----	-----	.265	-.156	.345	7(j)	-----	------	-----	--
$B_4W_{13}{}^0T_5$	45	-----	------	-----	-----	.253	-.146	.345	7(j)	-----	------	-----	--
$B_4W_{13}{}^{45}T_5$	0	-----	------	-----	-----	.294	-.220	.345	7(j)	-----	------	-----	--
$B_4W_{13}{}^{45}T_5$	45	-----	------	-----	-----	.293	-.215	.345	7(j)	-----	------	-----	--
$B_4W_{11}{}^0T_7$	0	-----	------	-----	-----	.212	-.107	.305	7(k)	-----	------	-----	--
$B_4W_{11}{}^0T_7$	45	-----	------	-----	-----	.212	-.087	.305	7(k)	-----	------	-----	--
$B_4W_{11}{}^{45}T_7$	0	.269	-.220	.330	11(c)	.248	-.182	.305	7(k)	.230	-.166	.312	15
$B_4W_{11}{}^{45}T_7$	45	.265	-.202	.330	11(c)	.248	-.181	.305	7(k)	.236	-.154	.312	15
$B_4W_{11}{}^0W_8{}^{45}T_7$	0	-----	------	-----	-----	.244	.010	.350	7(l)	-----	------	-----	--
$B_4W_{11}{}^0W_8{}^{45}T_7$	45	-----	------	-----	-----	.243	.010	.350	7(l)	-----	------	-----	--

Body	B_1	B_2	B_3	B_4
Fineness ratio	10.00	10.94	11.41	11.41

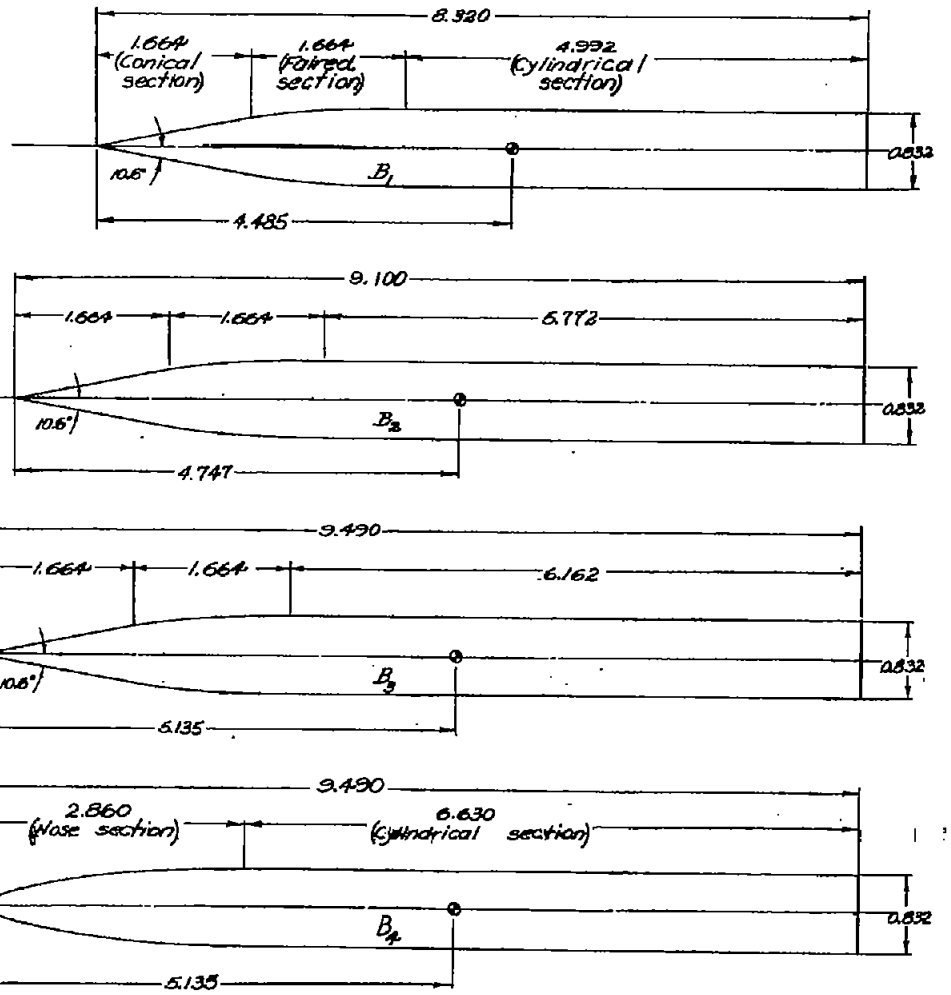

Ordinates of faired sections of B_1, B_2 and B_3

Distance from nose	Body Radius
1.664	.312
1.864	.348
2.064	.376
2.264	.395
2.464	.405
2.664	.411
2.864	.414
3.064	.415
3.328	.416

Ordinates of Nose Section, B_4

Distance from nose	Body radius
.005	.0066
.022	.018
.042	.030
.137	.073
.215	.101
.335	.138
.429	.164
.588	.203
.941	.272
1.287	.323
1.593	.358
2.203	.401
2.524	.412
2.717	.415
2.860	.416

NACA

Figure 1.- Model dimensions, designations, and moment-reference locations.

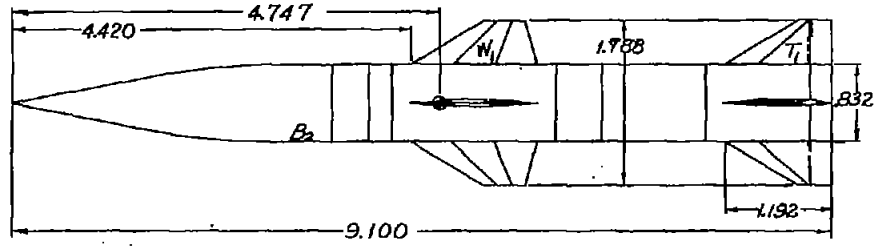

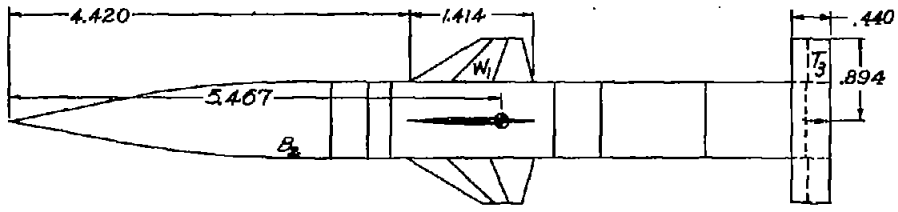

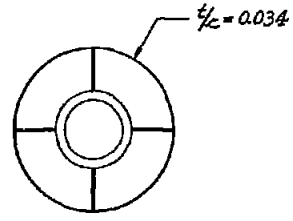

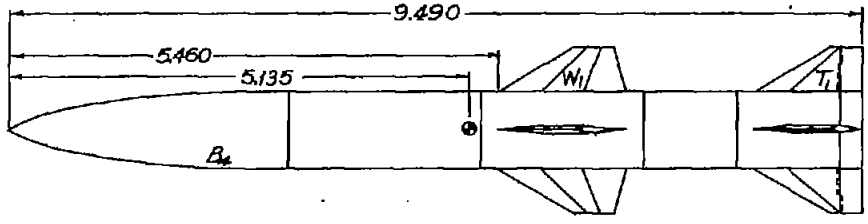

Surface	$(t/c)_R$	$(t/c)_T$	L.E. sweep angle	T.E. sweep angle	Aspect ratio
W_1	0.050	0.060	60°	-15°	1.32
T_1	.049	.049	60°	0°	1.57
T_4	.061	.045	45°	0°	2.40
T_6	.064	.064	0°	0°	5.00

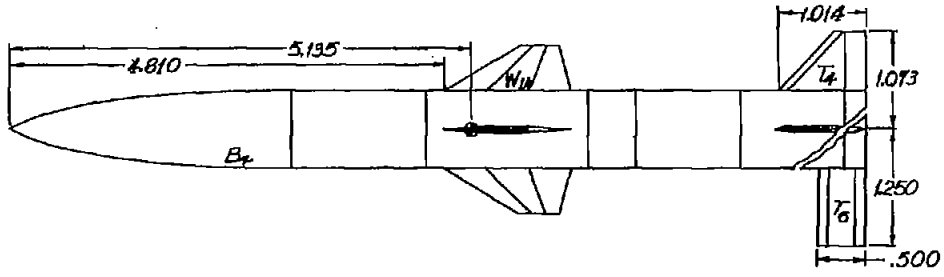

Figure 1.- Continued.

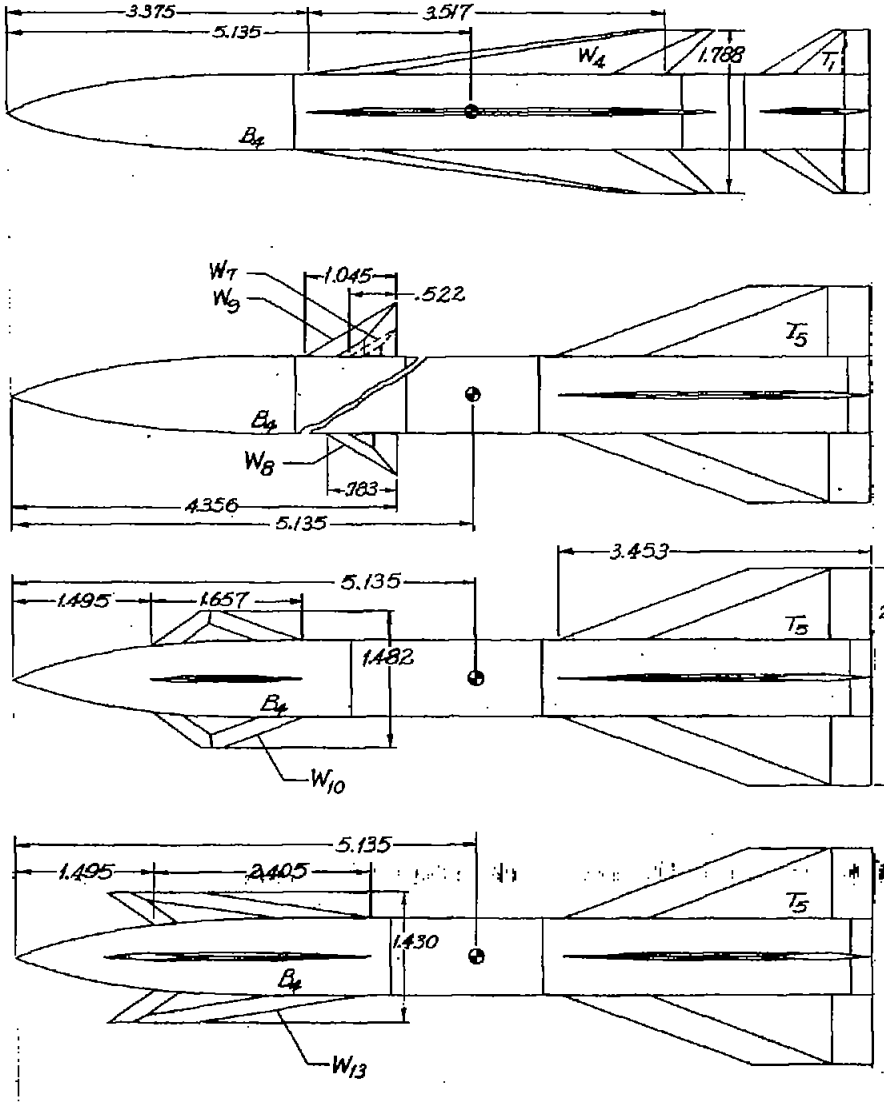

Surface	$(t/c)_R$	$(t/c)_T$	L.E. sweep angle	T.E. sweep angle	Aspect ratio
W_4	.016	.021	82.5°	47°	.53
W_7	.119	---	60°	0°	2.31
W_8	.079	---	60°	0°	2.31
W_9	.059	---	60°	0°	2.31
W_{10}	.037	.046	54°	-70°	.85
W_{13}	.021	.020	-55°	-81.2°	.68
T_5	.018	.045	70°	0°	.78

Figure 1.- Continued.

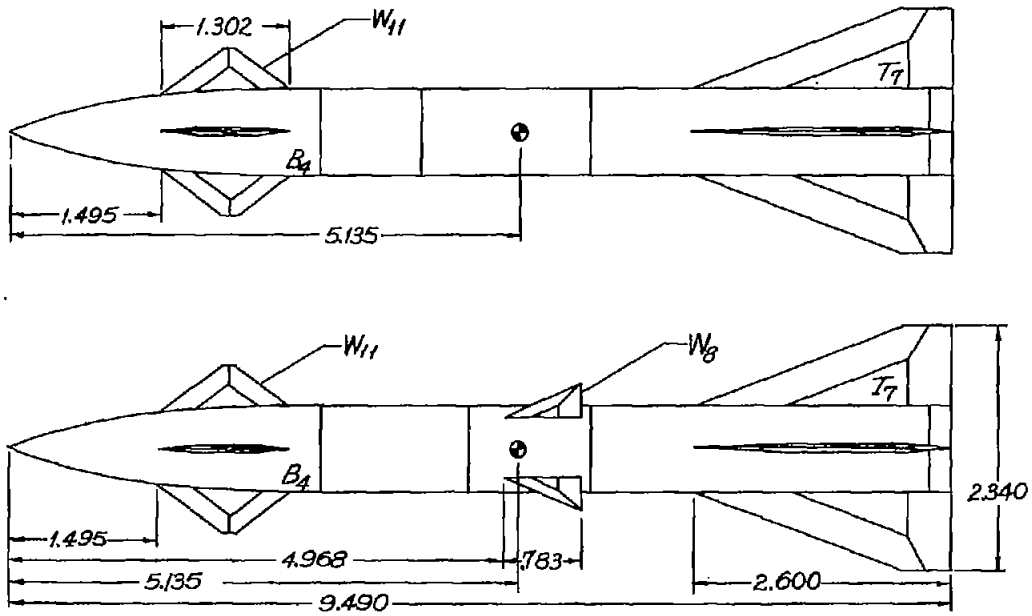

Surface	$(t/c)_R$	$(t/c)_T$	L.E. sweep angle	T.E. sweep angle	Aspect ratio
W_{11}	.048	.119	54°	-54°	1.29
T_7	.024	.027	70°	0°	1.10

NACA

Figure 1.- Concluded.

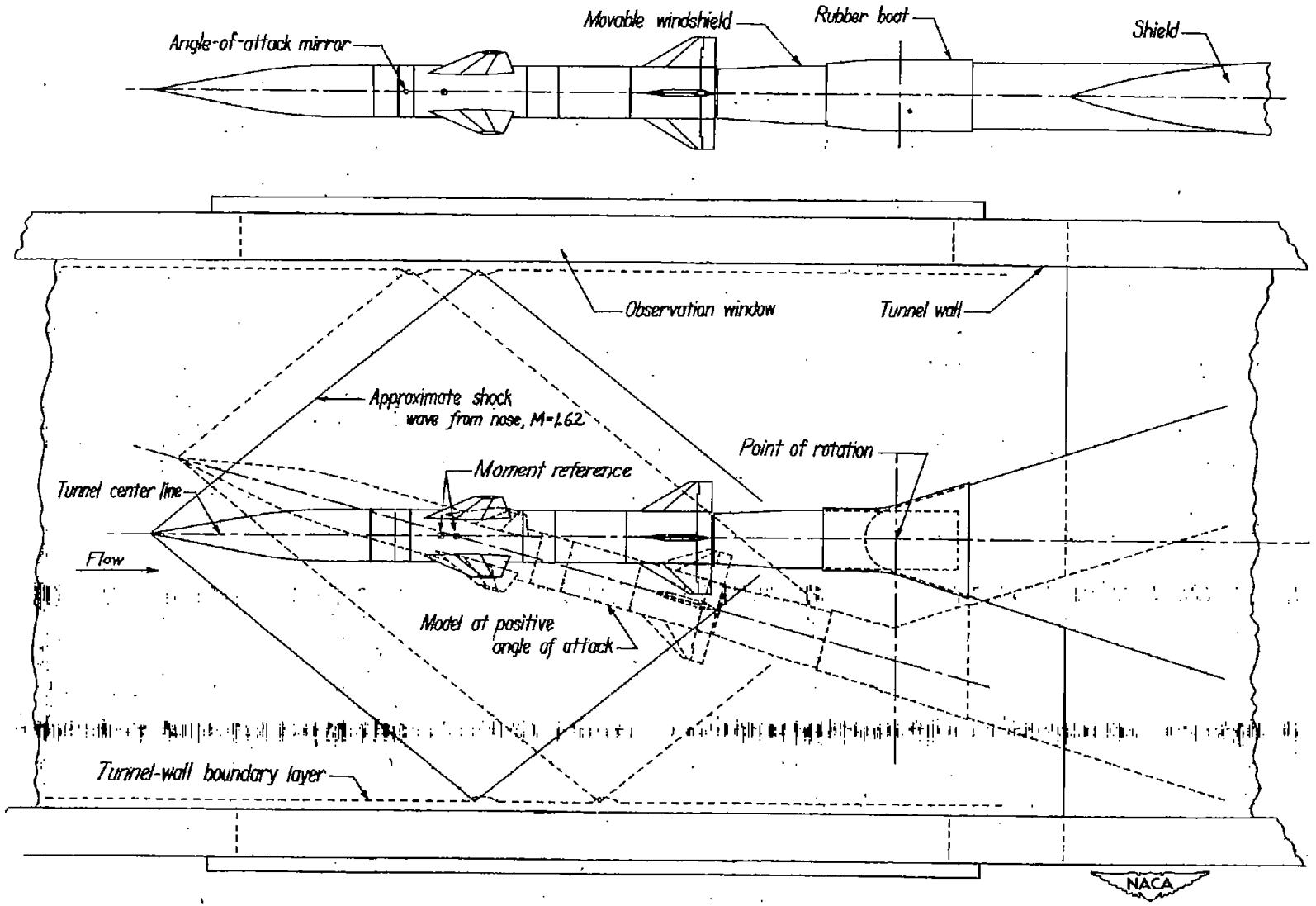

Figure 2.- Model installation in tunnel.

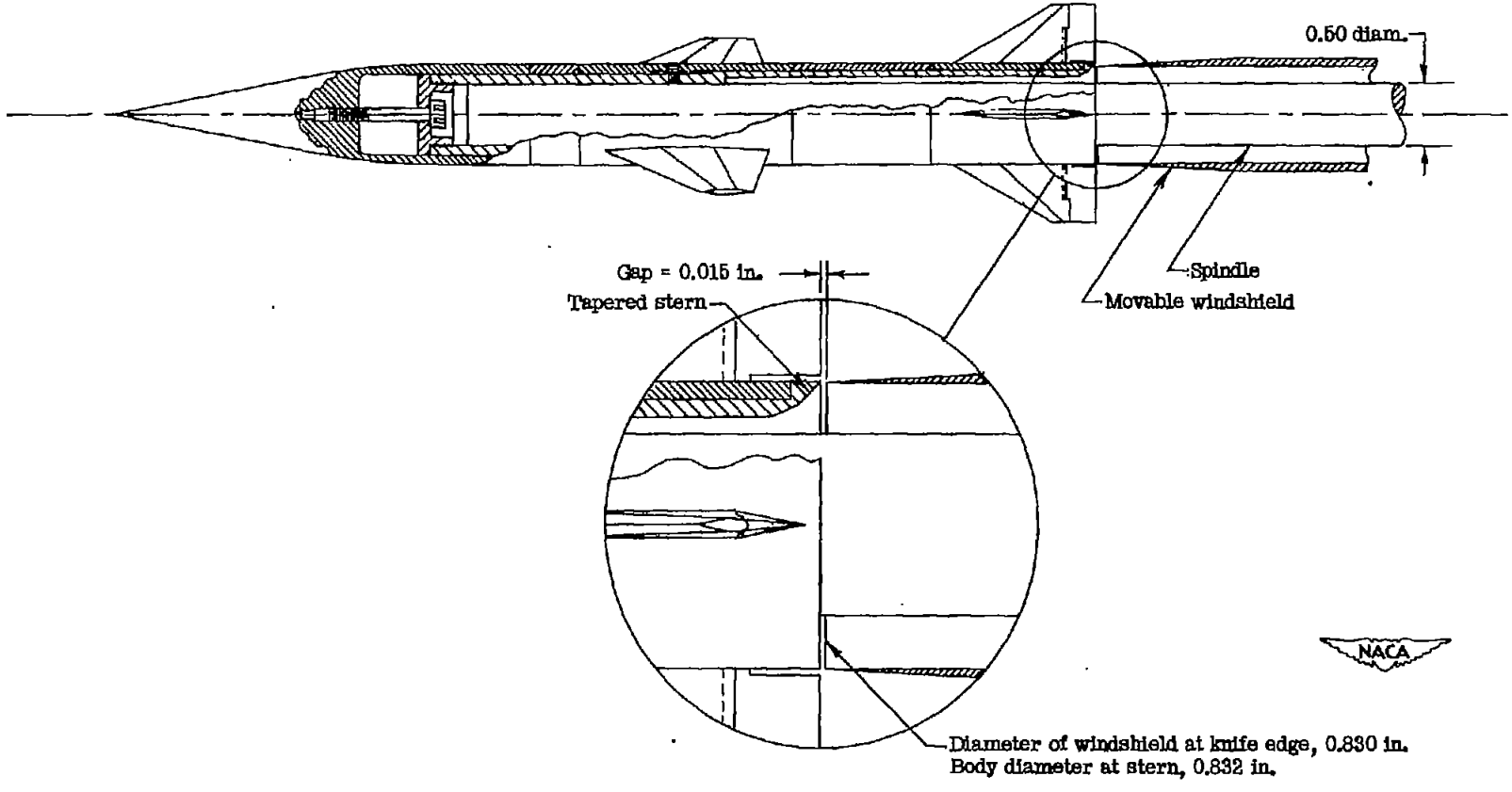

Figure 3.- Cross section of model body and stern detail.

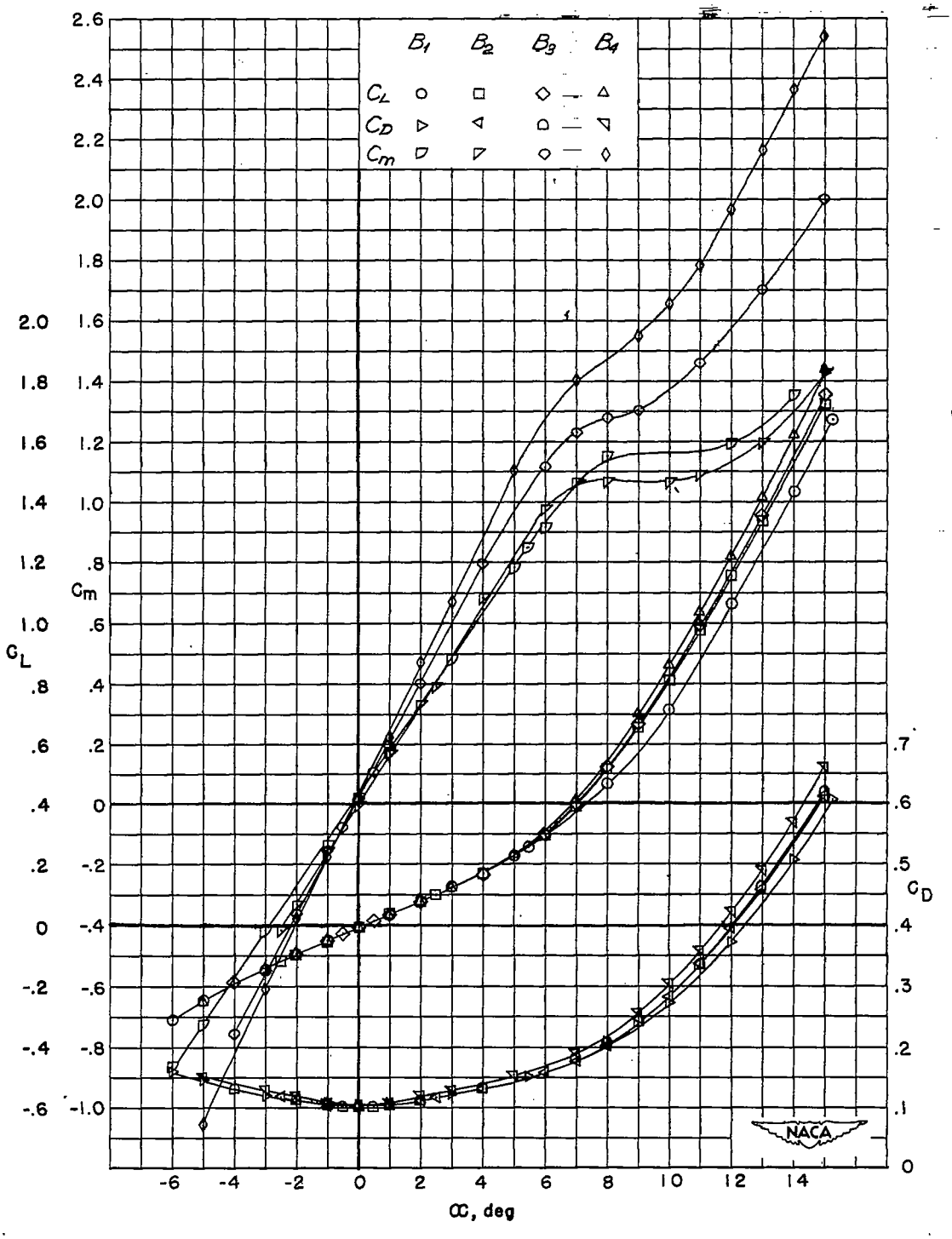

(a) B_1, B_2, B_3, and B_4.

Figure 4.- Lift, drag, and pitching-moment characteristics of B at M = 1.93.

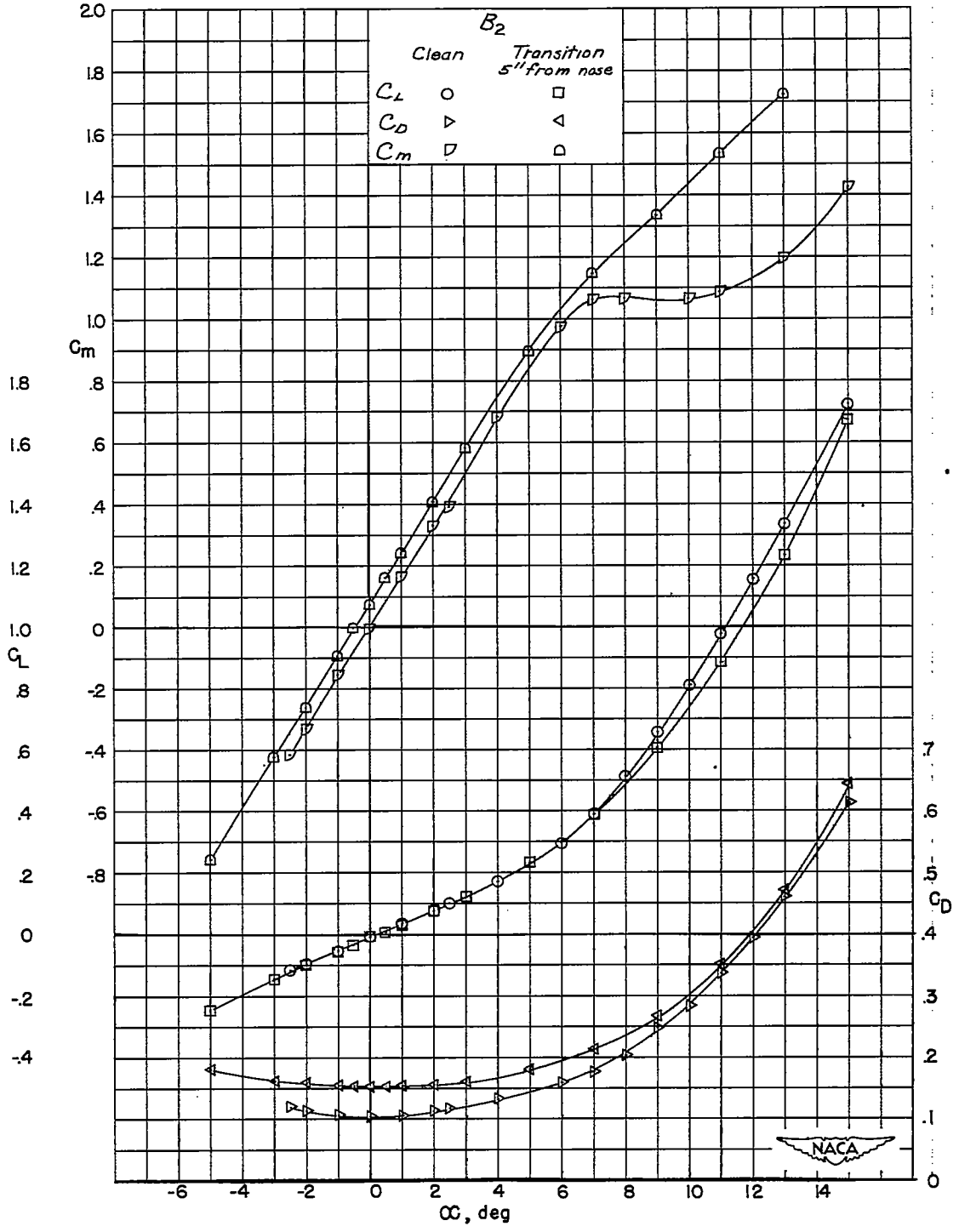

(b) B_2 (with and without transition).

Figure 4.- Continued.

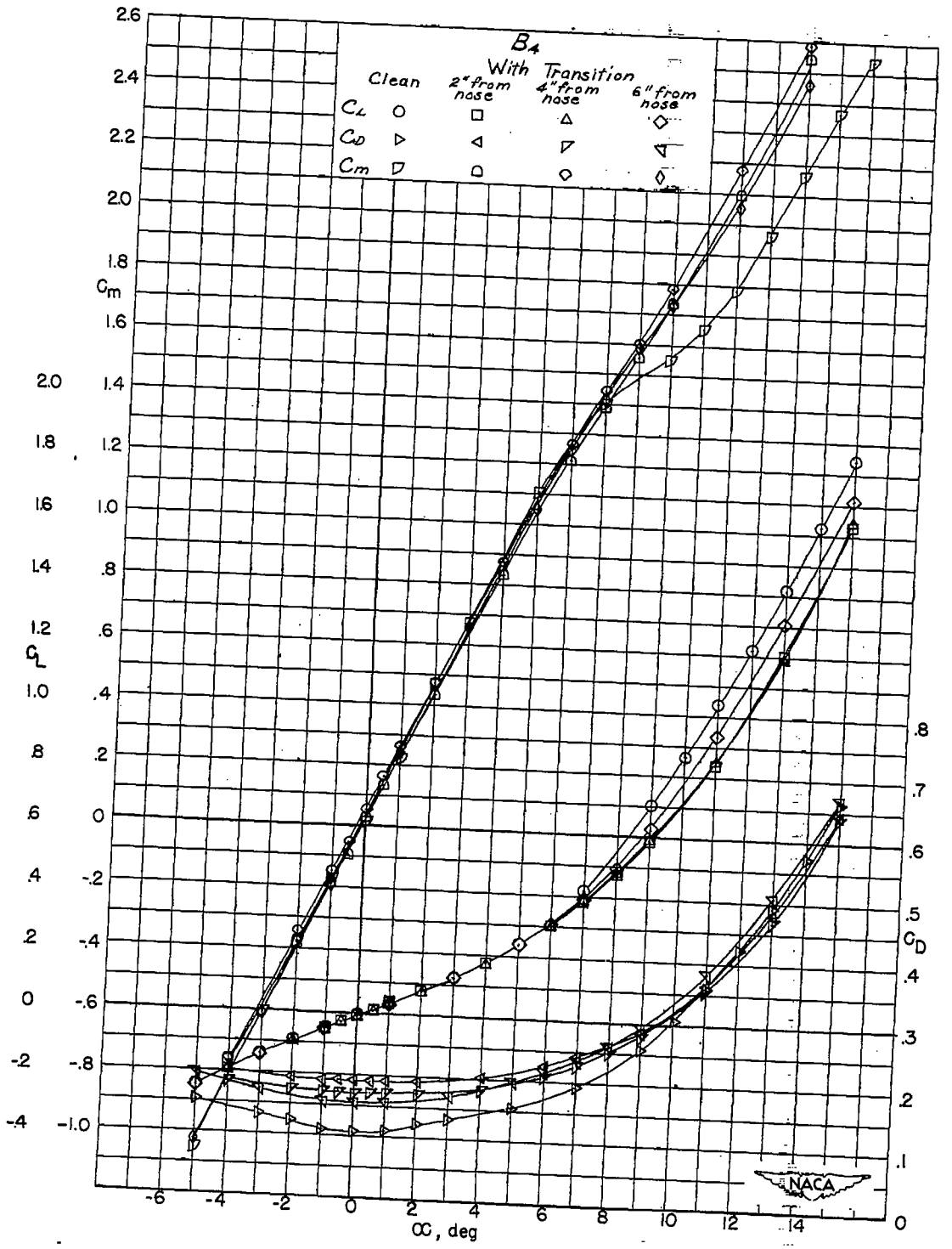

(c) B_4 (with and without transition).

Figure 4.- Concluded.

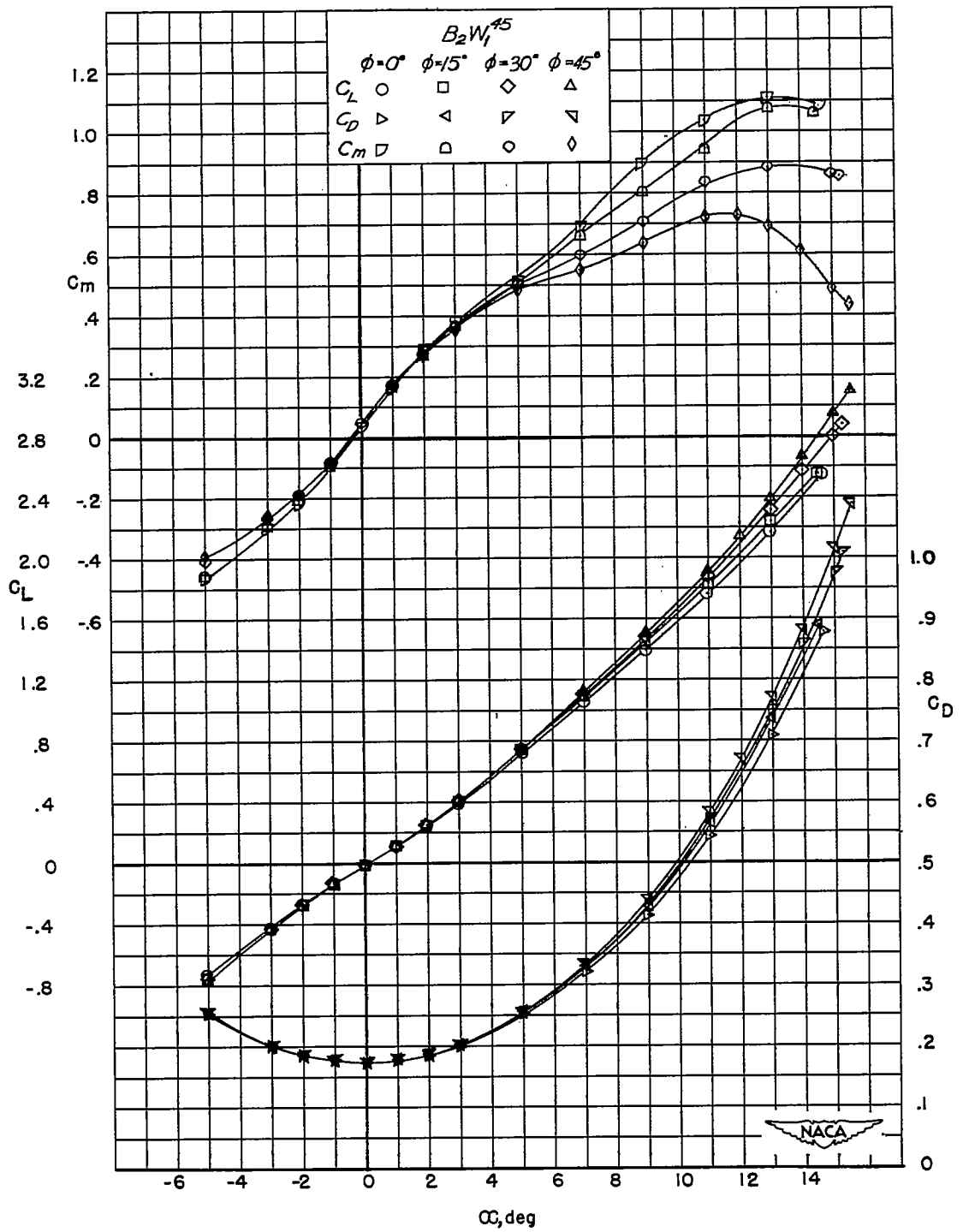

(a) $B_2W_1^{45}$.

Figure 5.- Lift, drag, and pitching-moment characteristics of BW at M = 1.93.

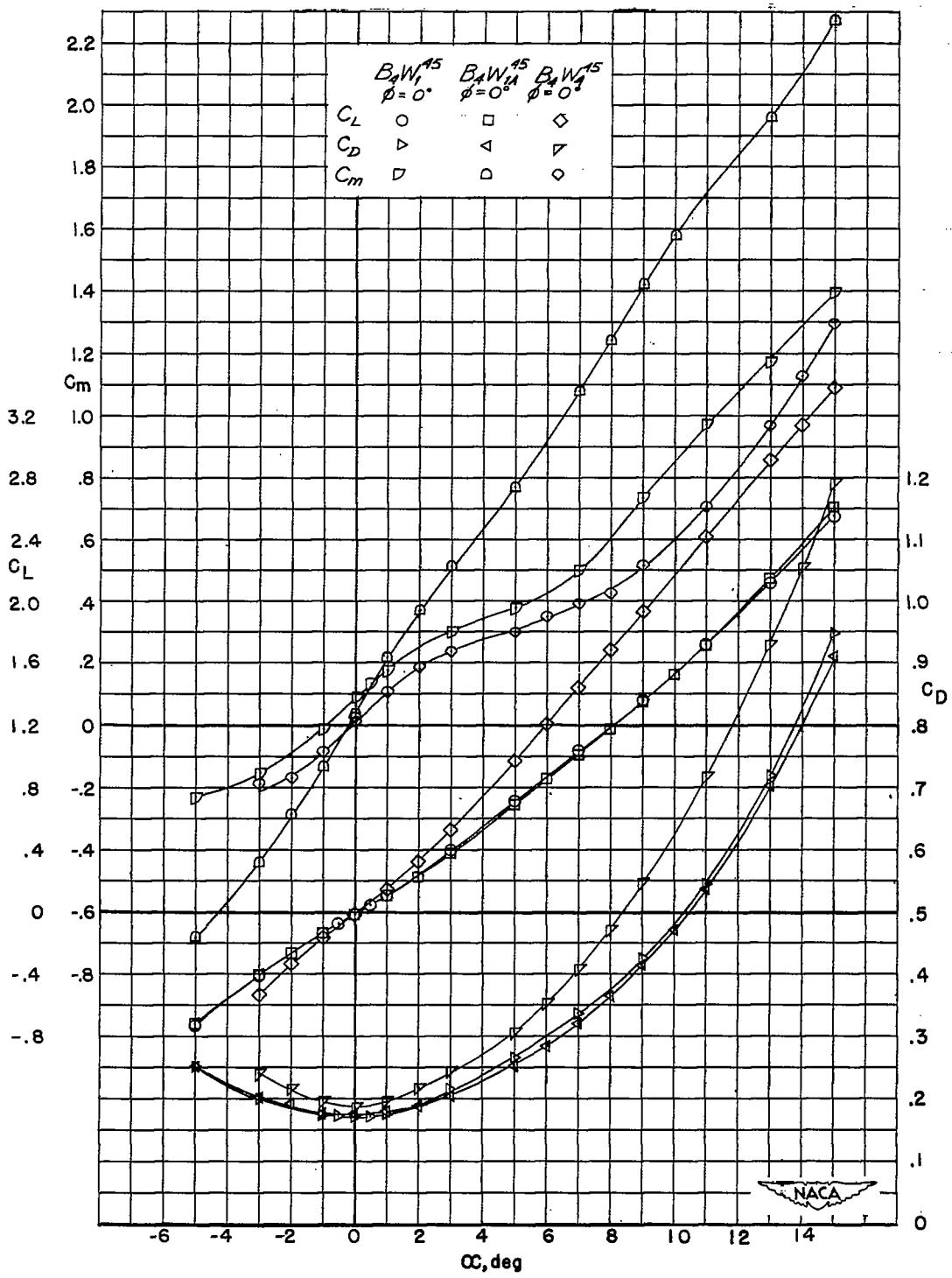

(b) $B_4W_1{}^{45}$, $B_4W_{1A}{}^{45}$, and $B_4W_4{}^{45}$.

Figure 5.- Continued.

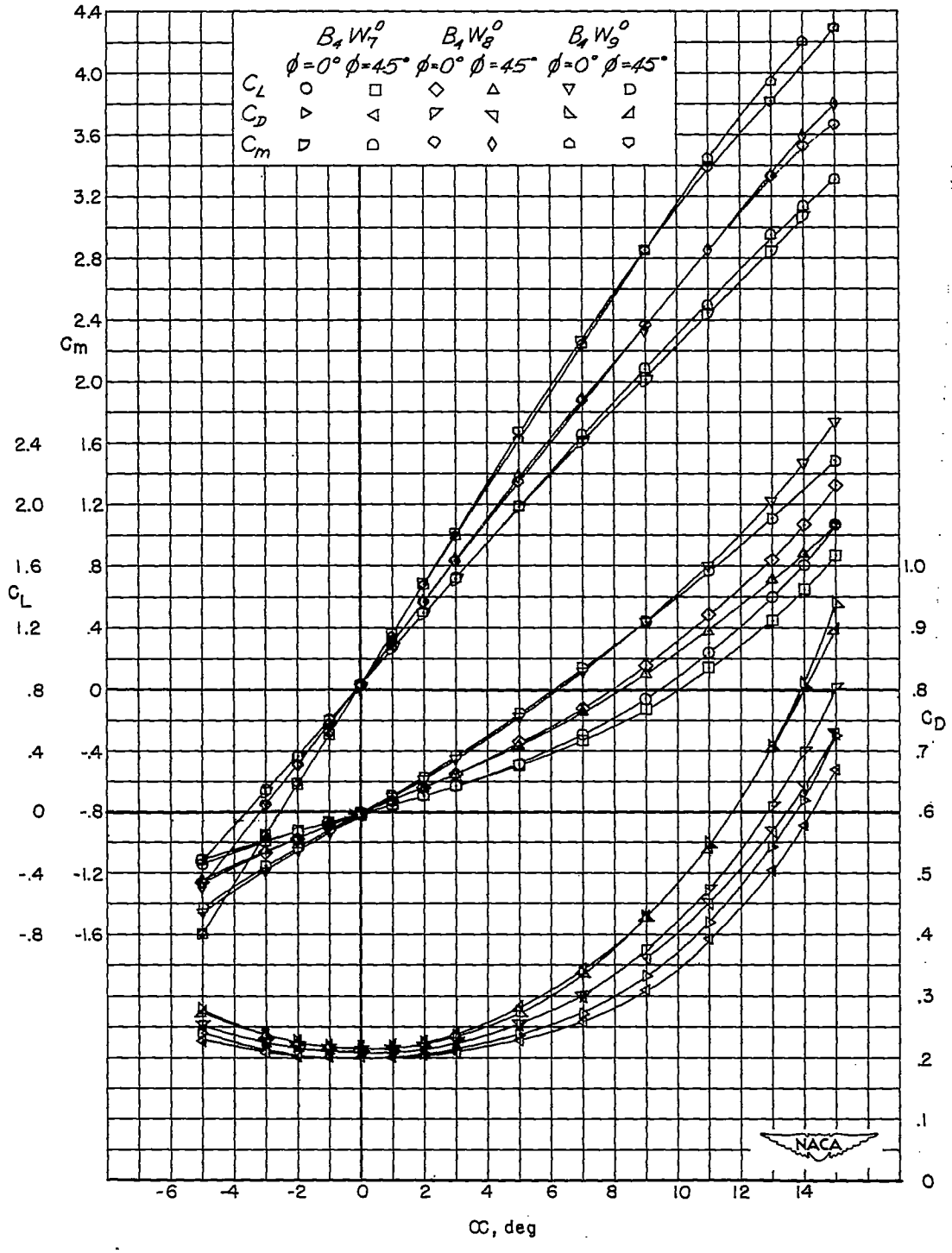

(c) $B_4W_7^0$, $B_4W_8^0$, and $B_4W_9^0$.

Figure 5.- Continued.

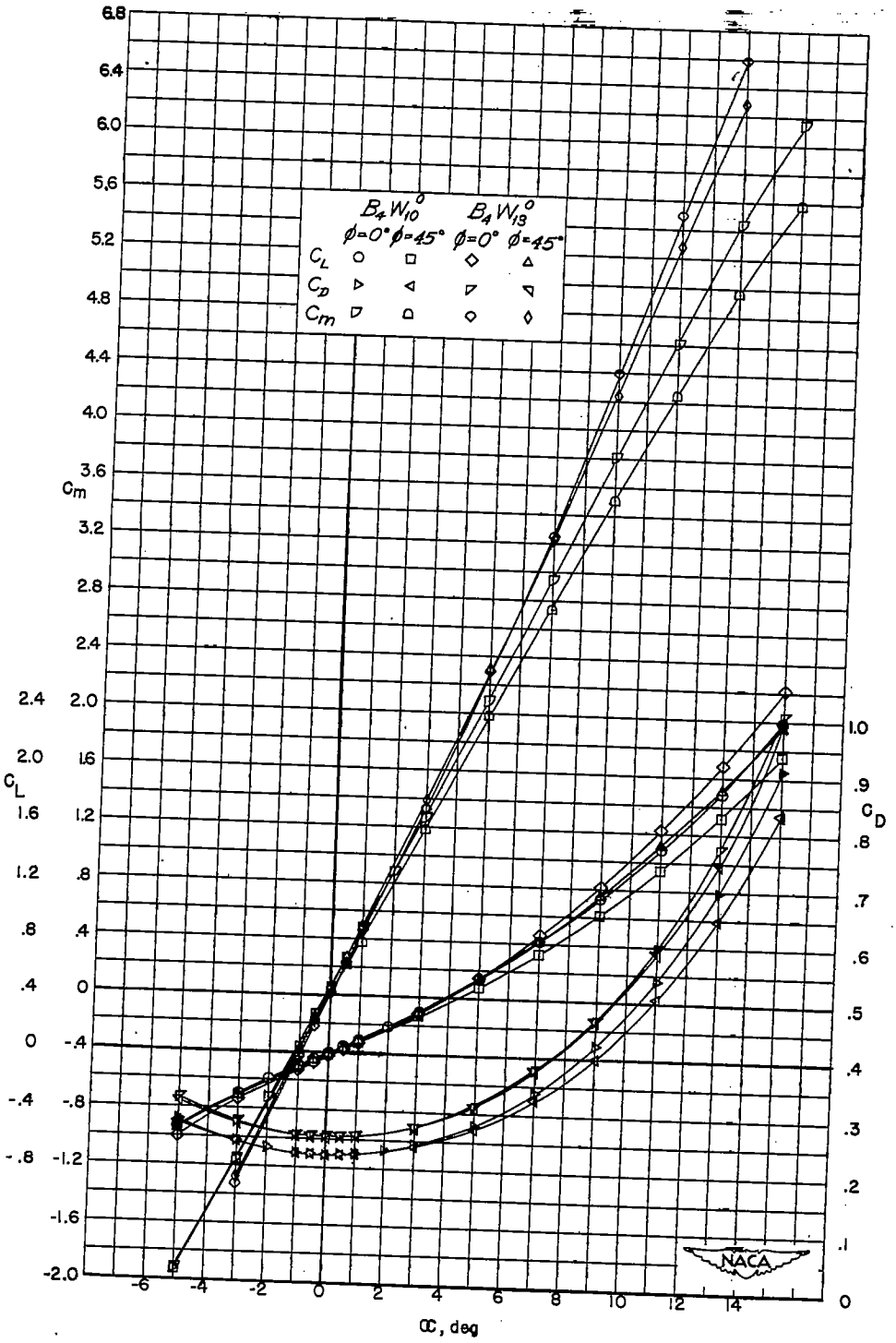

(d) $B_4W_{10}^0$ and $B_4W_{13}^0$.

Figure 5.- Continued.

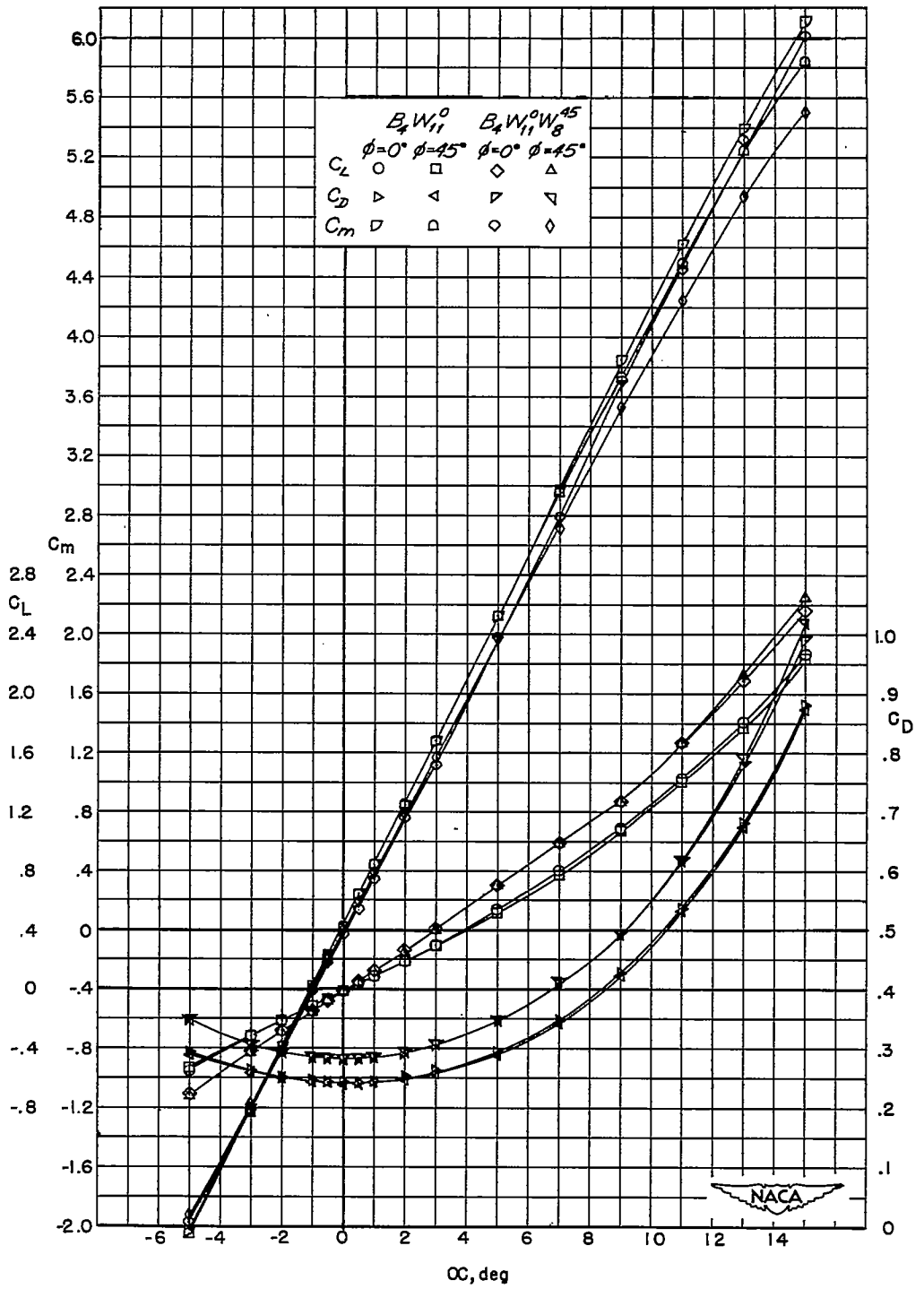

(e) $B_4W_{11}^0$ and $B_4W_{11}^0W_8^{45}$.

Figure 5.- Concluded.

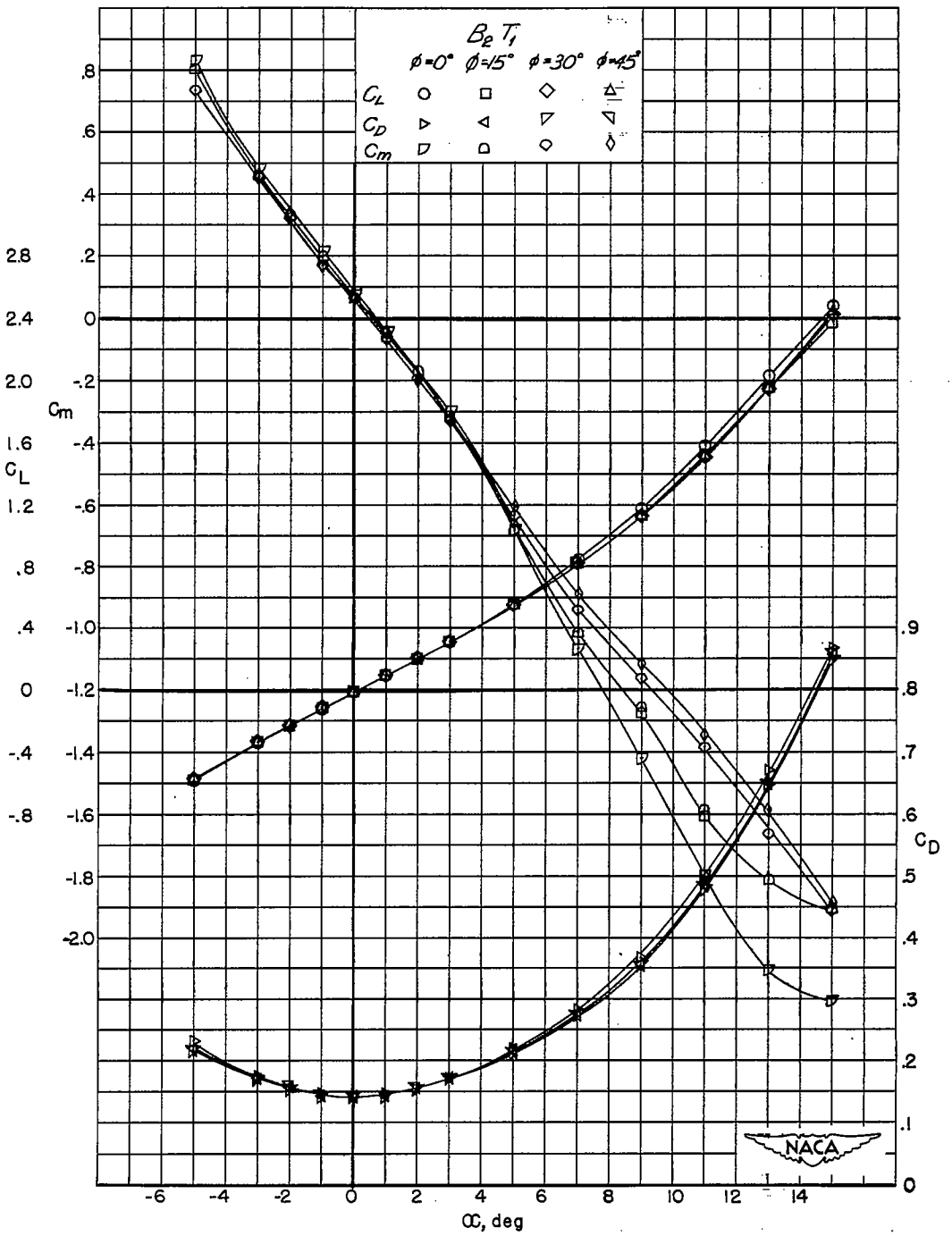

(a) B_2T_1.

Figure 6.- Lift, drag, and pitching-moment characteristics of BT at M = 1.93.

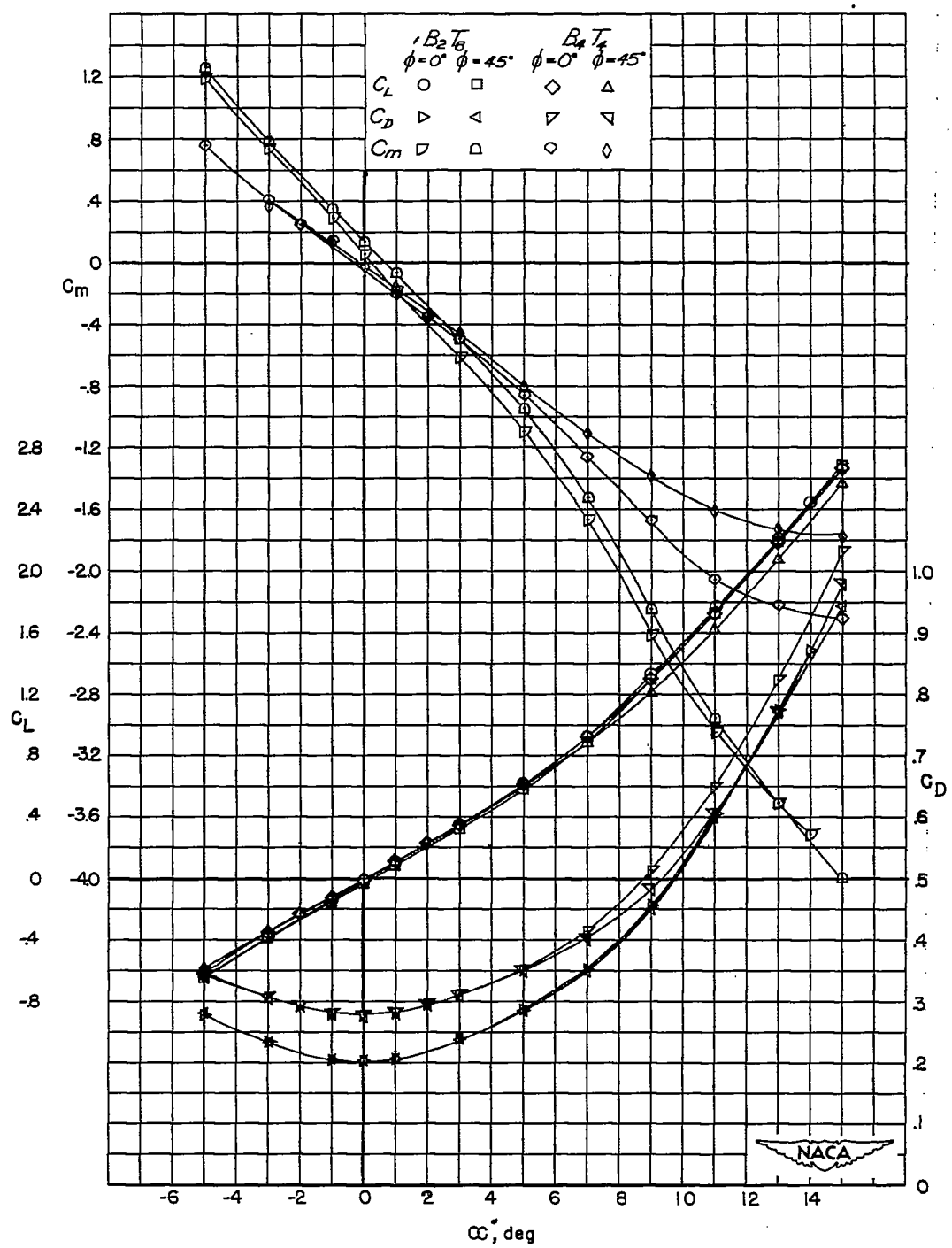

(b) B_2T_6 and B_4T_4.

Figure 6.- Continued.

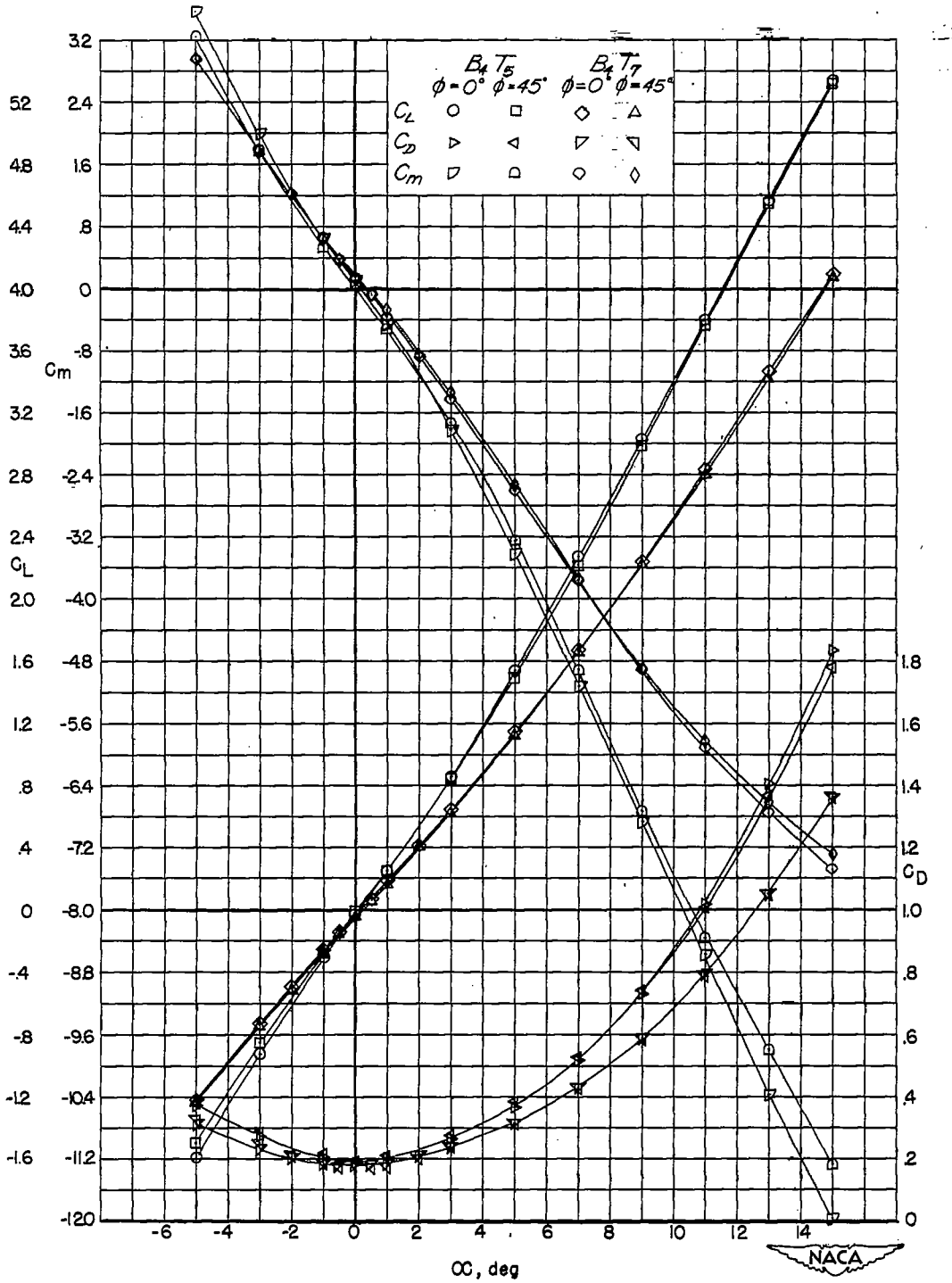

(c) B_4T_5 and B_4T_7.

Figure 6.- Concluded.

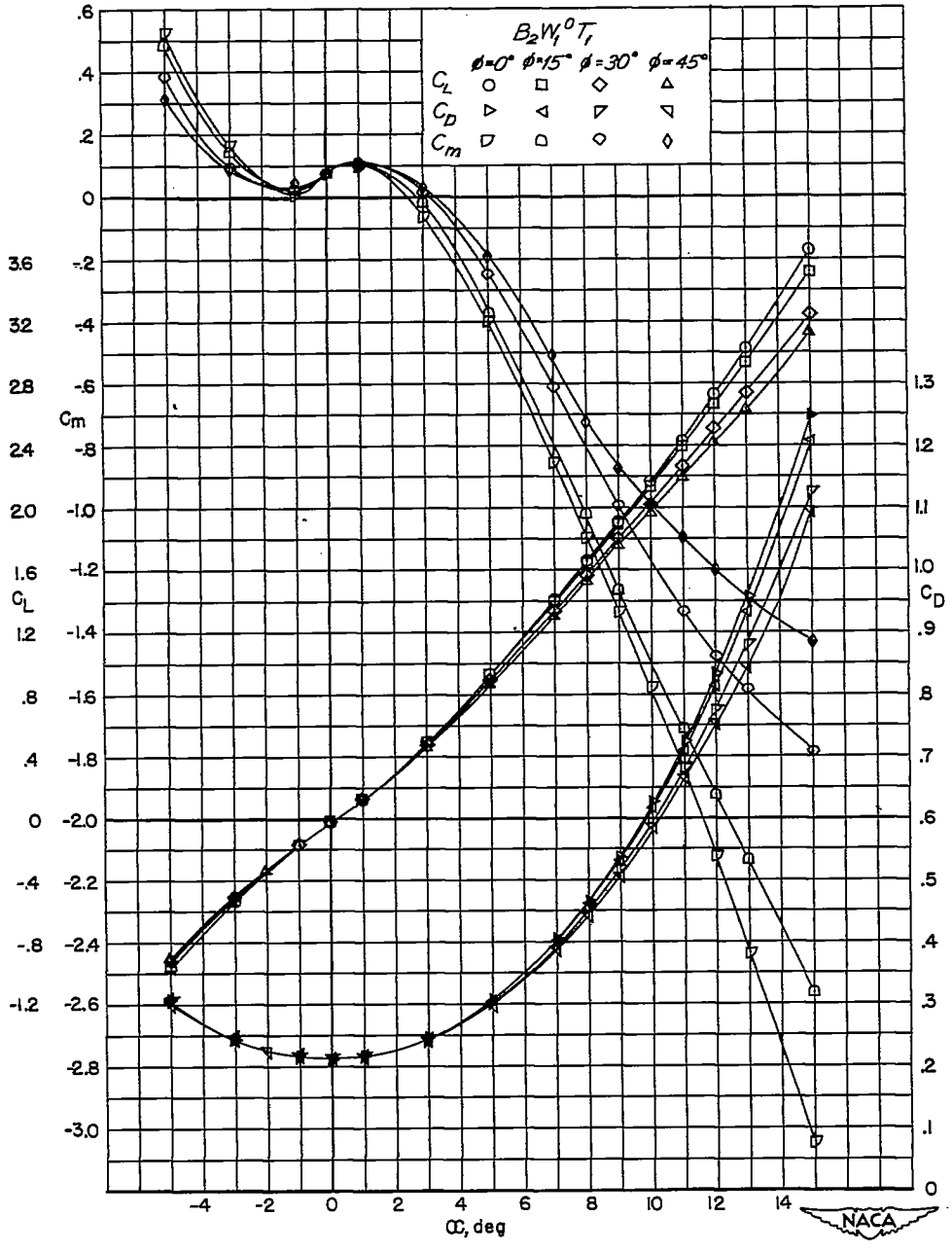

(a) $B_2W_1{}^0T_1$.

Figure 7.- Lift, drag, and pitching-moment characteristics of BWT at M = 1.93.

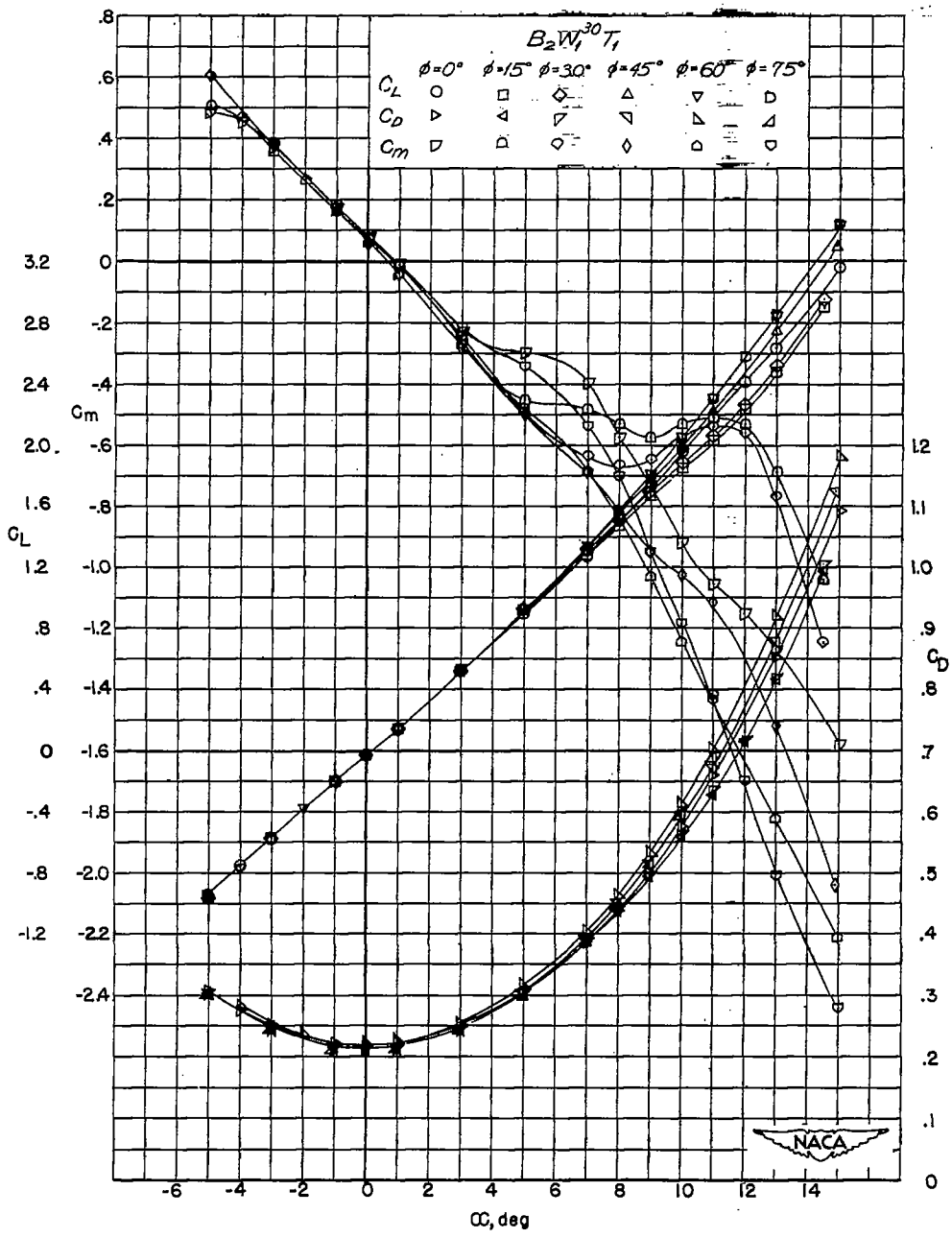

(b) $B_2W_1^{30}T_1$.

Figure 7.- Continued.

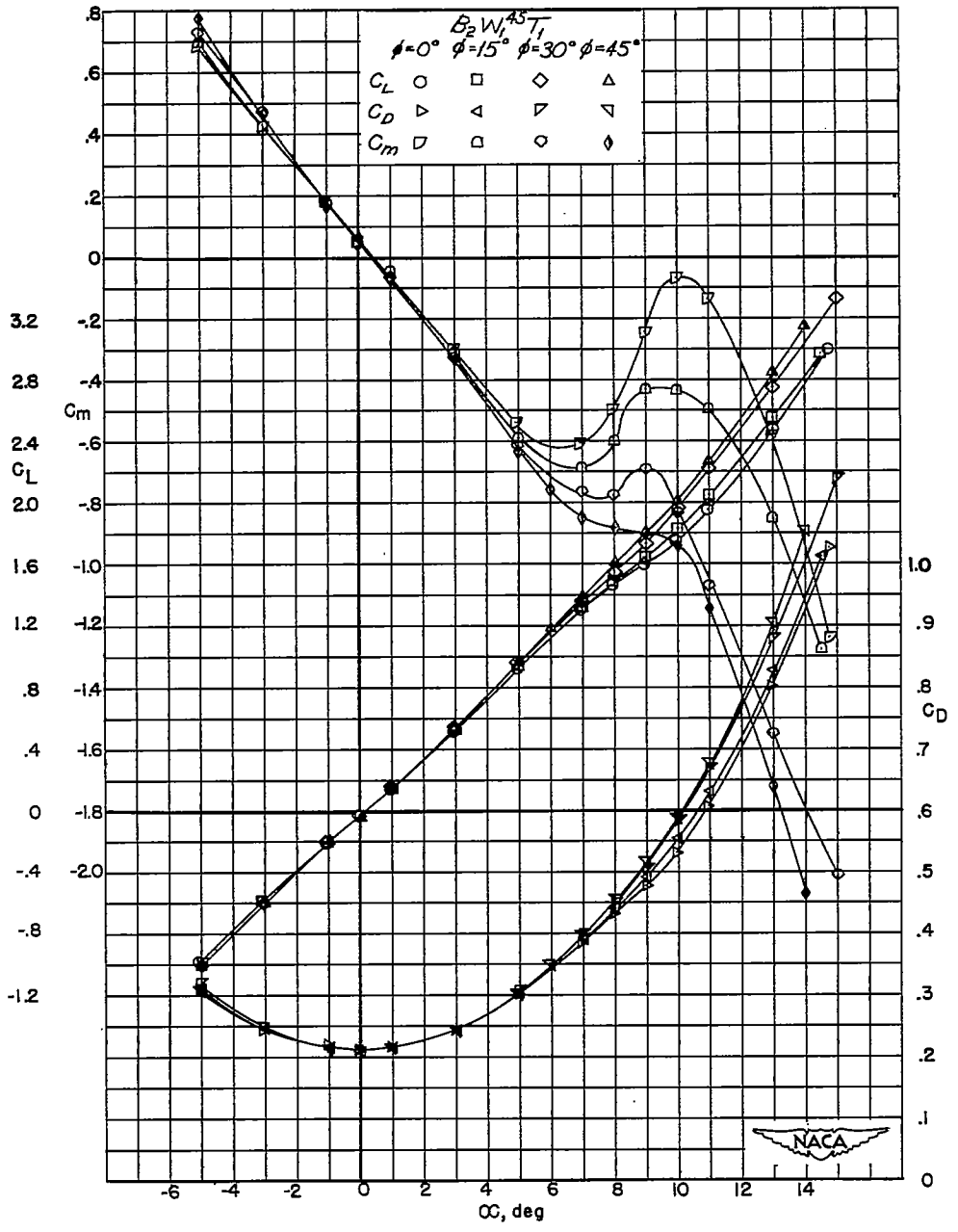

(c) $B_2W_1{}^{45}T_1$.

Figure 7.- Continued.

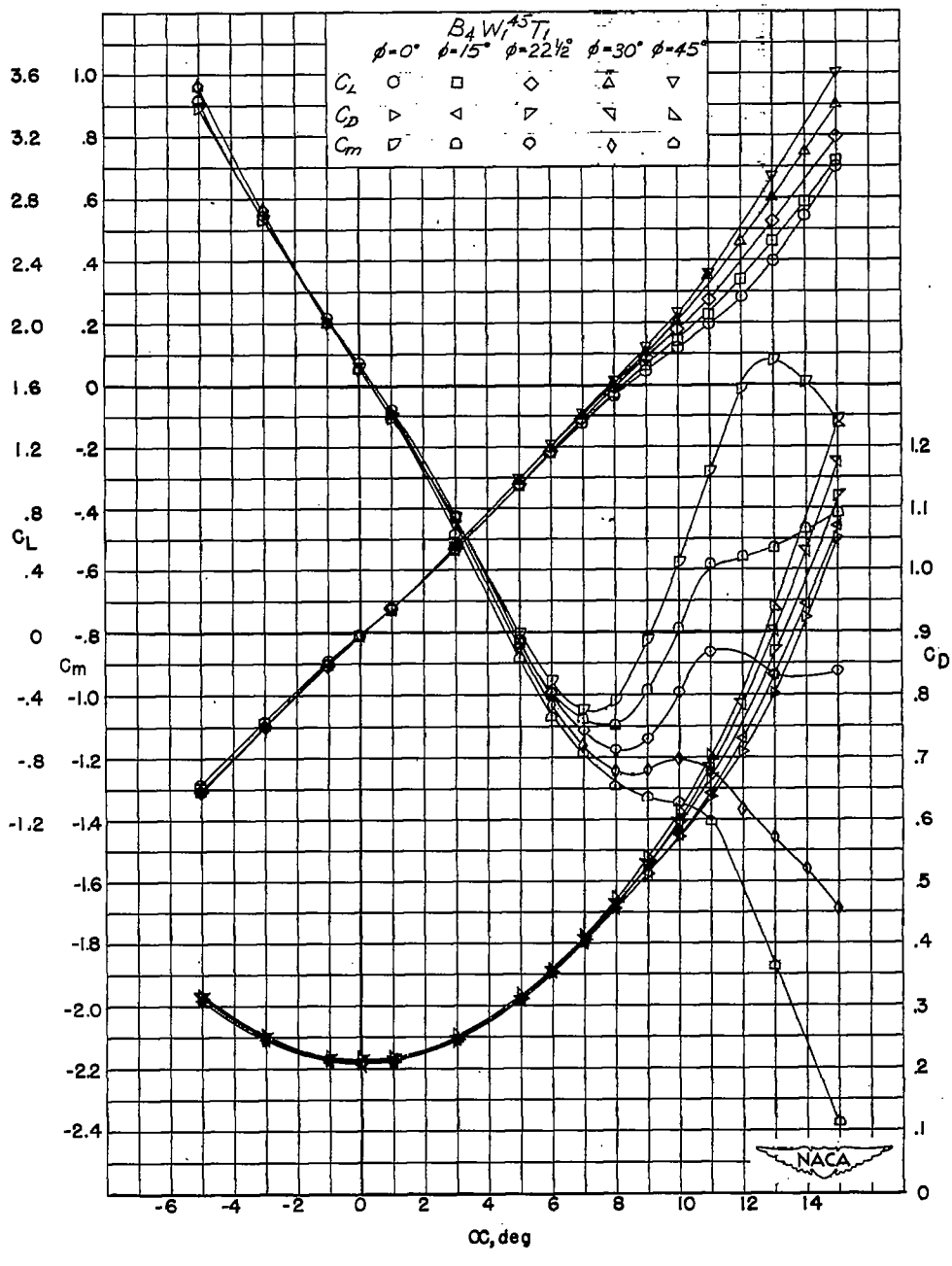

(d) $B_4W_1{}^{45}T_1$.

Figure 7.- Continued.

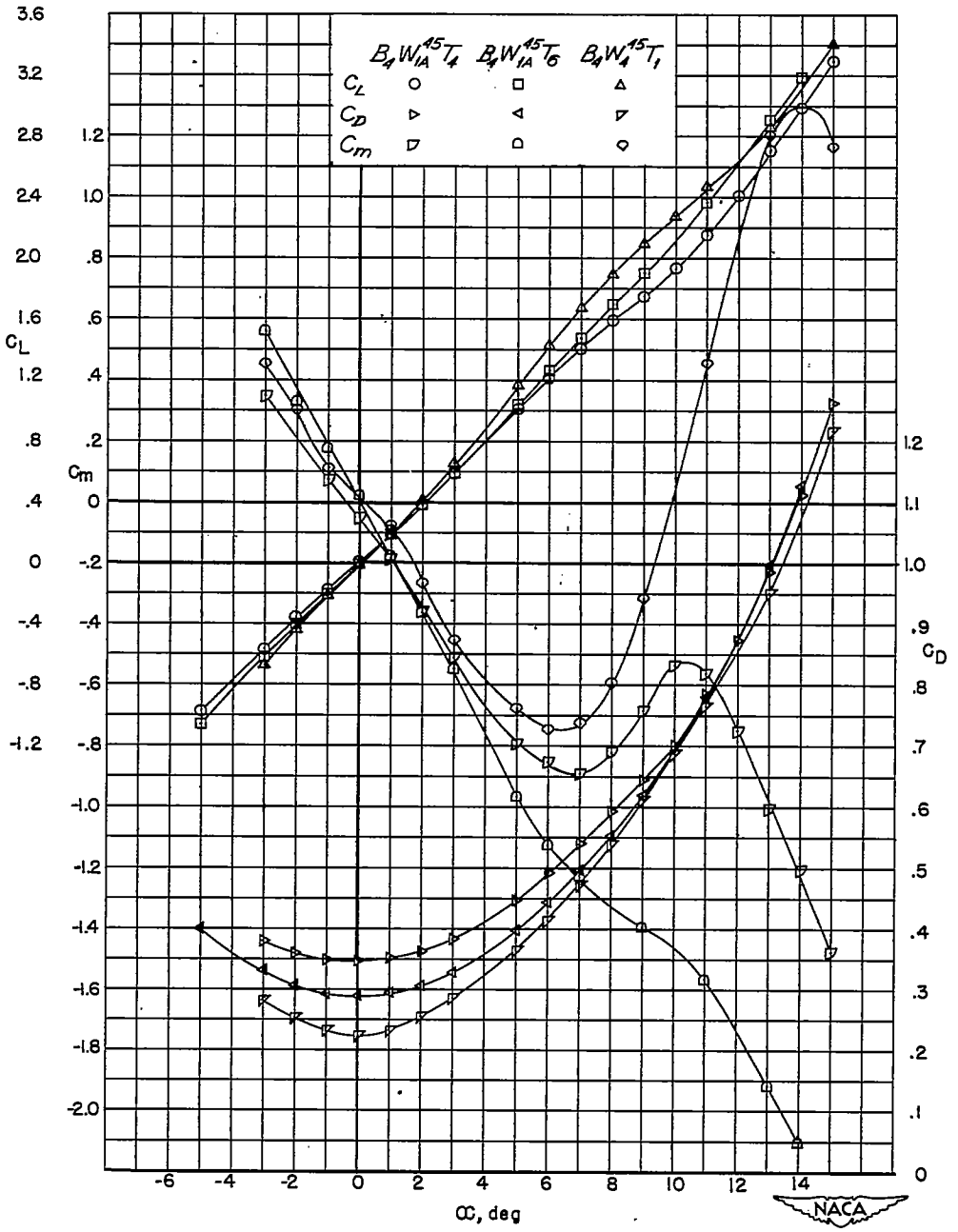

(e) $B_4W_{1A}{}^{45}T_4$, $B_4W_{1A}{}^{45}T_6$, and $B_4W_4{}^{45}T_1$.

Figure 7.- Continued.

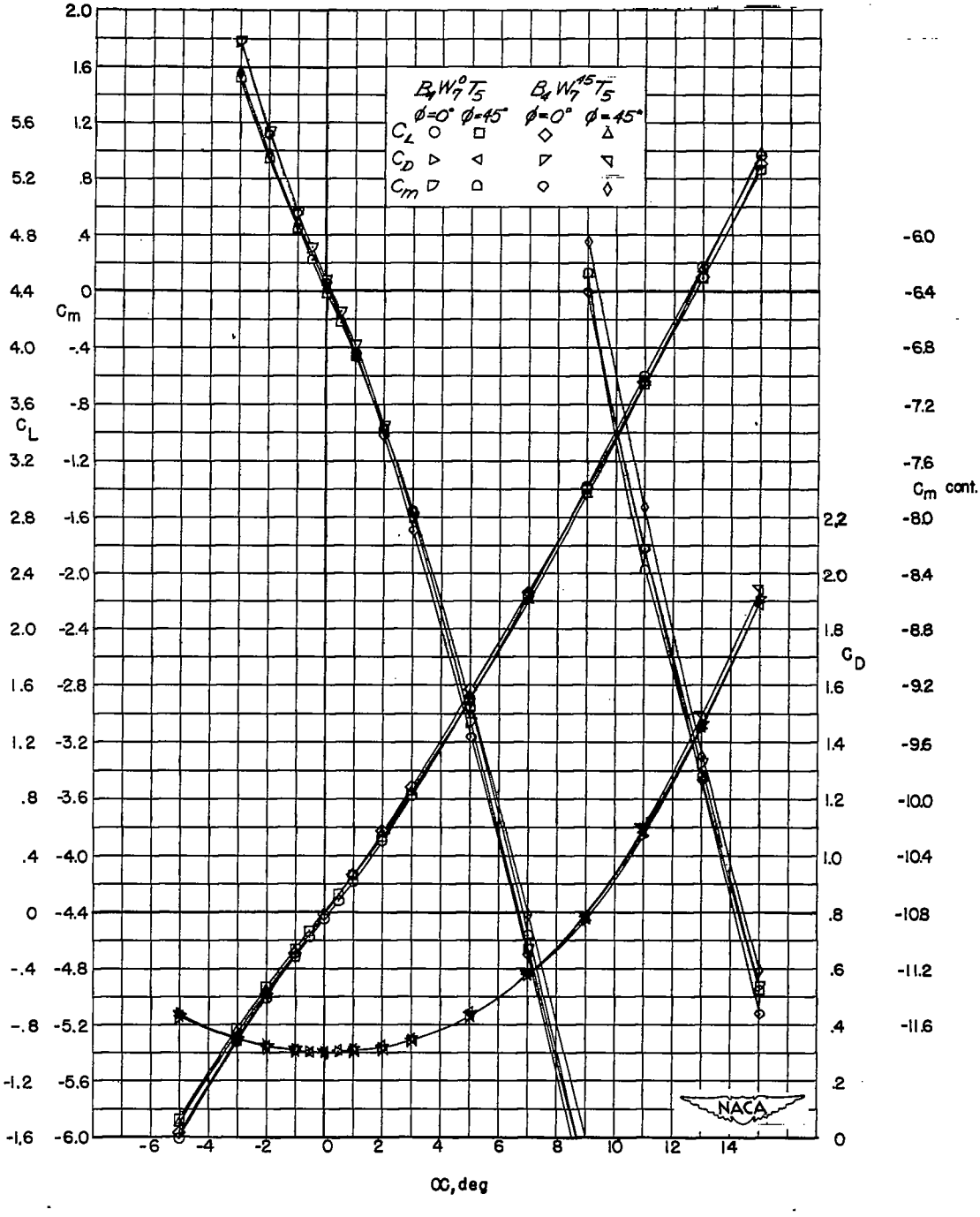

(f) $B_4W_7^0T_5$ and $B_4W_7^{45}T_5$.

Figure 7.- Continued.

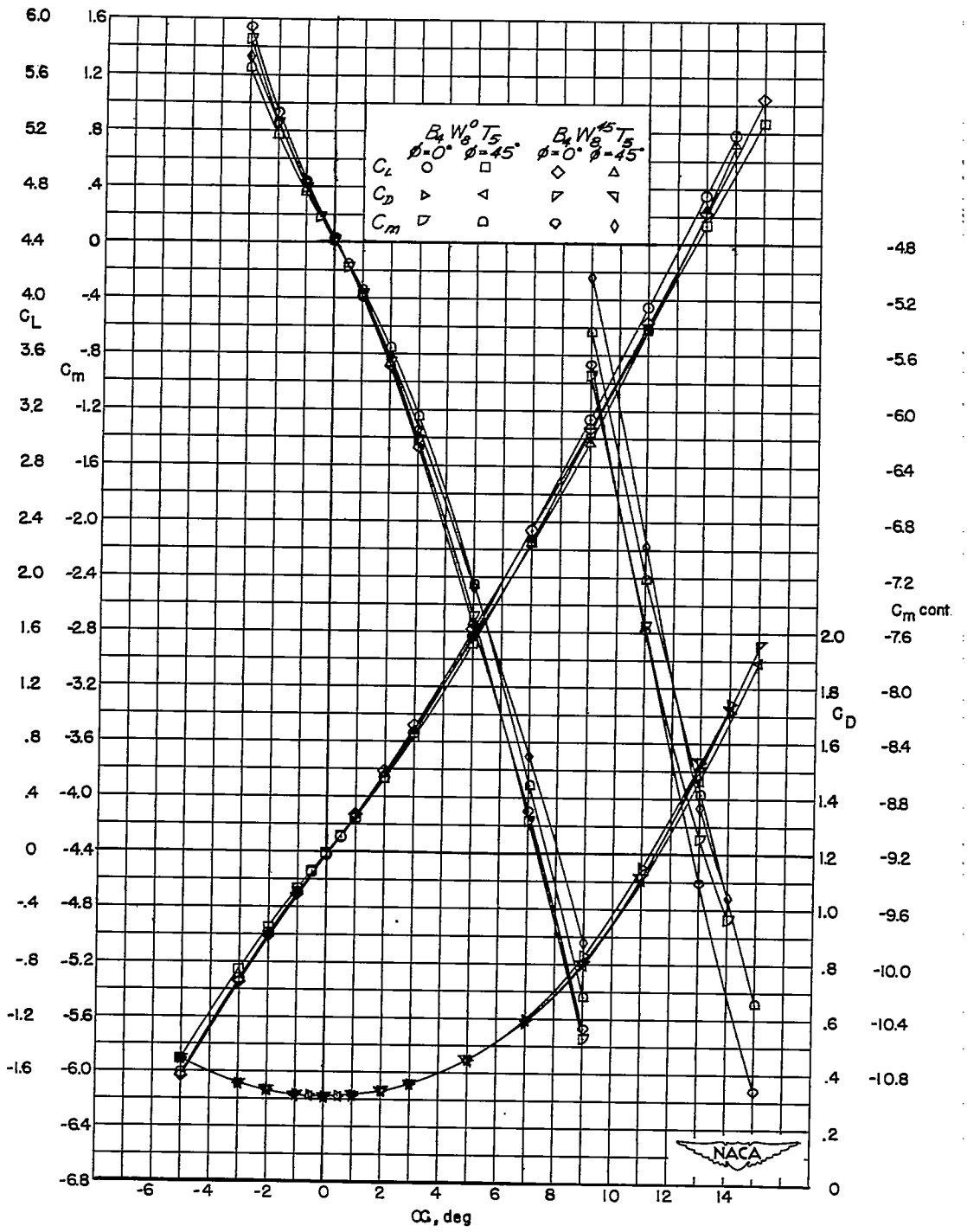

(g) $B_4W_8{}^0T_5$ and $B_4W_8{}^{45}T_5$.

Figure 7.- Continued.

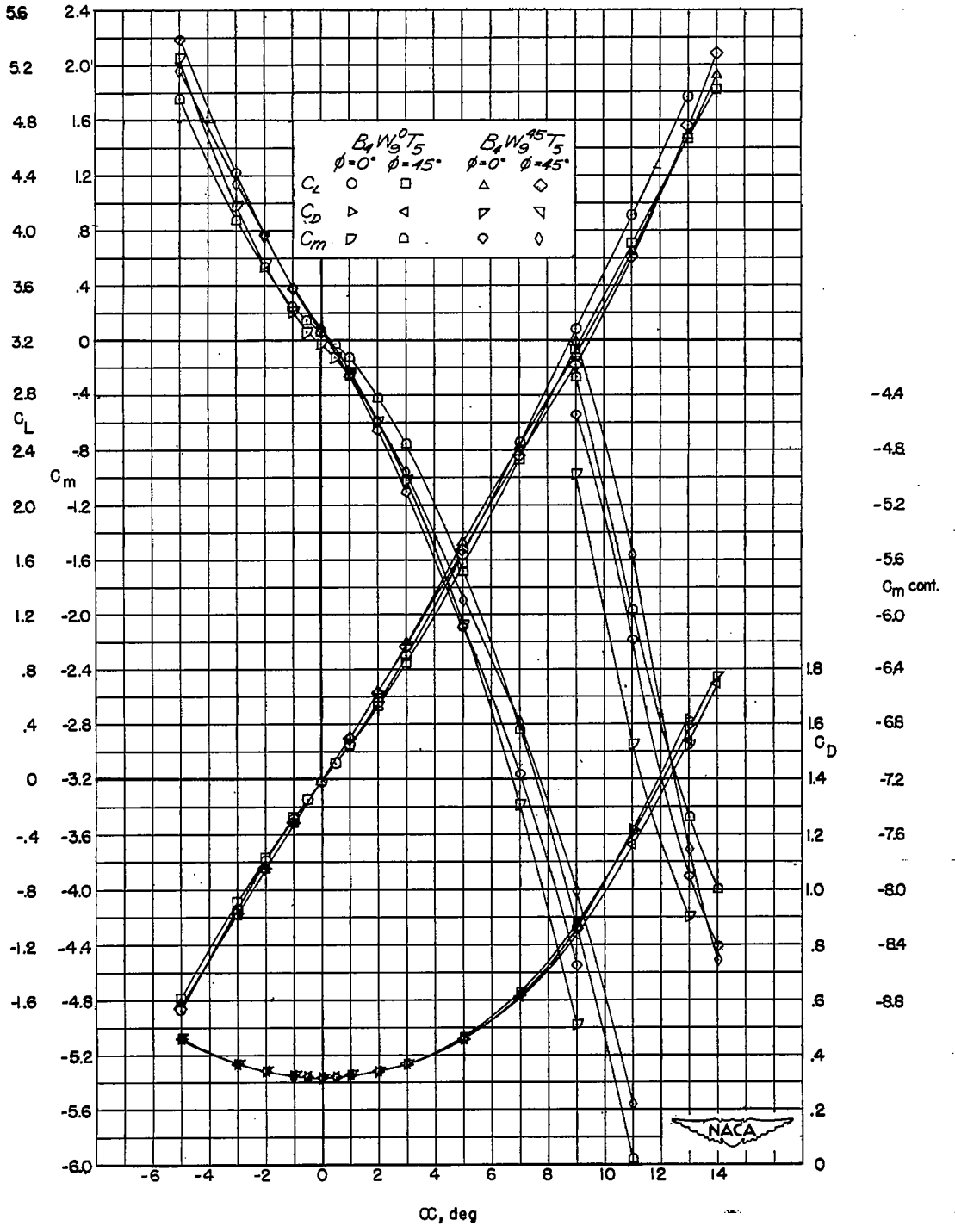

(h) $B_4W_9{}^0T_5$ and $B_4W_9{}^{45}T_5$.

Figure 7.- Continued.

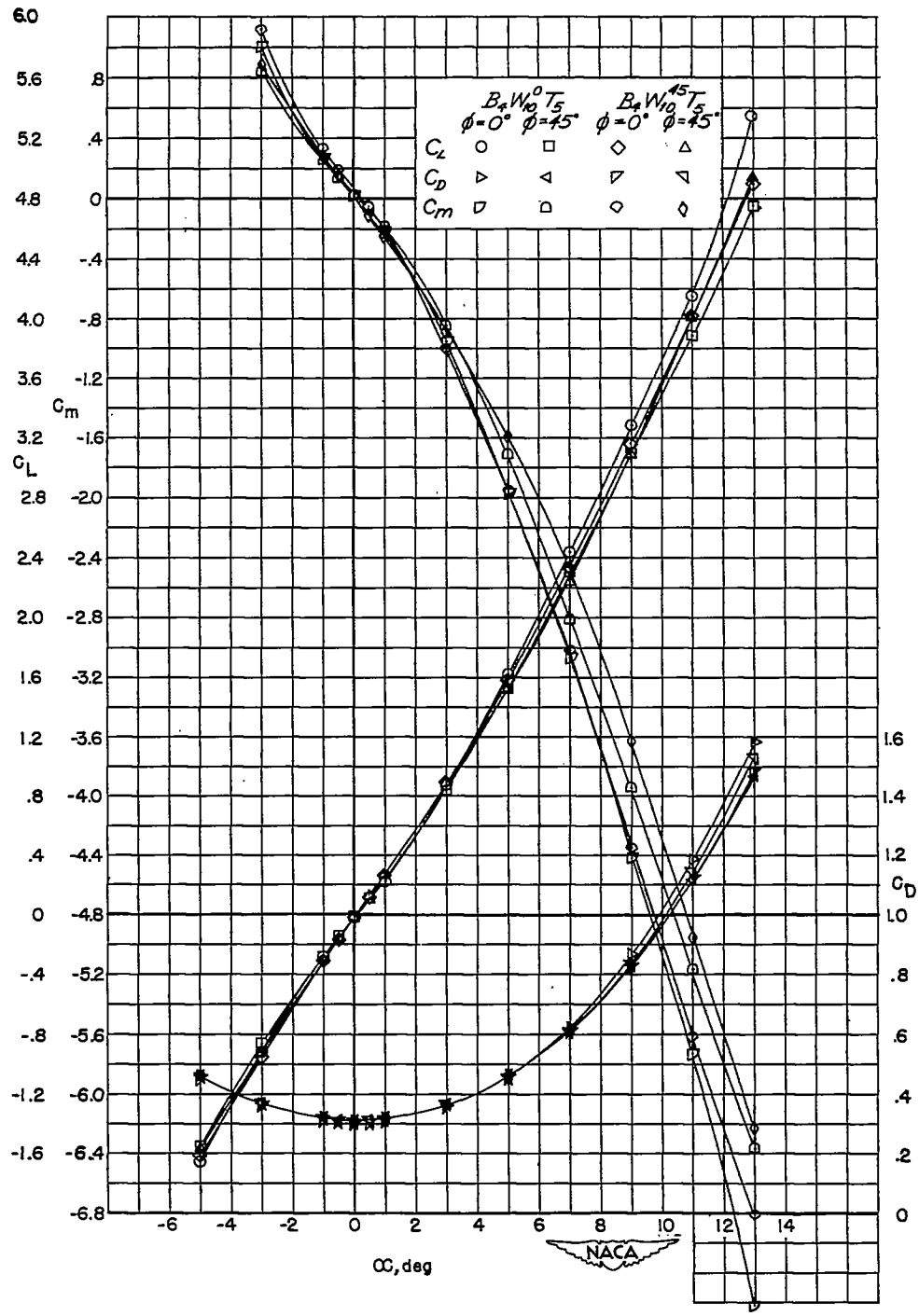

(i) $B_4W_{10}{}^0T_5$ and $B_4W_{10}{}^{45}T_5$.

Figure 7.- Continued.

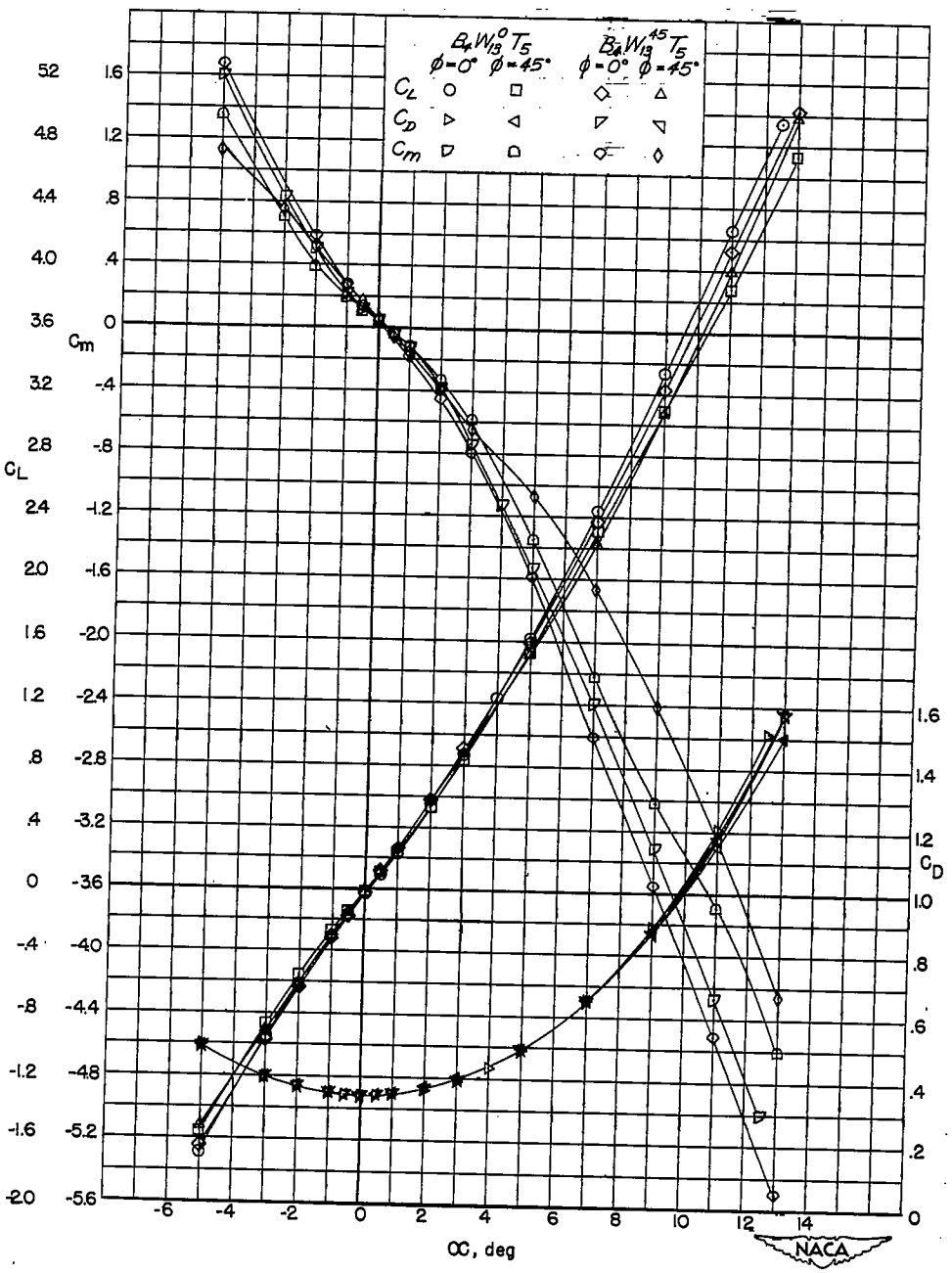

(j) $B_4W_{13}{}^0T_5$ and $B_4W_{13}{}^{45}T_5$.

Figure 7.- Continued.

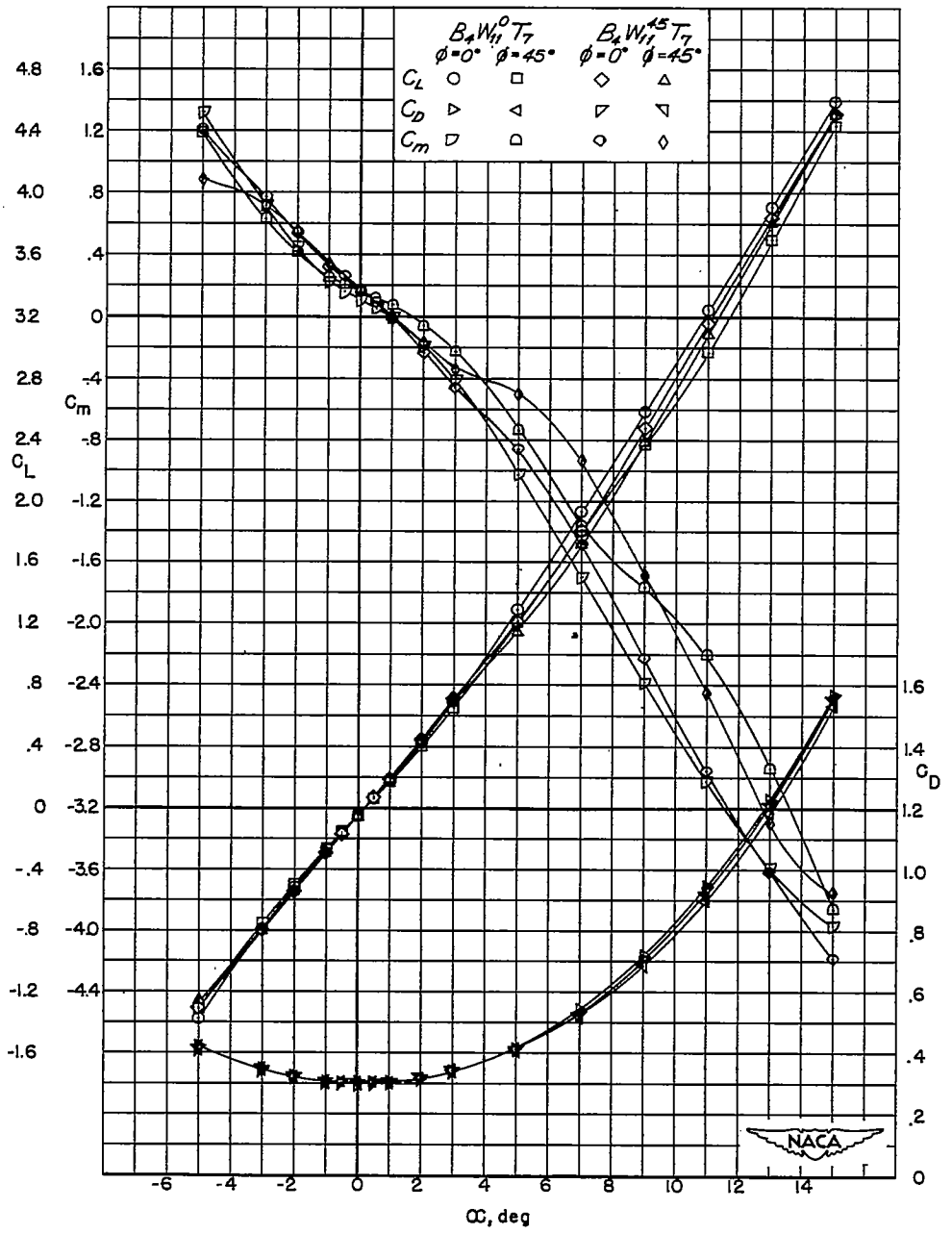

(k) $B_4W_{11}{}^{0}T_7$ and $B_4W_{11}{}^{45}T_7$.

Figure 7.- Continued.

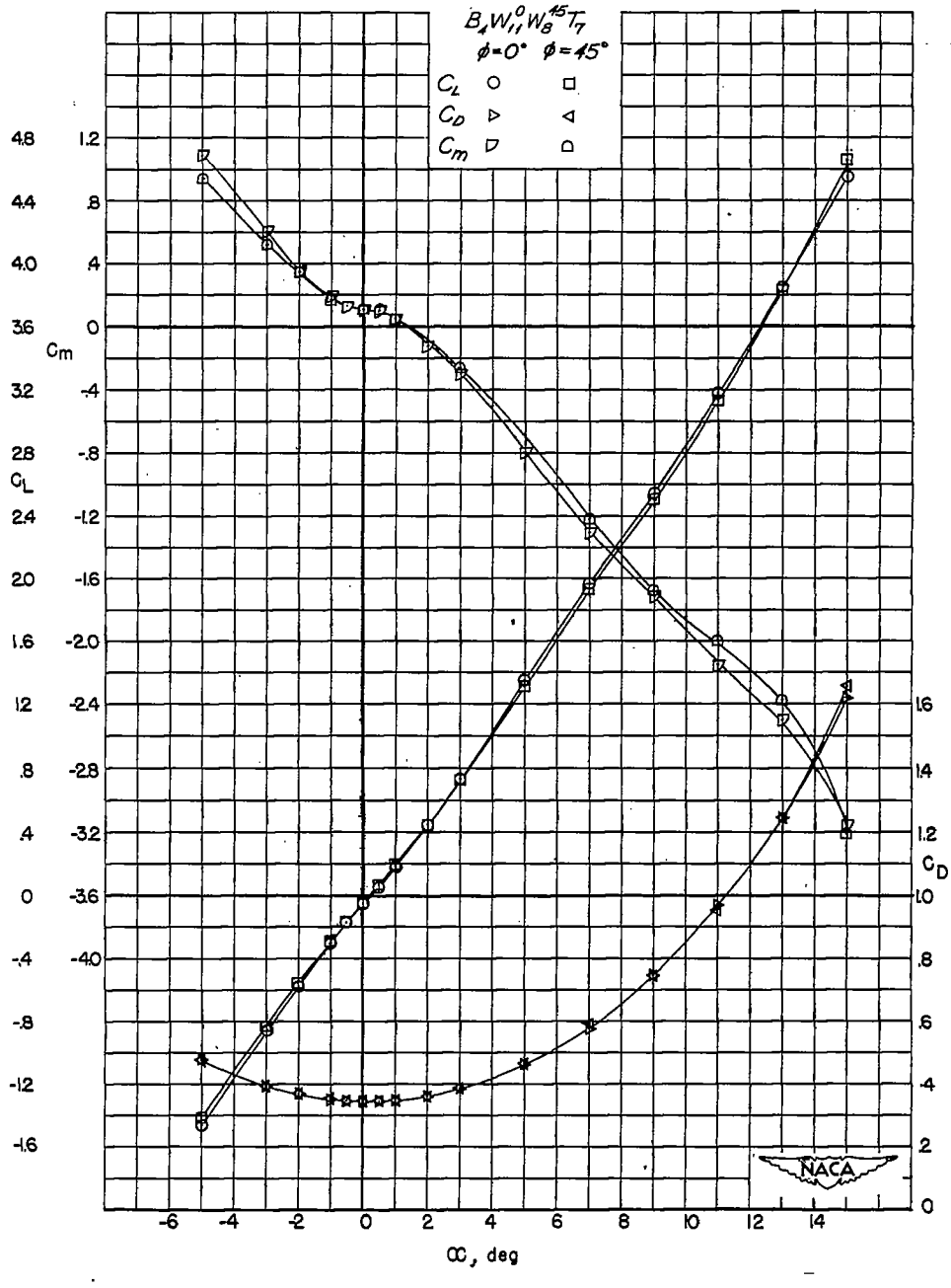

(l) $B_4W_{11}{}^{0}W_8{}^{45}T_7$.

Figure 7.- Concluded.

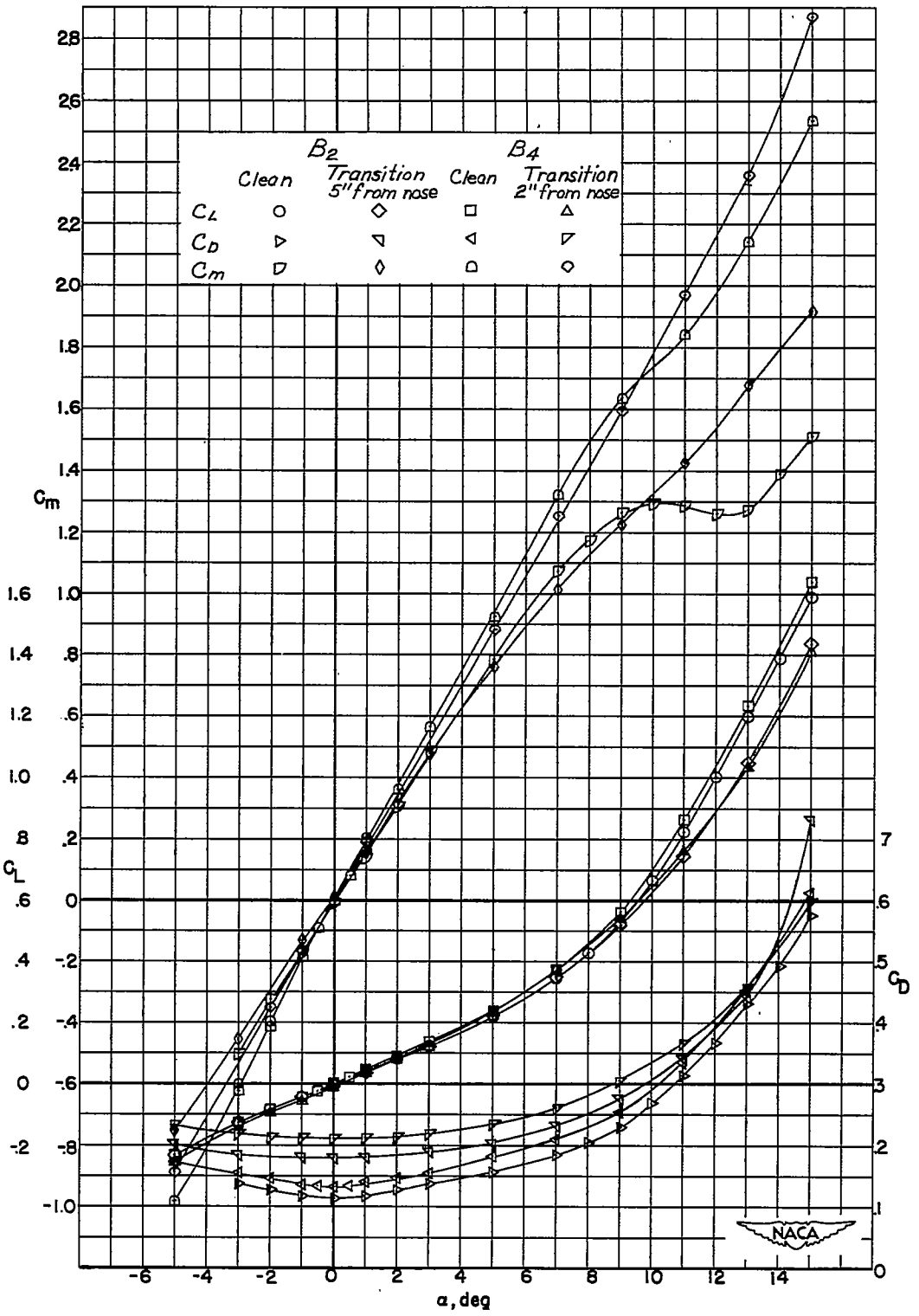

Figure 8.- Lift, drag, and pitching-moment characteristics of B at M = 1.62.

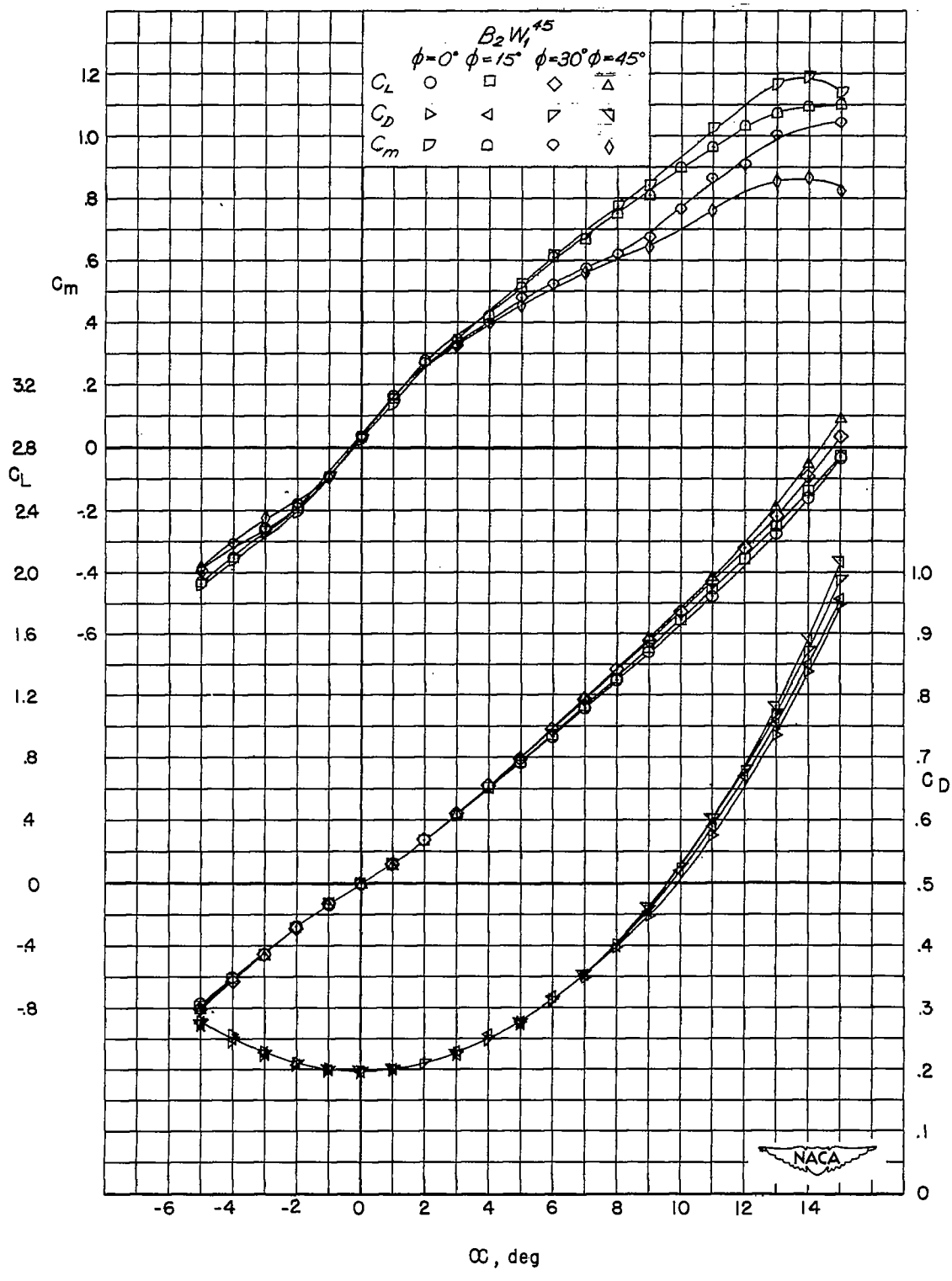

Figure 9.- Lift, drag, and pitching-moment characteristics of BW at M = 1.62.

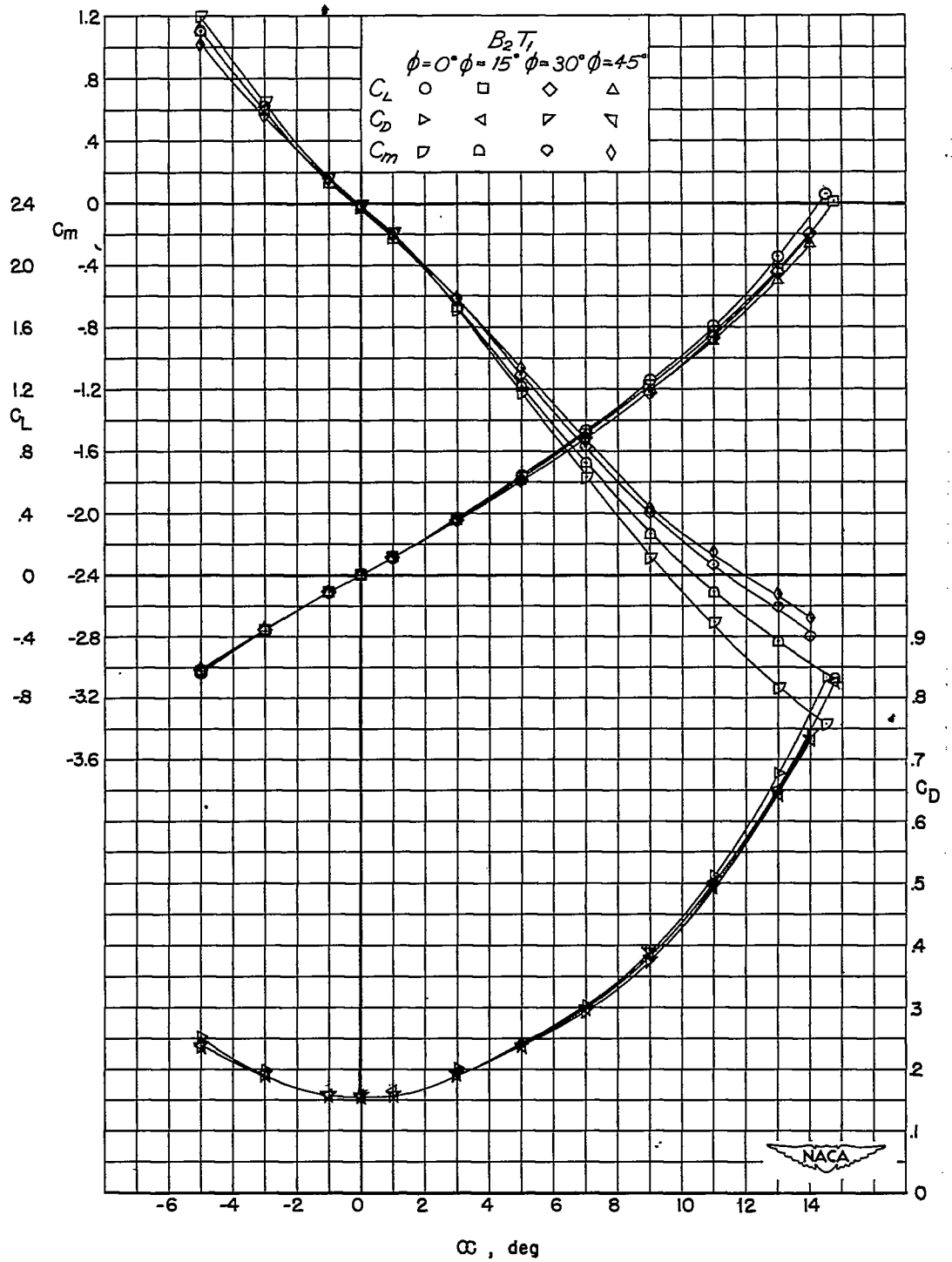

(a) B_2T_1.

Figure 10.- Lift, drag, and pitching-moment characteristics of BT at M = 1.62.

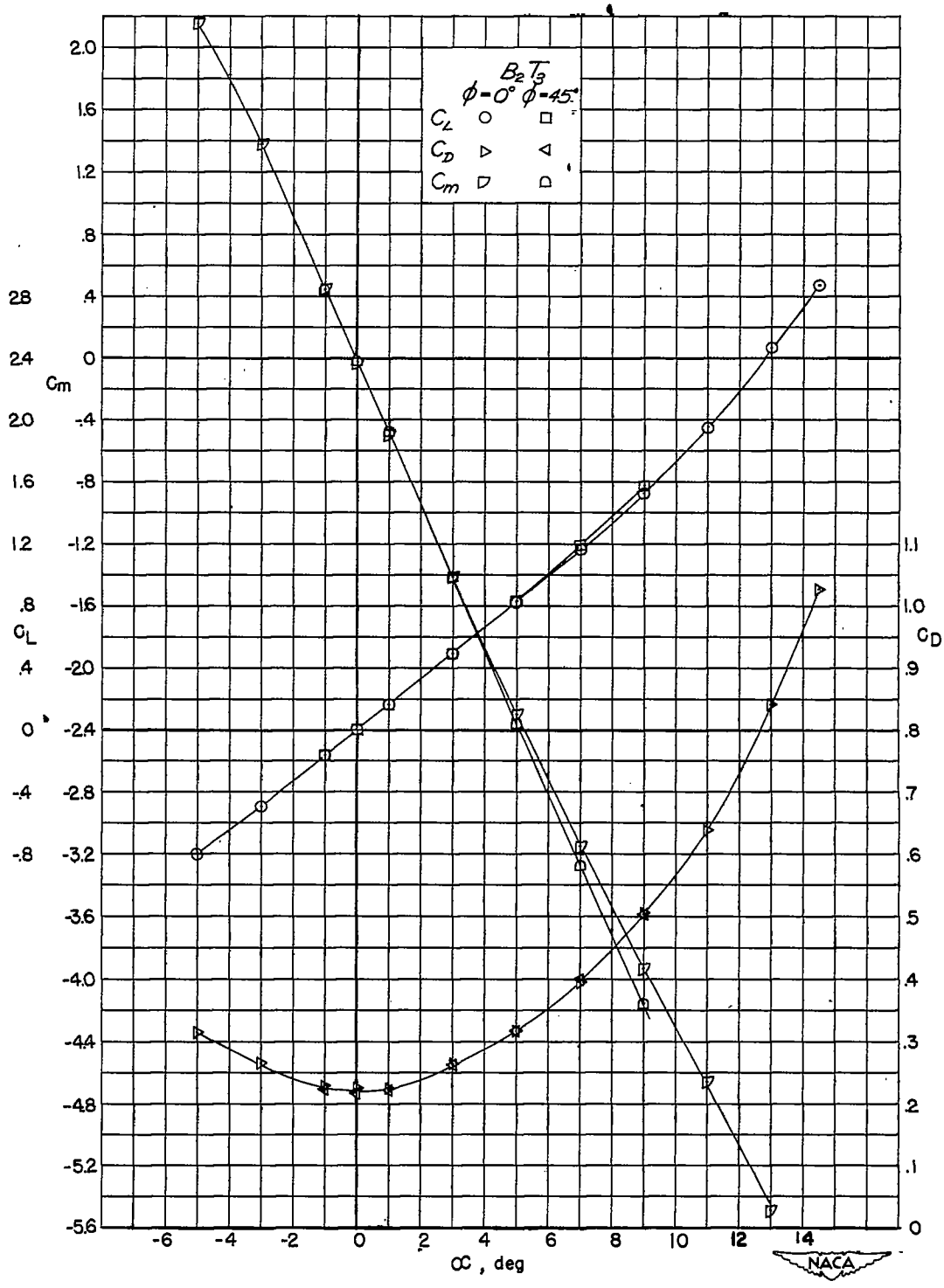

(b) B_2T_3.

Figure 10.- Concluded.

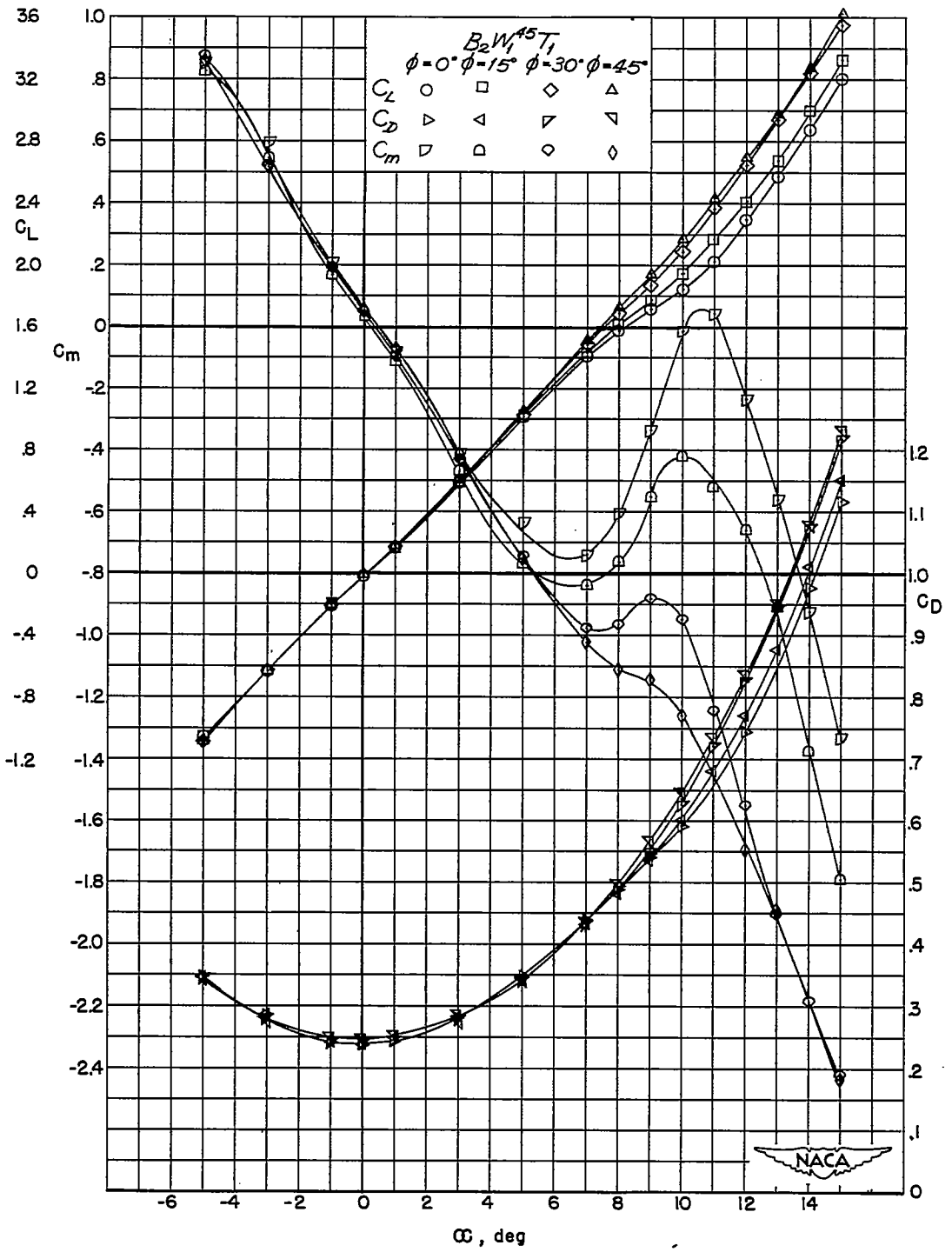

(a) $B_2W_1{}^{45}T_1$.

Figure 11.- Lift, drag, and pitching-moment characteristics of BWT at M = 1.62.

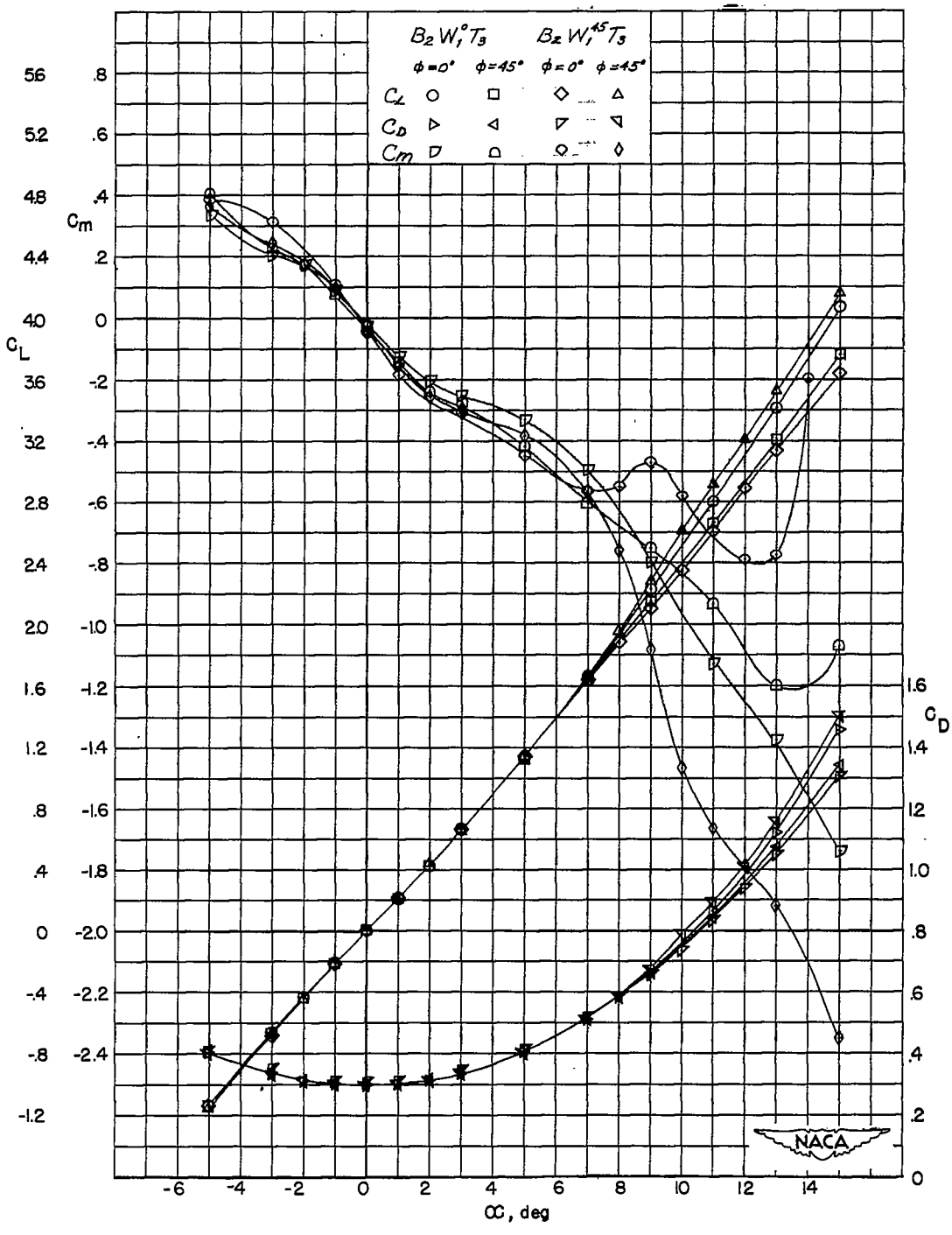

(b) $B_2W_1{}^{0}T_3$ and $B_2W_1{}^{45}T_3$.

Figure 11.- Continued.

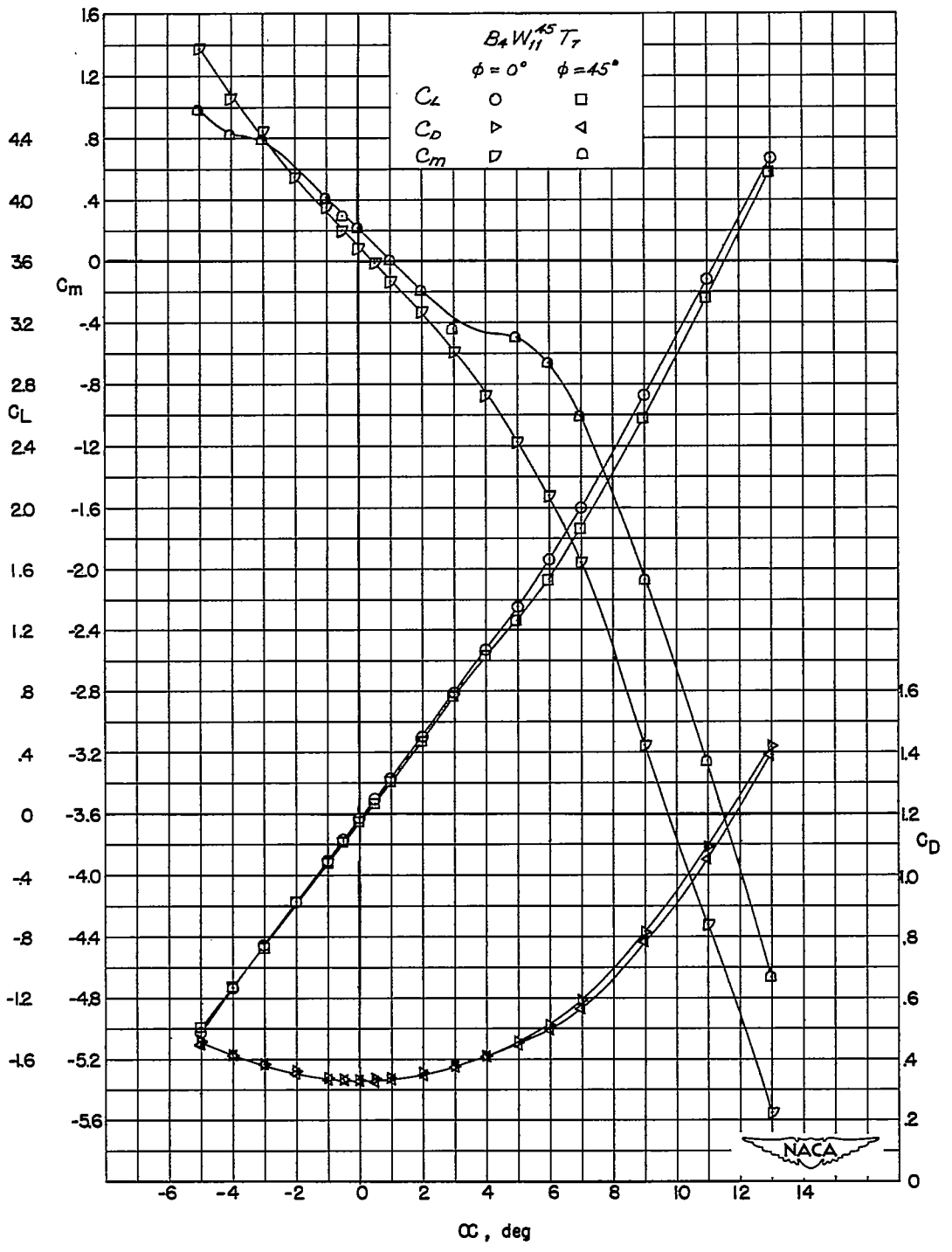

(c) $B_4W_{11}{}^{45}T_7$.

Figure 11.- Concluded.

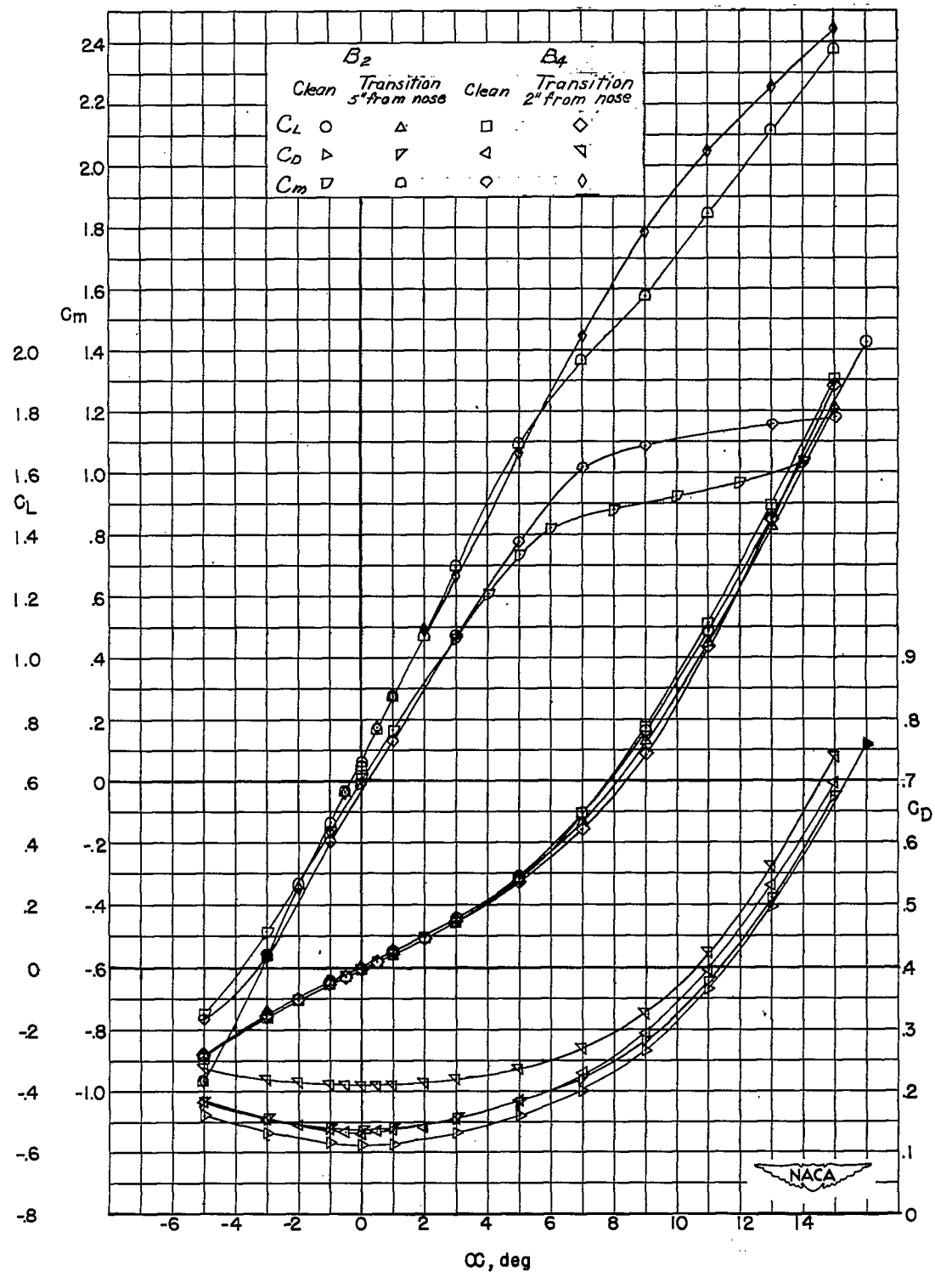

Figure 12.- Lift, drag, and pitching-moment characteristics of B at M = 2.40.

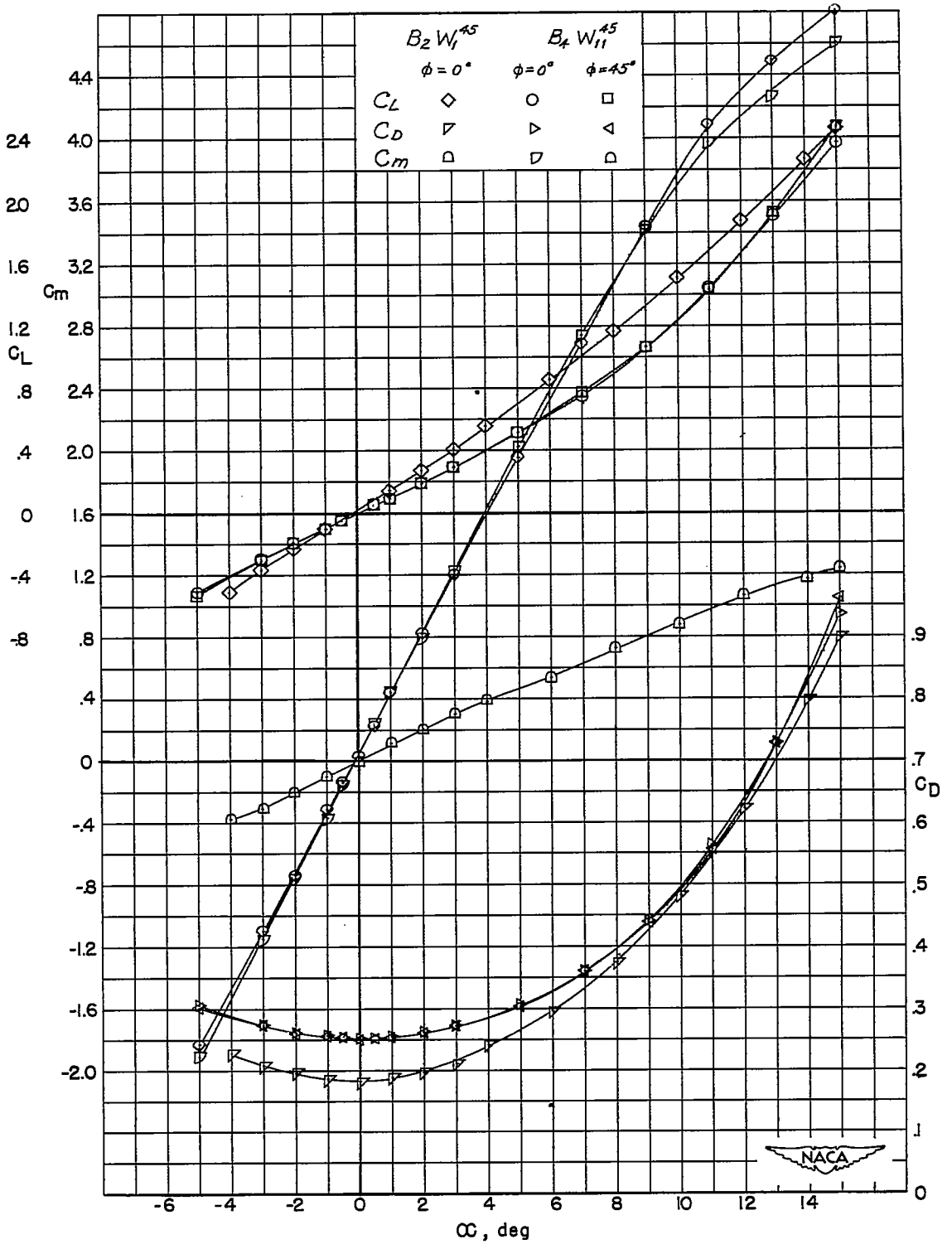

Figure 13.- Lift, drag, and pitching-moment characteristics of BW at M = 2.40.

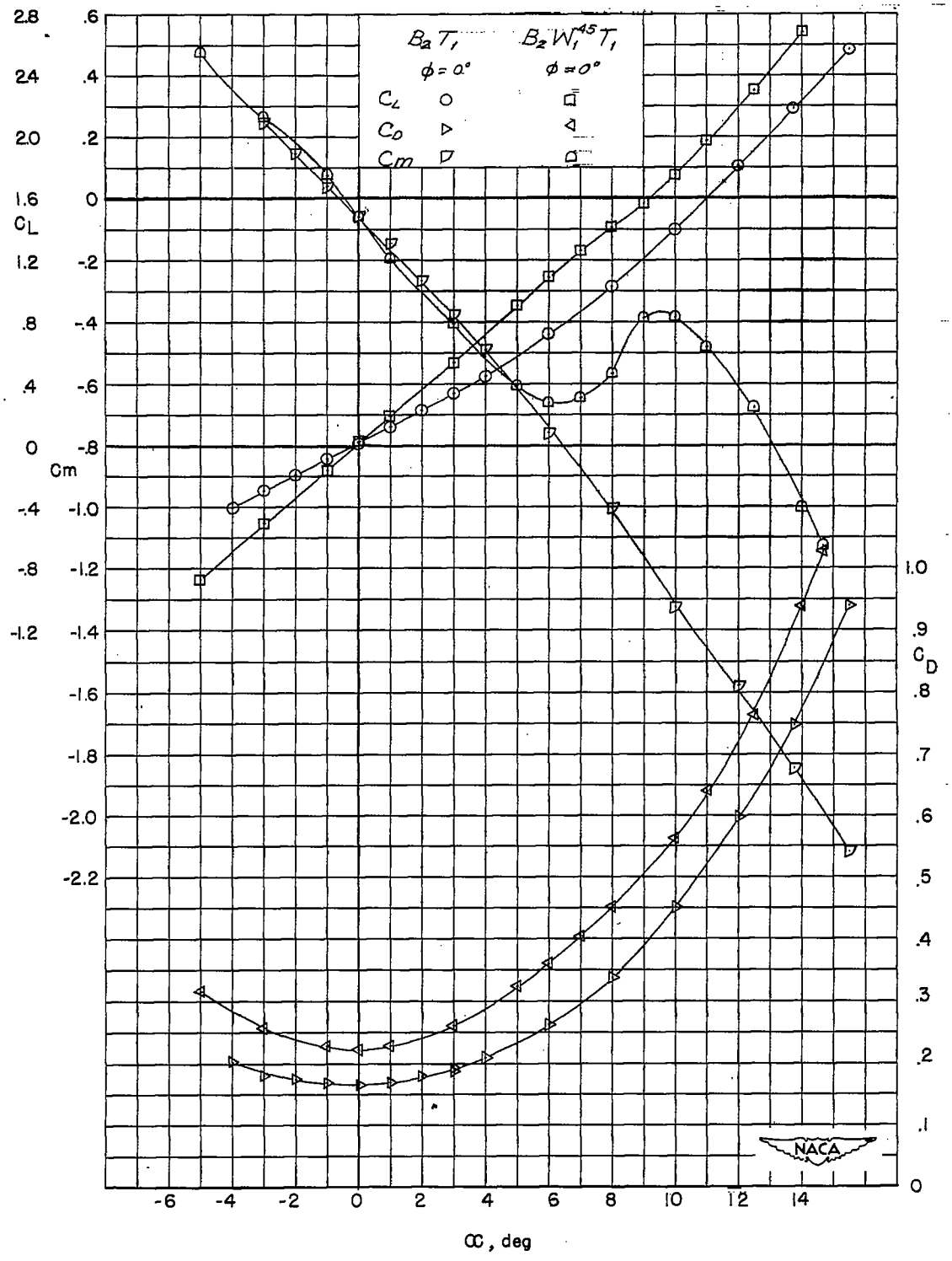

Figure 14.- Lift, drag, and pitching-moment characteristics of B_2T_1 and $B_2W_1^{45}T_1$ at M = 2.40.

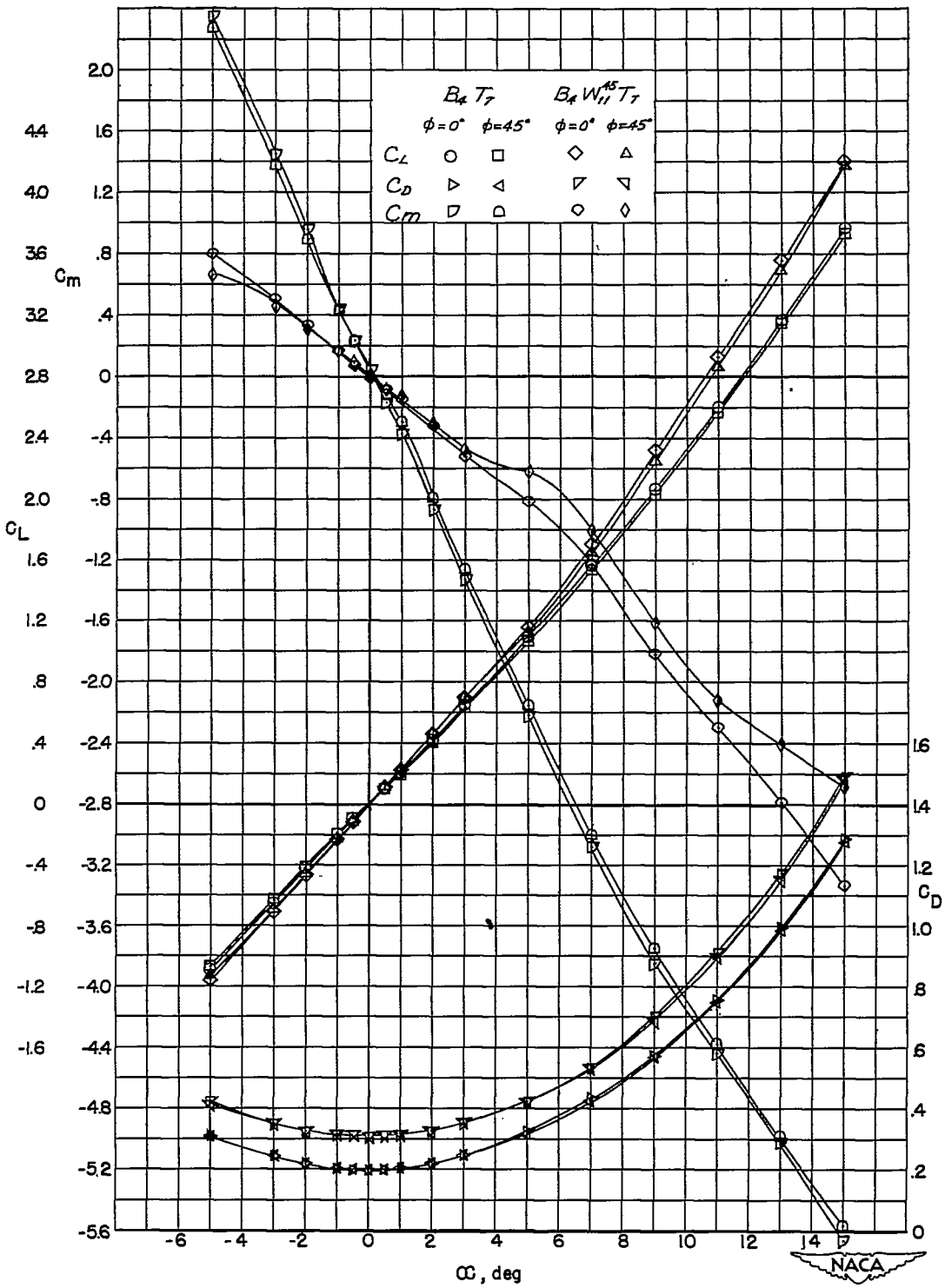

Figure 15.- Lift, drag, and pitching-moment characteristics of B_4T_7 and $B_4W_{11}^{45}T_7$ at M = 2.40.

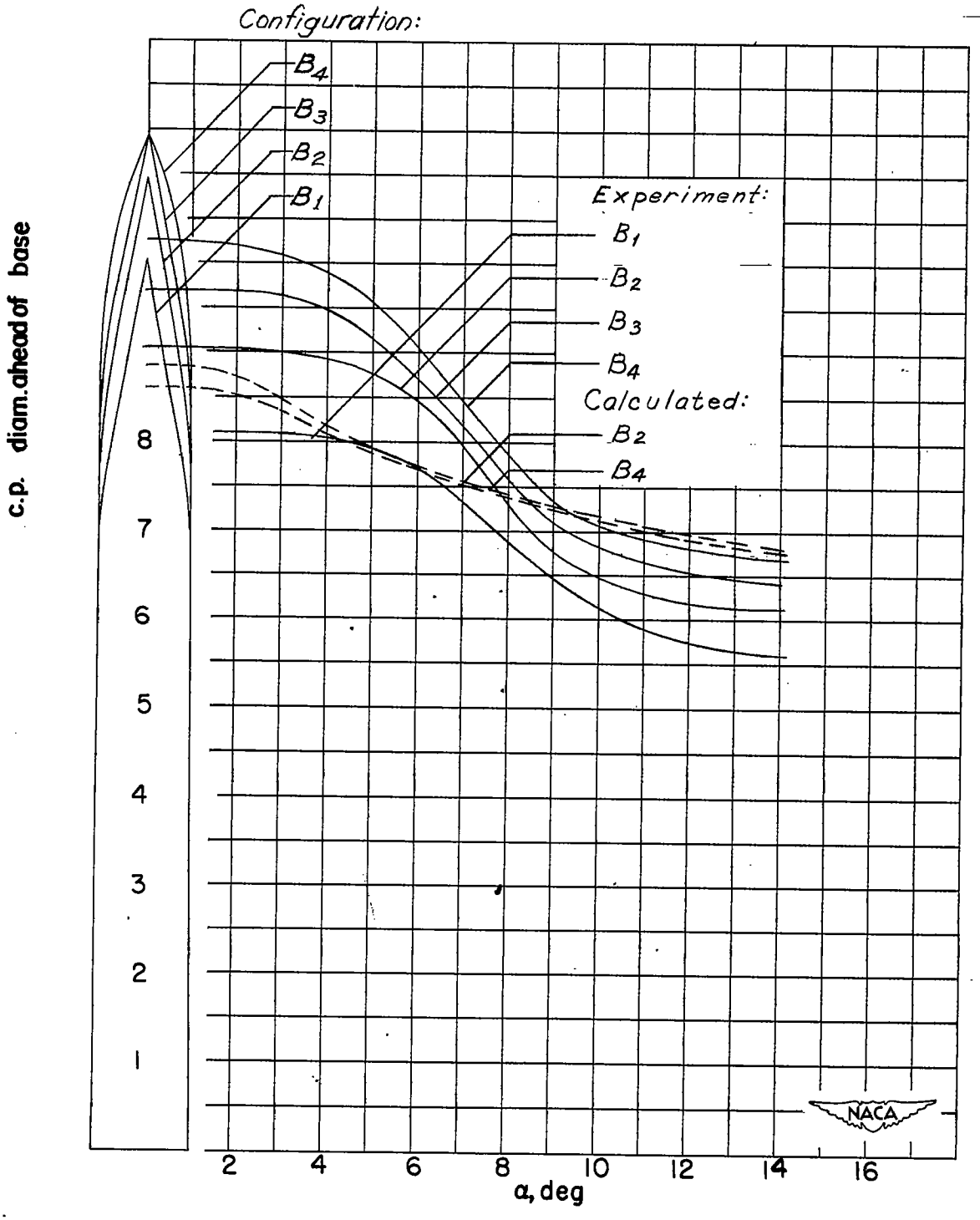

Figure 16.- Variation of center-of-pressure location with α of B_1, B_2, B_3, and B_4 at $M = 1.93$.

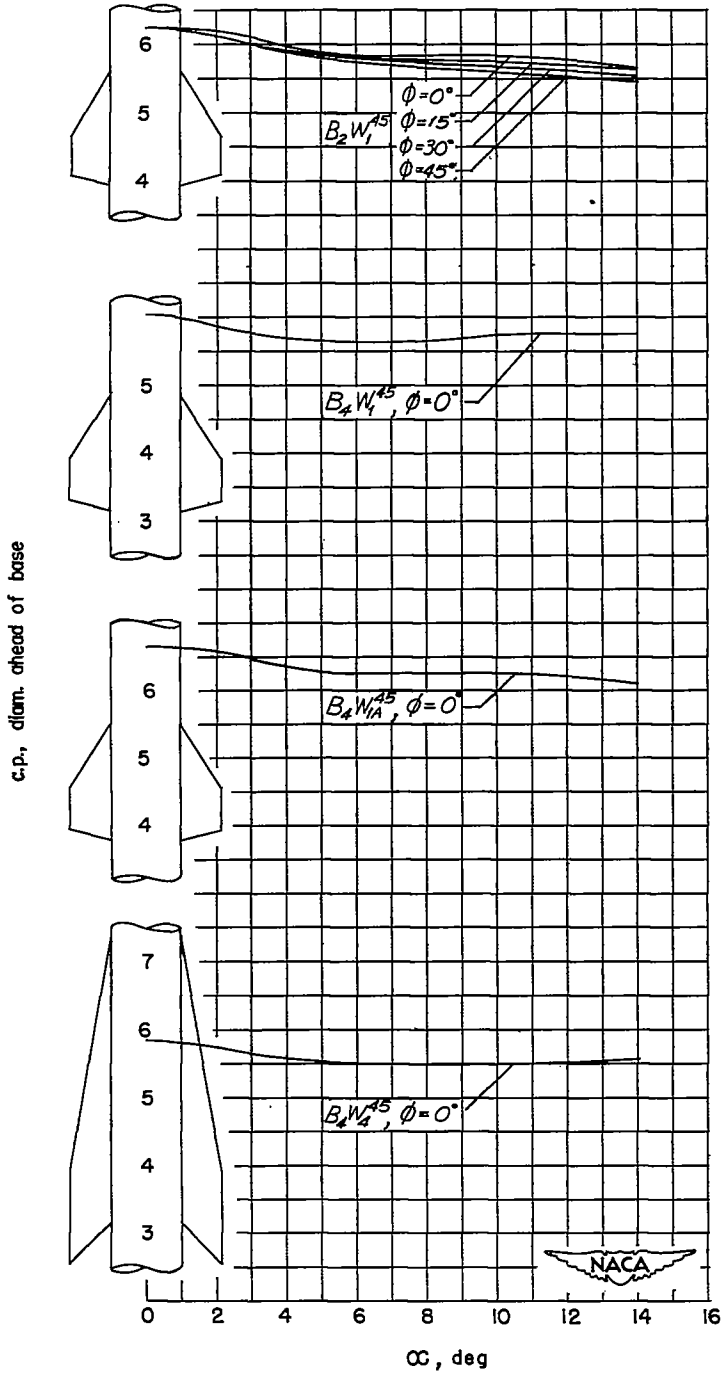

(a) $B_2W_1{}^{45}$, $B_4W_1{}^{45}$, $B_4W_{1A}{}^{45}$, and $B_4W_4{}^{45}$.

Figure 17.- Variation of center-of-pressure location with α of BW at $M = 1.93$.

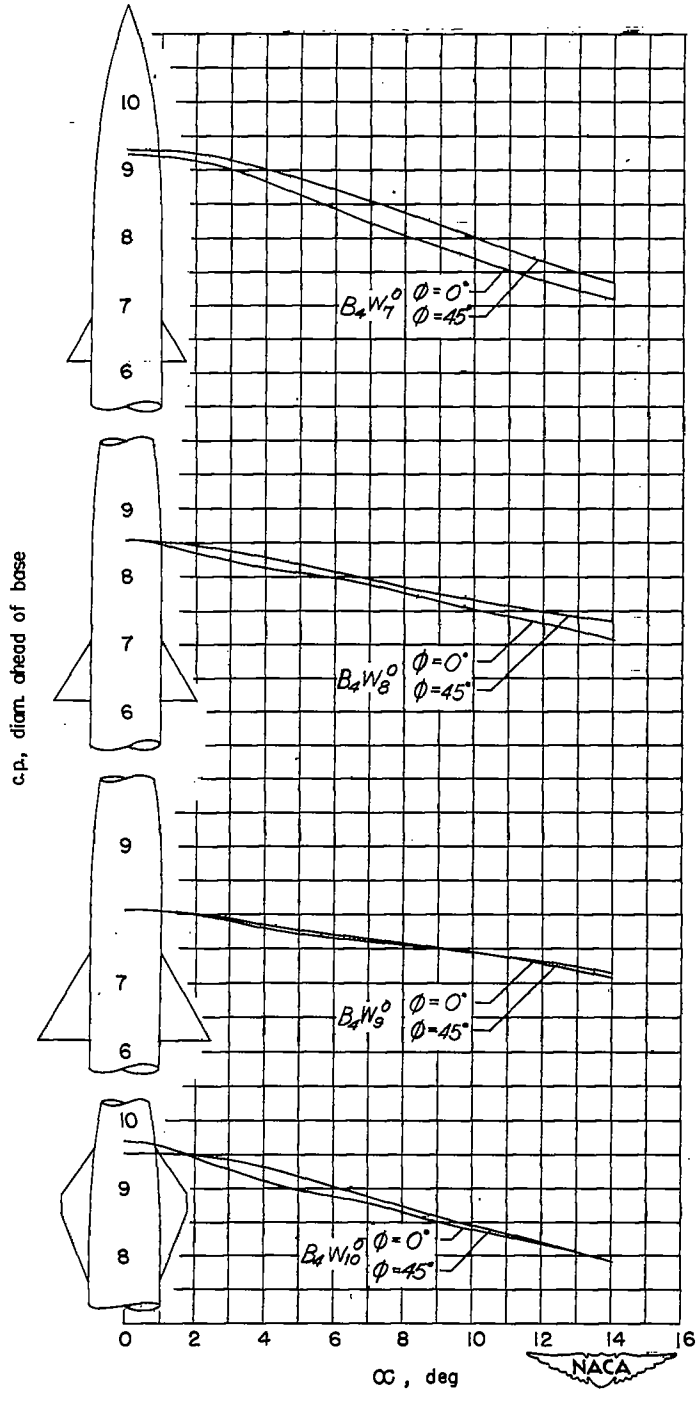

(b) $B_4W_7^0$, $B_4W_8^0$, $B_4W_9^0$, and $B_4W_{10}^0$.

Figure 17.- Continued.

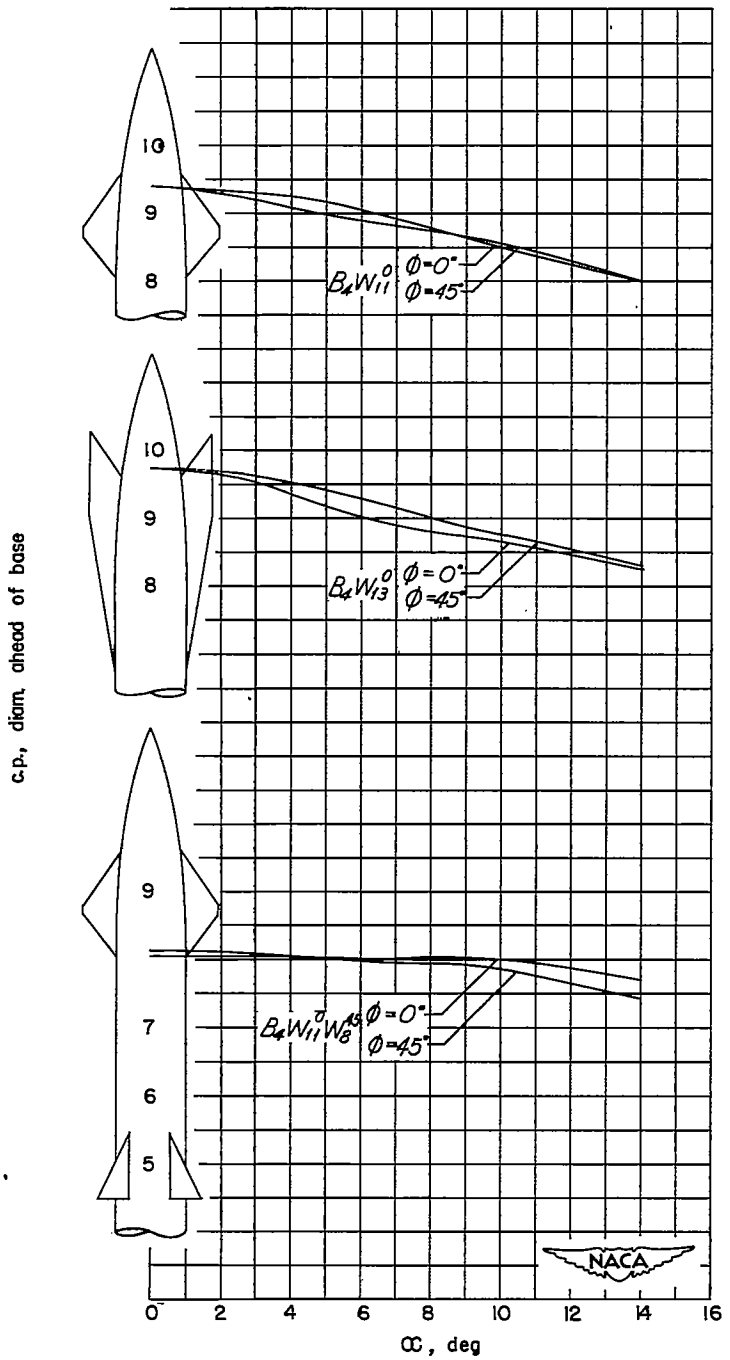

(c) $B_4W_{11}{}^0$, $B_4W_{13}{}^0$, and $B_4W_{11}{}^0W_8{}^{45}$.

Figure 17.- Concluded.

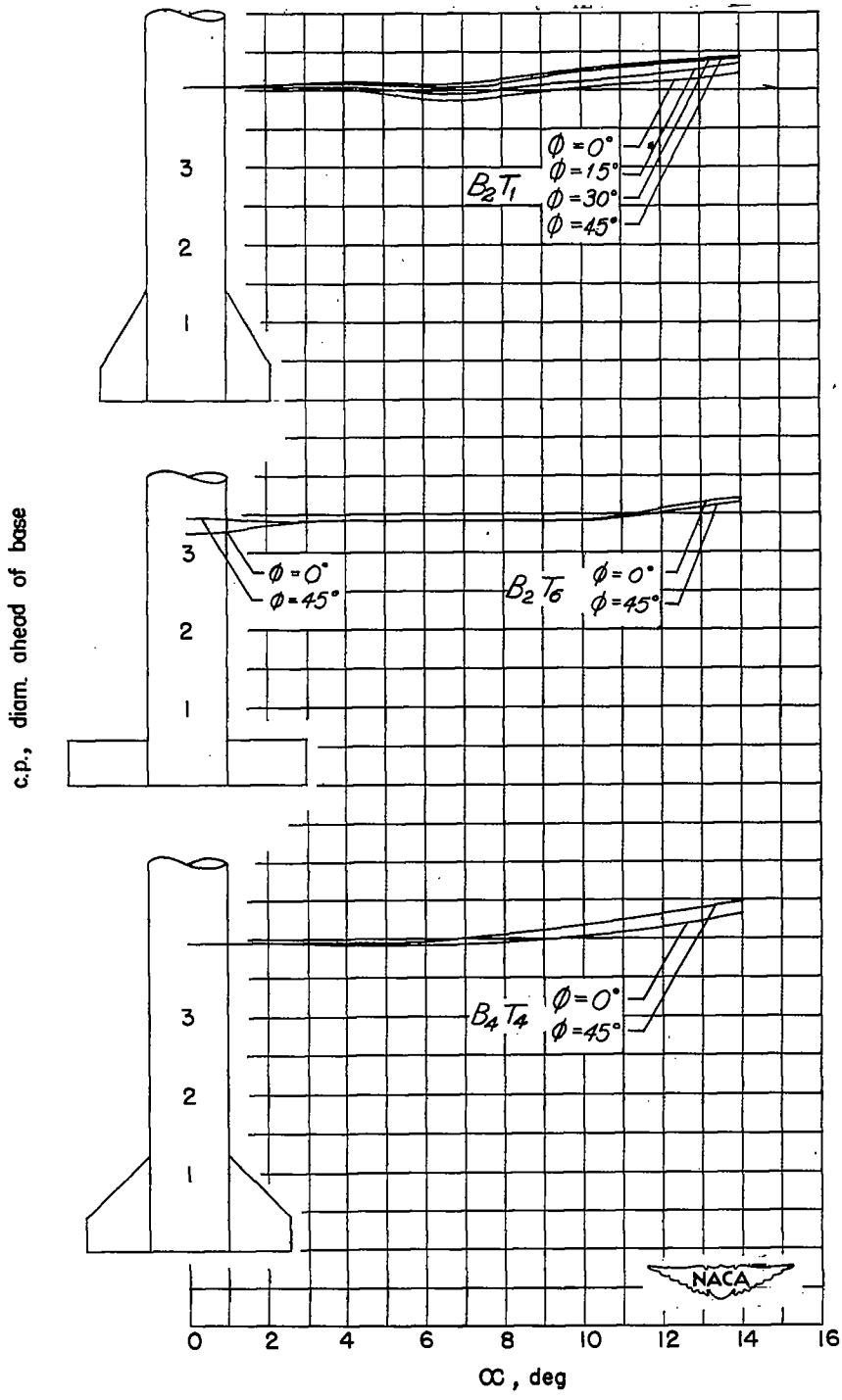

(a) B_2T_1, B_2T_6, and B_4T_4.

Figure 18.- Variation of center-of-pressure location with α of BT at M = 1.93.

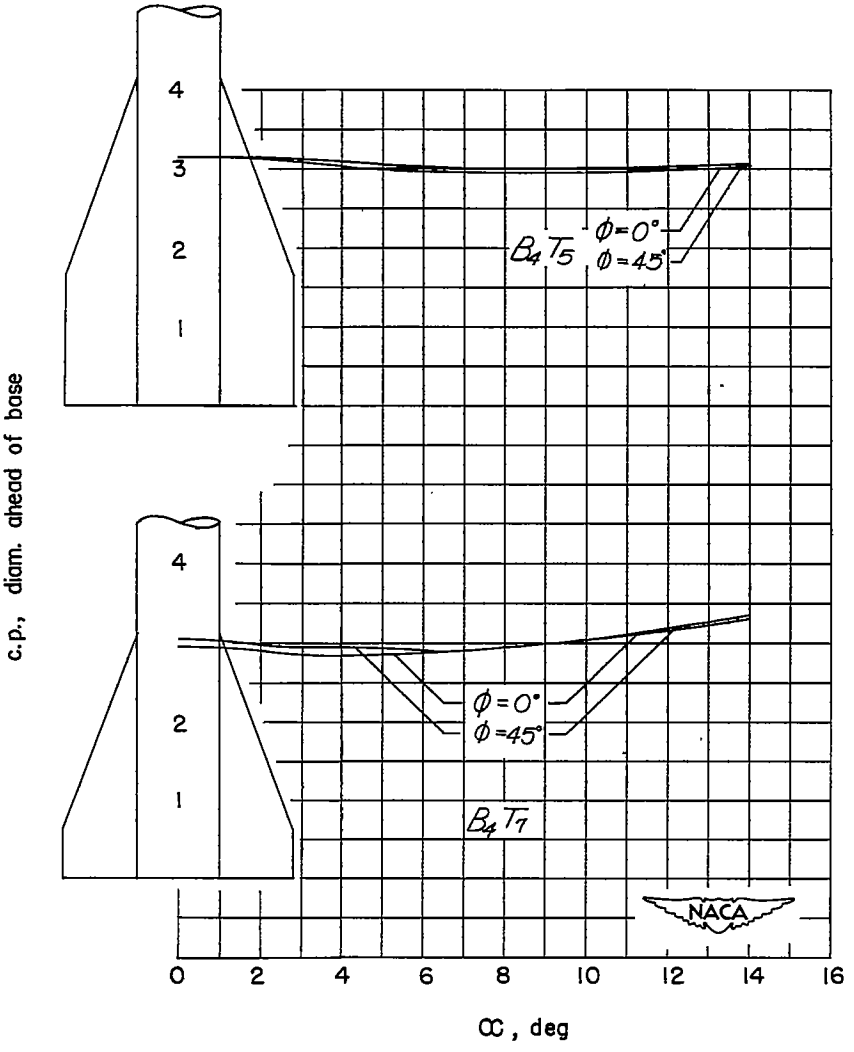

(b) B_4T_5 and B_4T_7.

Figure 18.- Concluded.

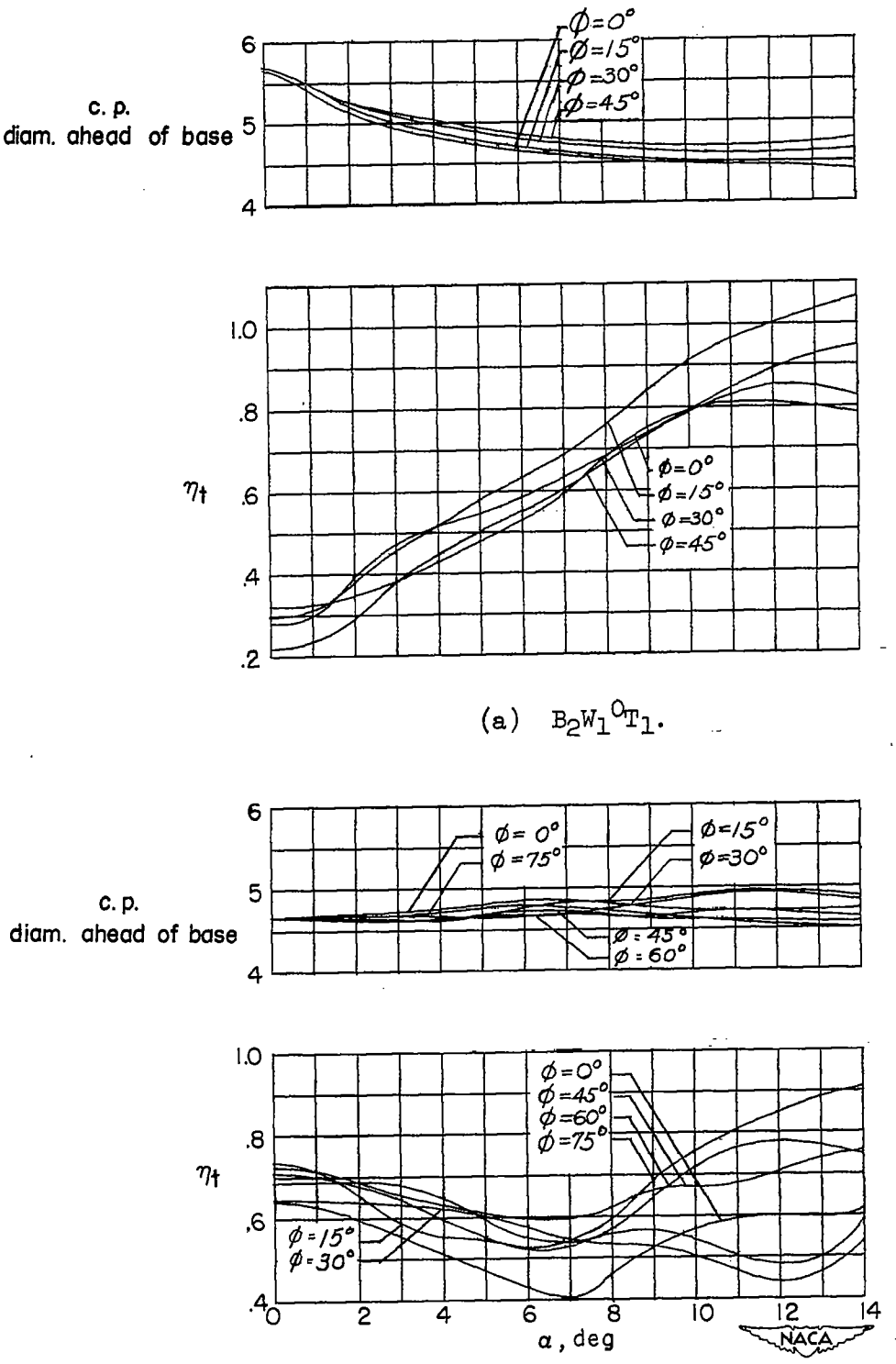

Figure 19.- Variation of center-of-pressure location and η_t with α of BWT at M = 1.93.

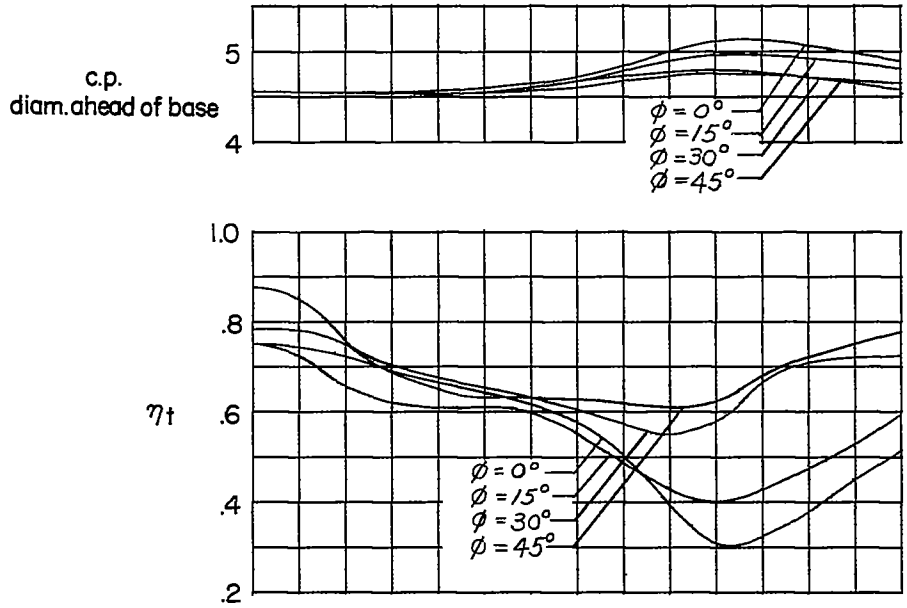

(c) $B_2W_1{}^{45}T_1$.

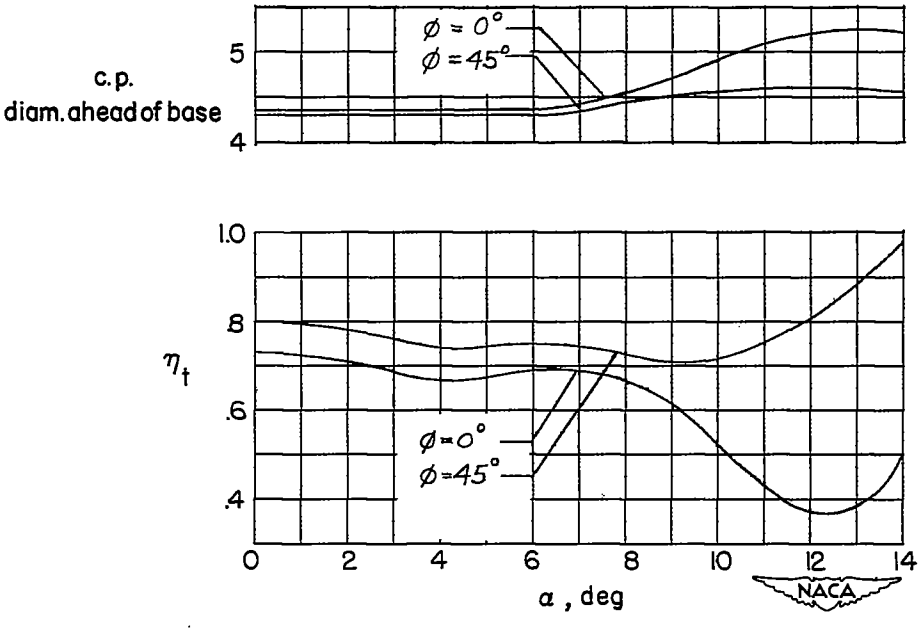

(d) $B_4W_1{}^{45}T_1$.

Figure 19.- Continued.

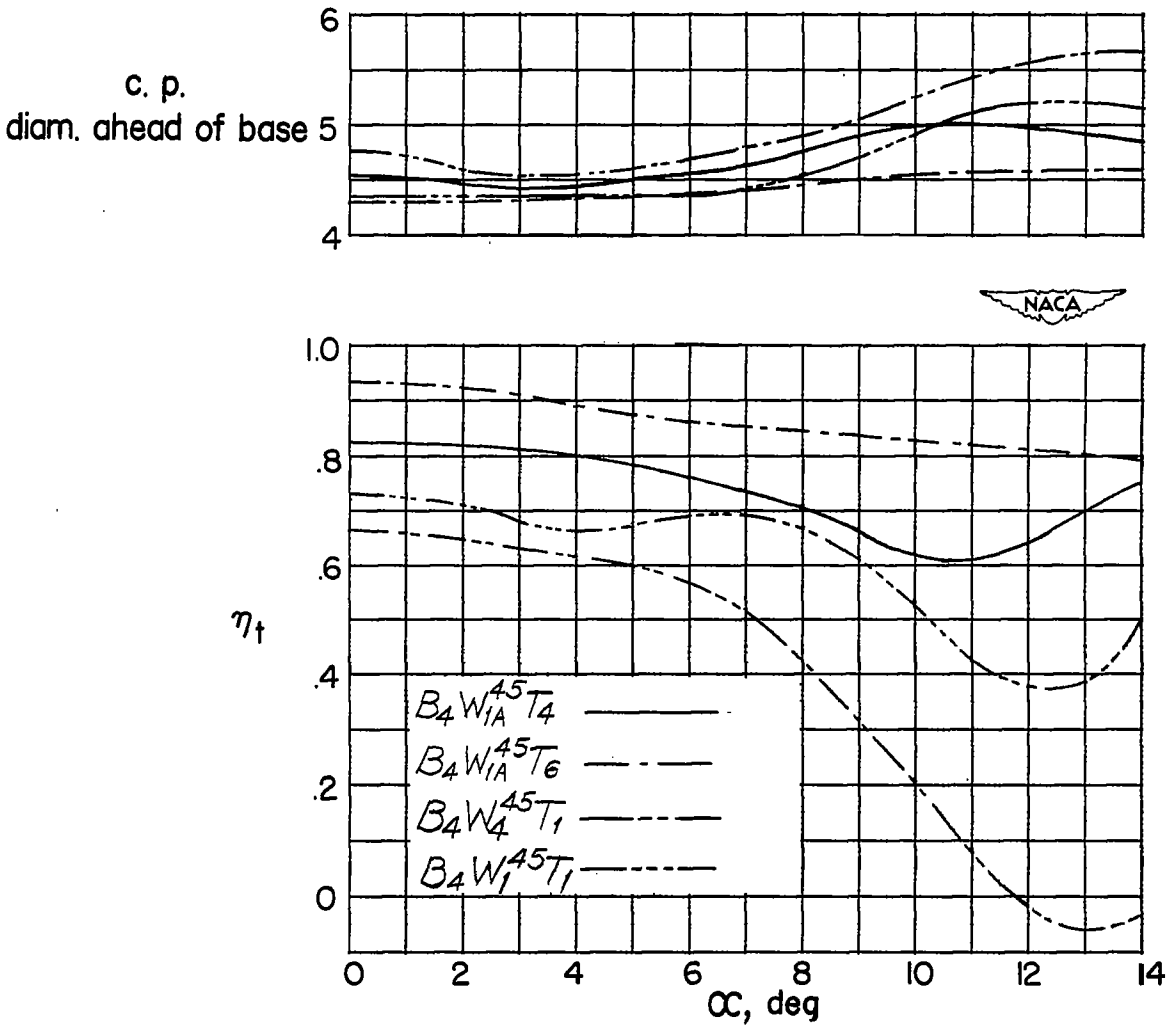

(e) $B_4W_1{}^{45}T_1$, $B_4W_{1A}{}^{45}T_4$, $B_4W_{1A}{}^{45}T_6$, and $B_4W_4{}^{45}T_1$ at zero roll angle.

Figure 19.- Continued.

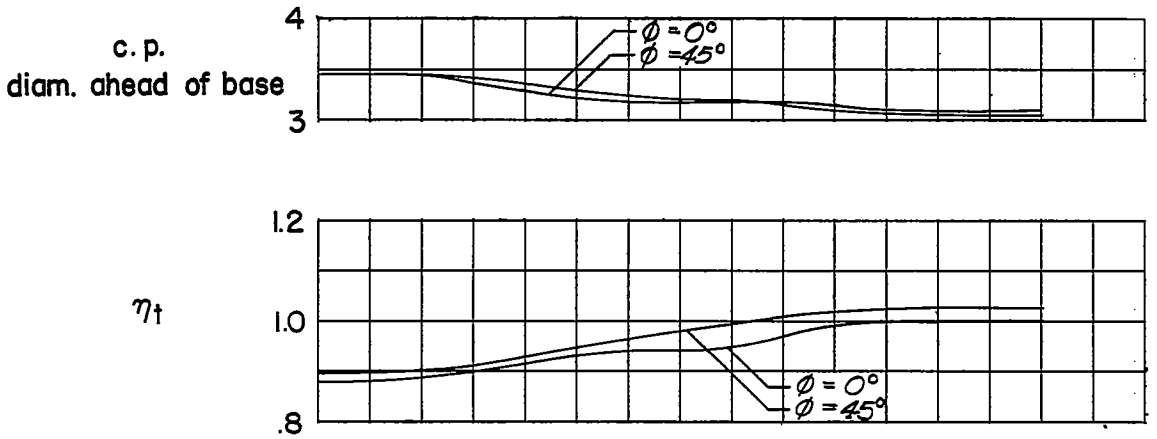

(f) $B_4W_7{}^0T_5$.

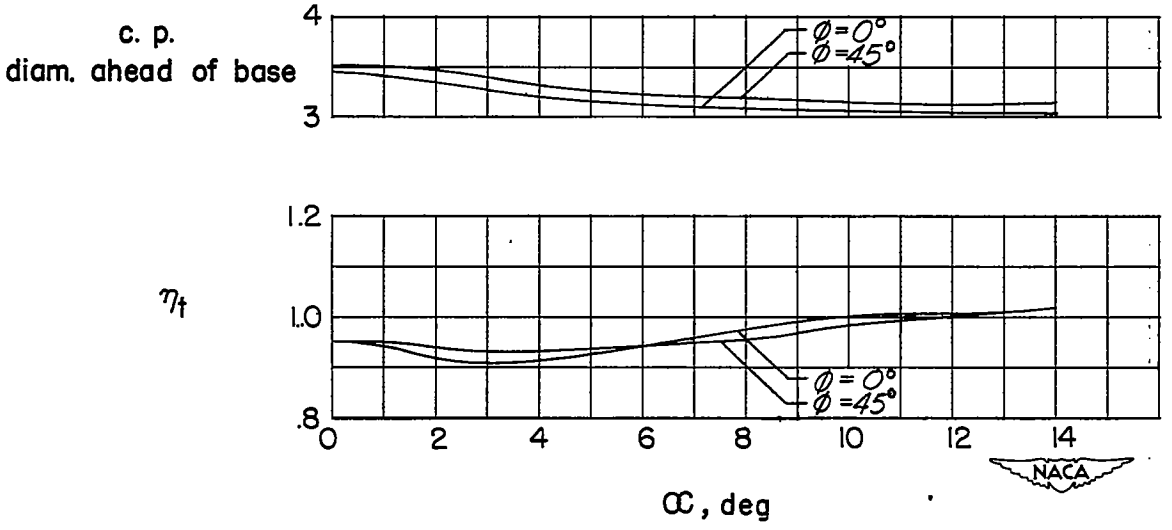

(g) $B_4W_7{}^{45}T_5$.

Figure 19.- Continued.

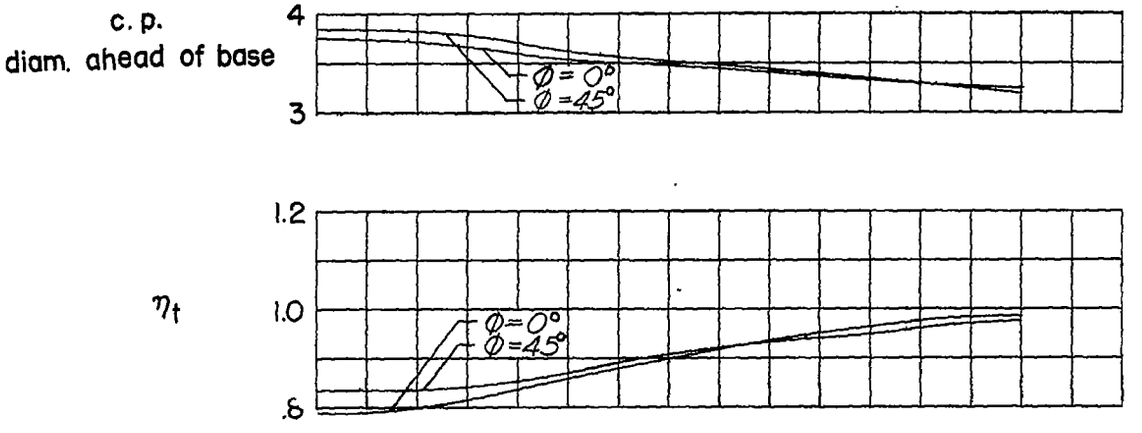

(h) $B_4W_8{}^0T_5$.

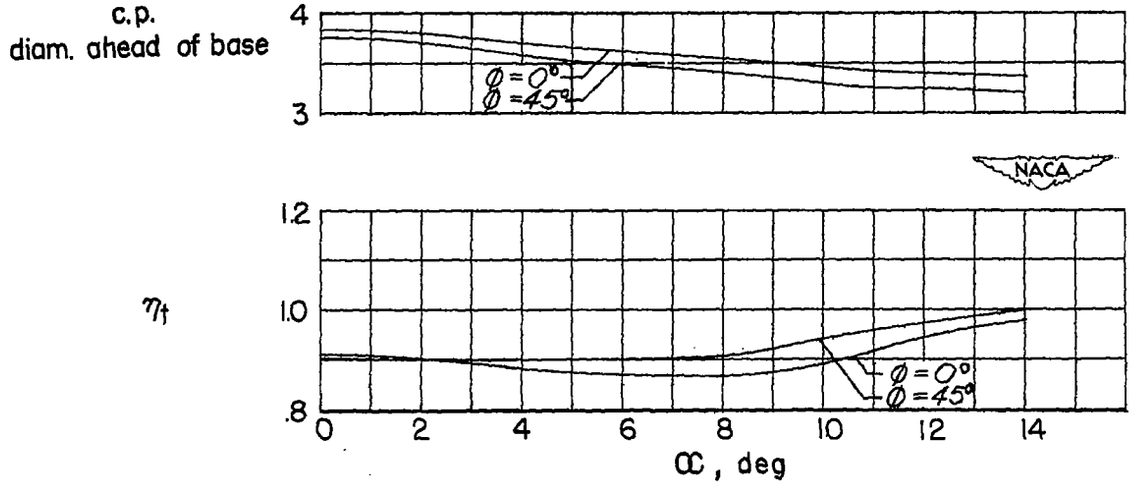

(i) $B_4W_8{}^{45}T_5$.

Figure 19.- Continued.

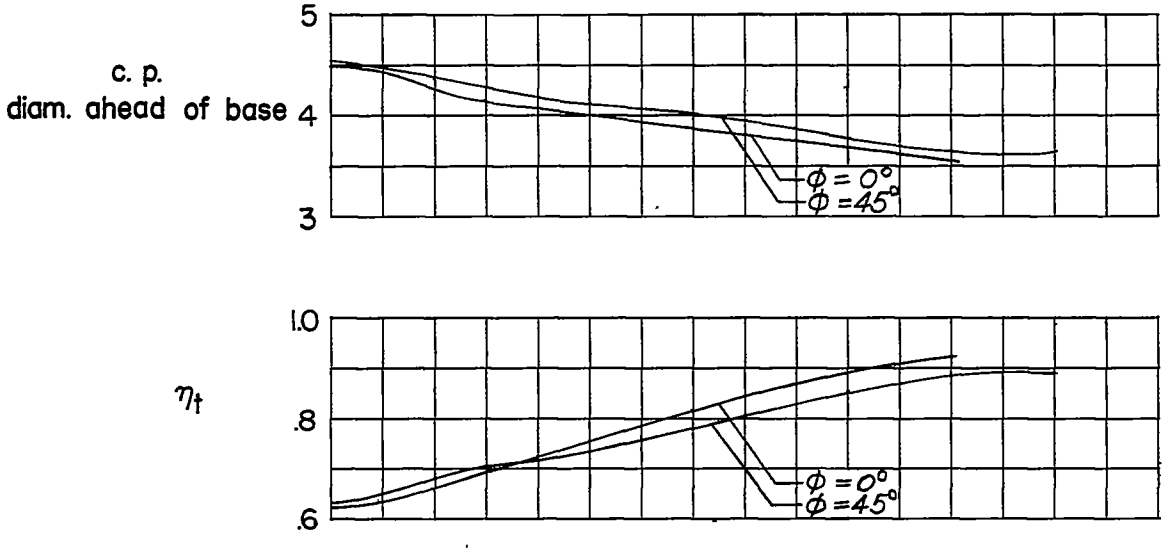

(j) $B_4W_9{}^0T_5$.

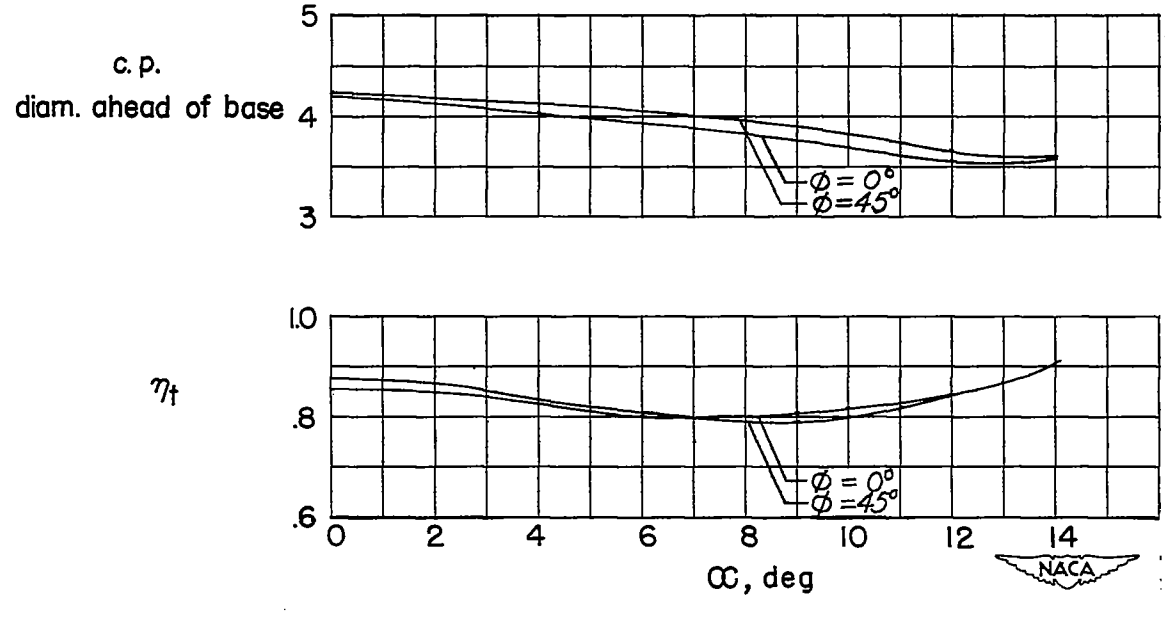

(k) $B_4W_9{}^{45}T_5$.

Figure 19.- Continued.

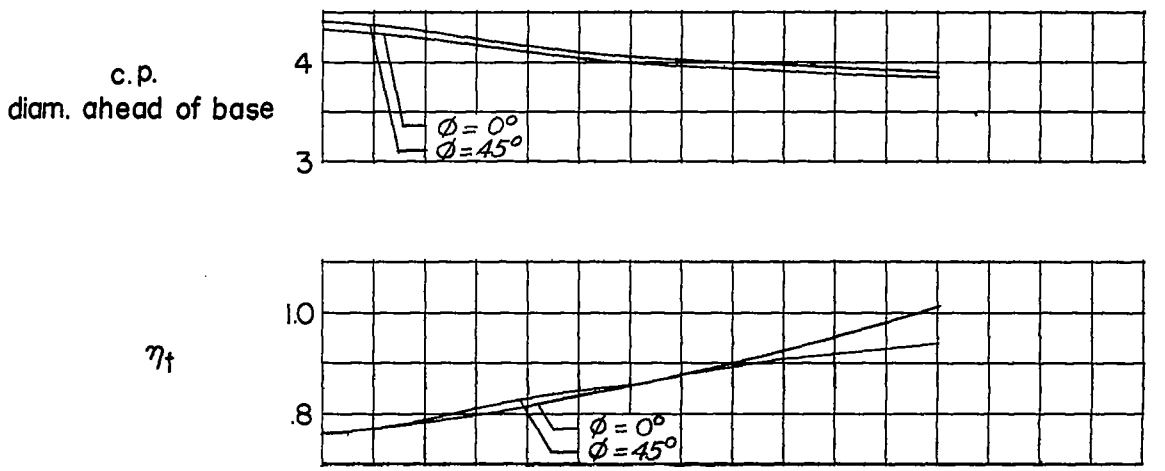

(l) $B_4W_{10}{}^0T_5$.

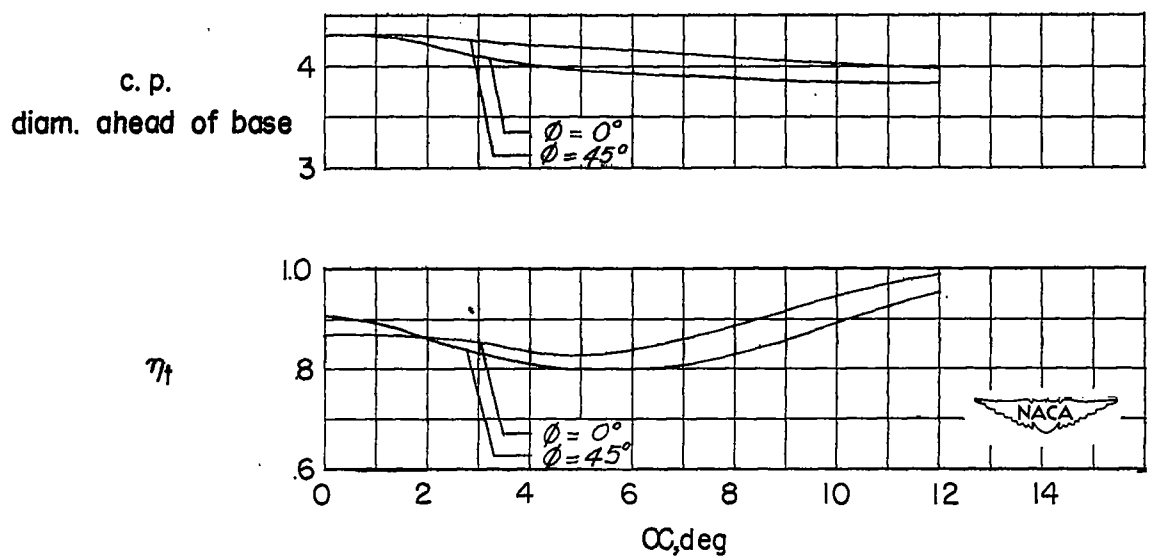

(m) $B_4W_{10}{}^{45}T_5$.

Figure 19.- Continued.

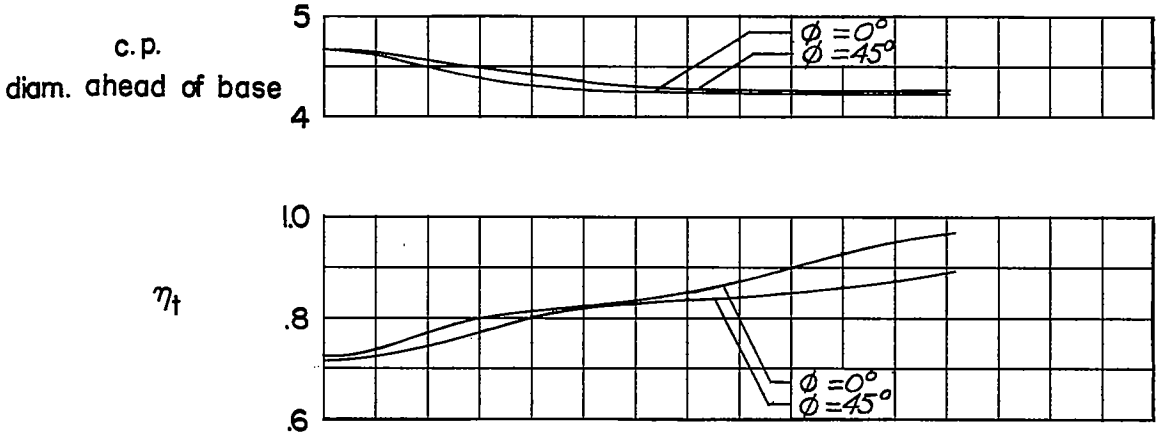

(n) $B_4W_{13}{}^{0}T_5$.

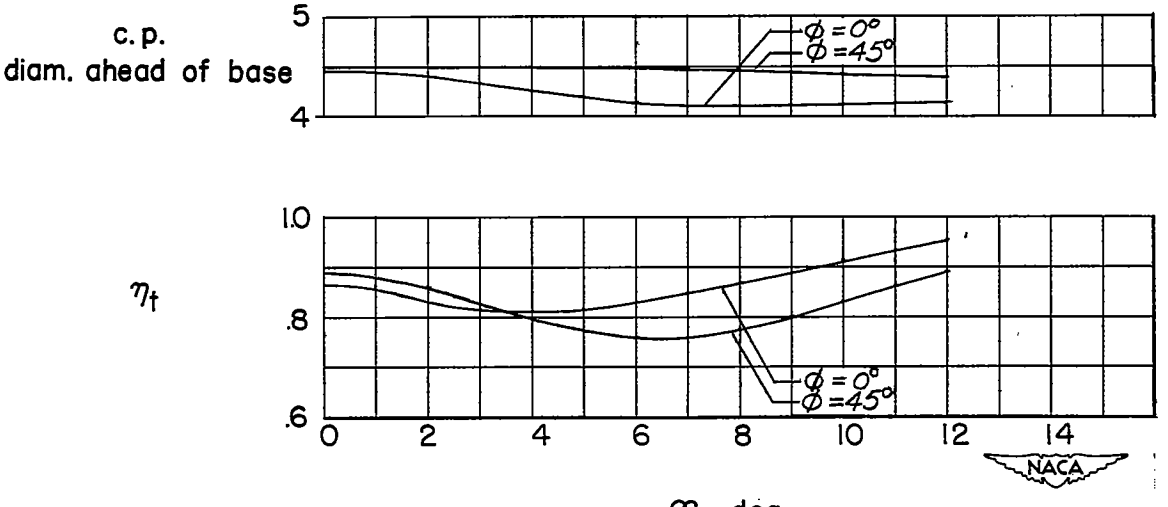

(o) $B_4W_{13}{}^{45}T_5$.

Figure 19.- Continued.

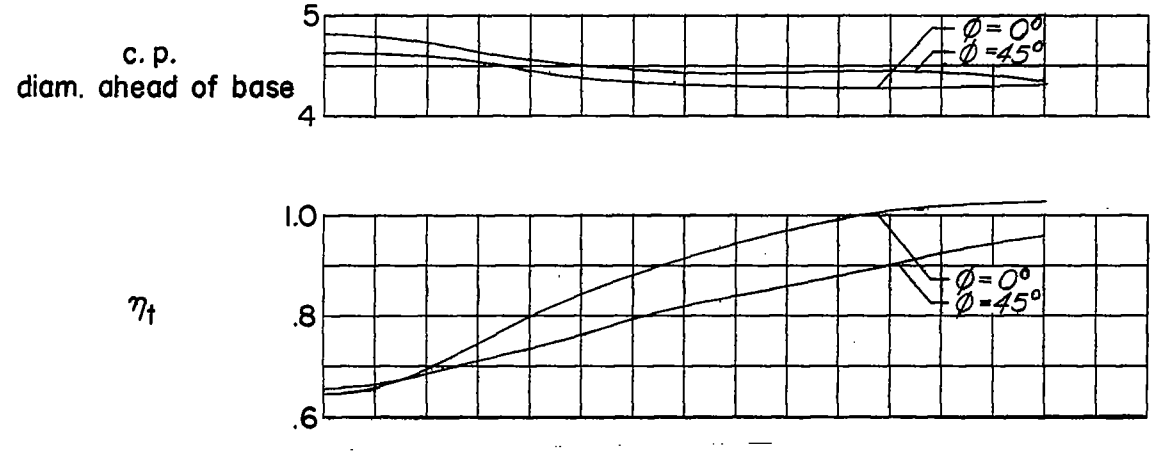

(p) $B_4W_{11}{}^0T_7$.

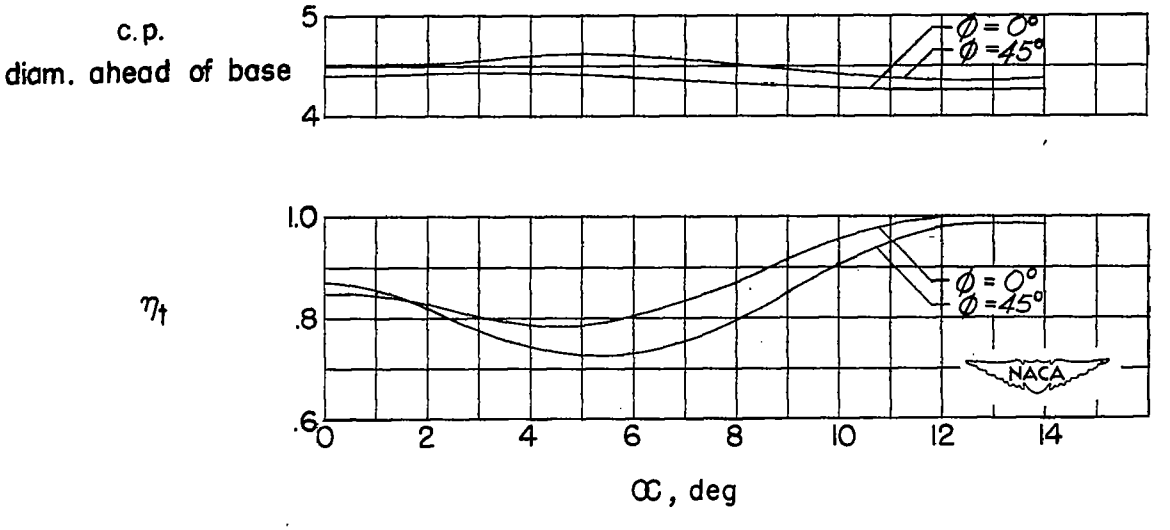

(q) $B_4W_{11}{}^{45}T_7$.

Figure 19.- Continued.

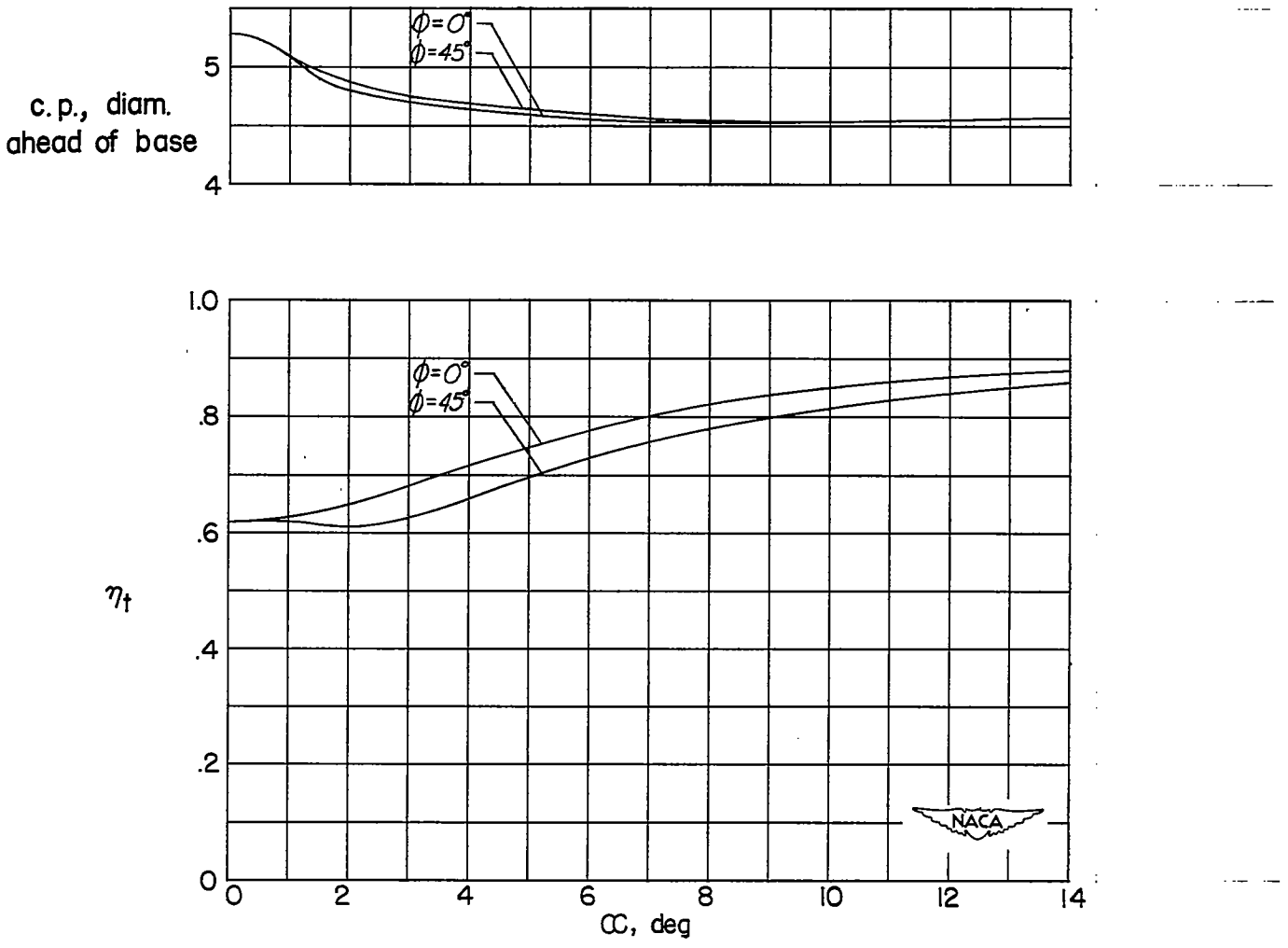

(r) $B_4W_{11}{}^0W_8{}^{45}T_7$.

Figure 19.- Concluded.

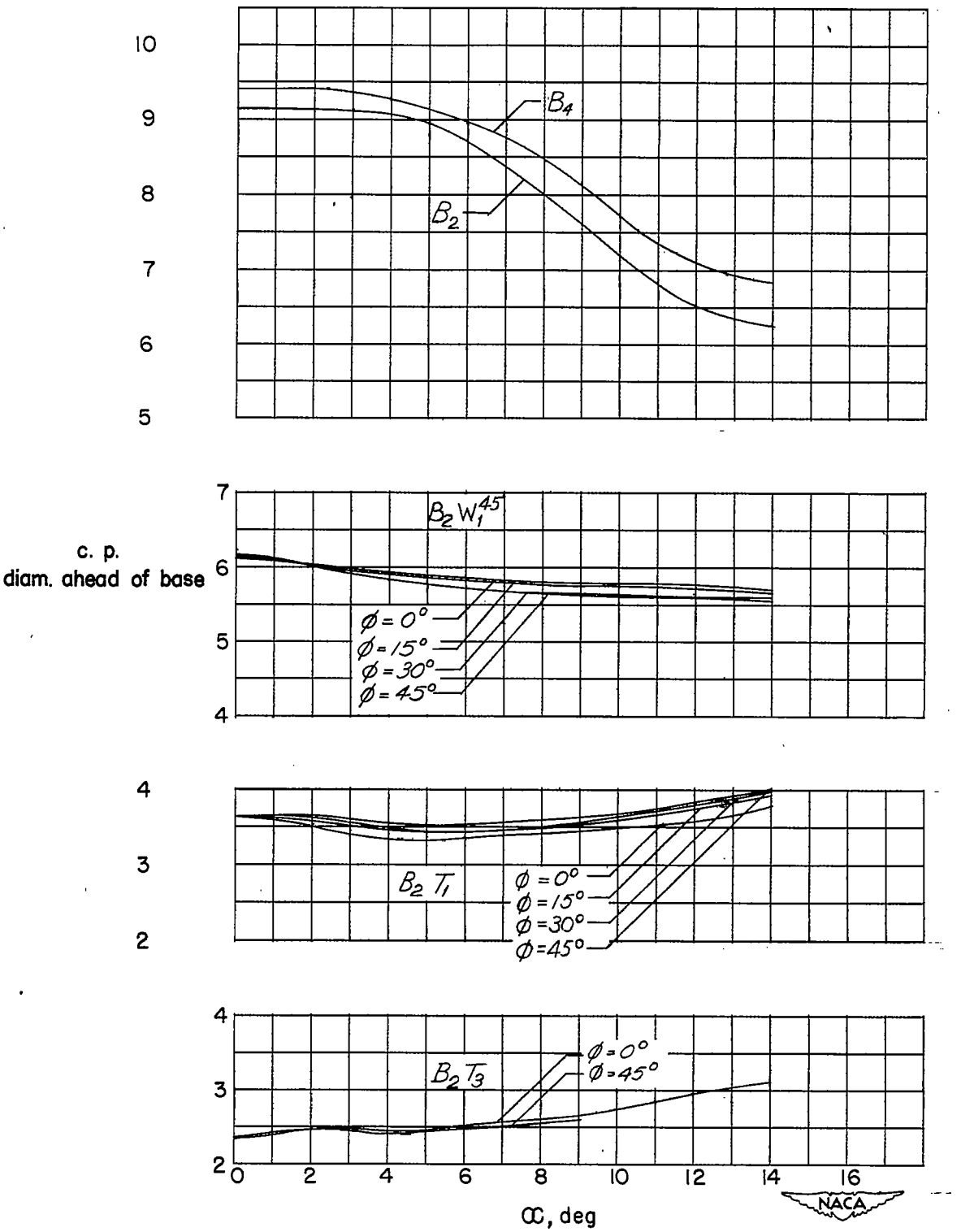

Figure 20.- Variation of center-of-pressure location with α of B, BW, and BT at M = 1.62.

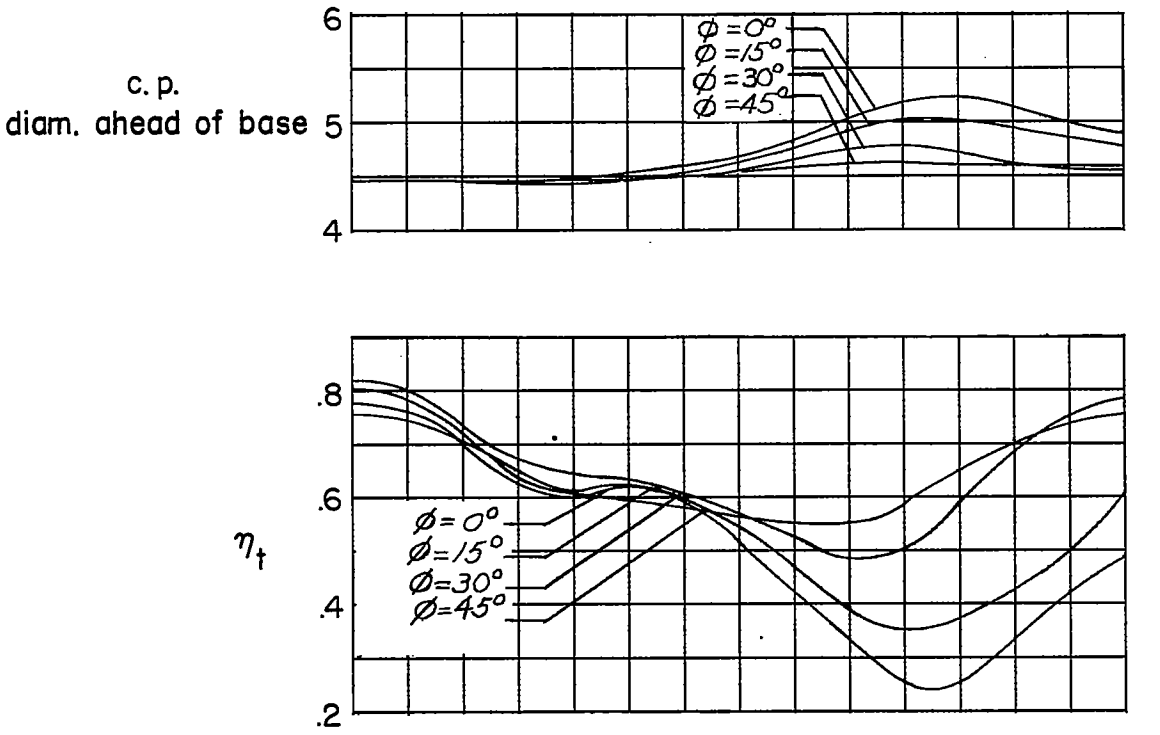

(a) $B_2W_1{}^{45}T_1$.

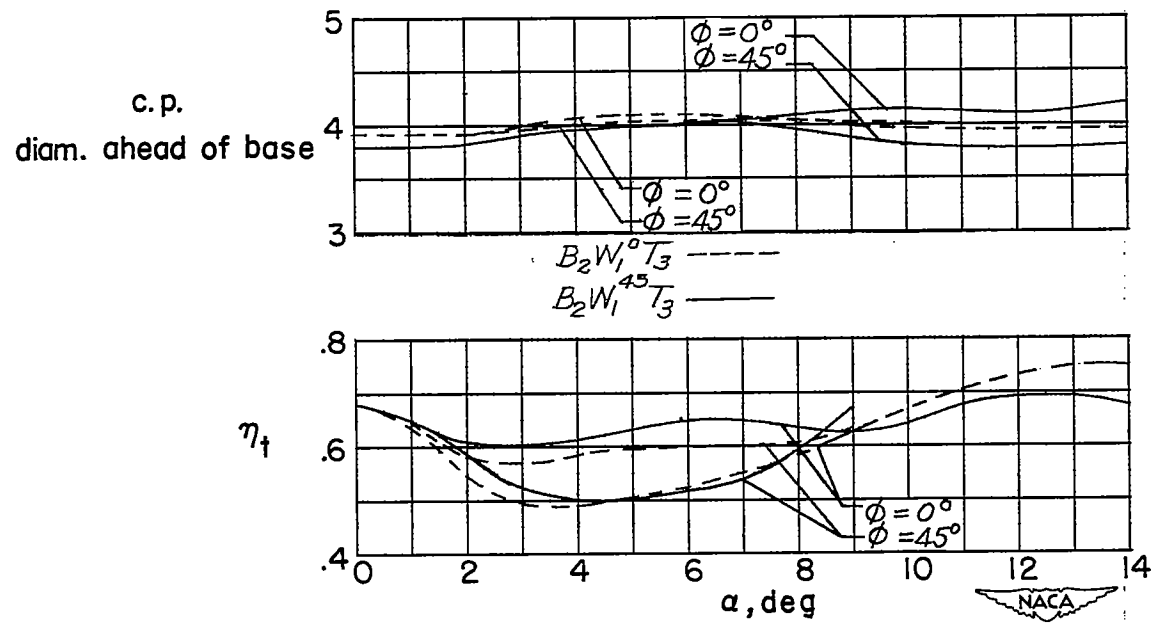

(b) $B_2W_1{}^{0}T_3$ and $B_2W_1{}^{45}T_3$.

Figure 21.- Variation of center-of-pressure location and η_t with α of BWT at M = 1.62.

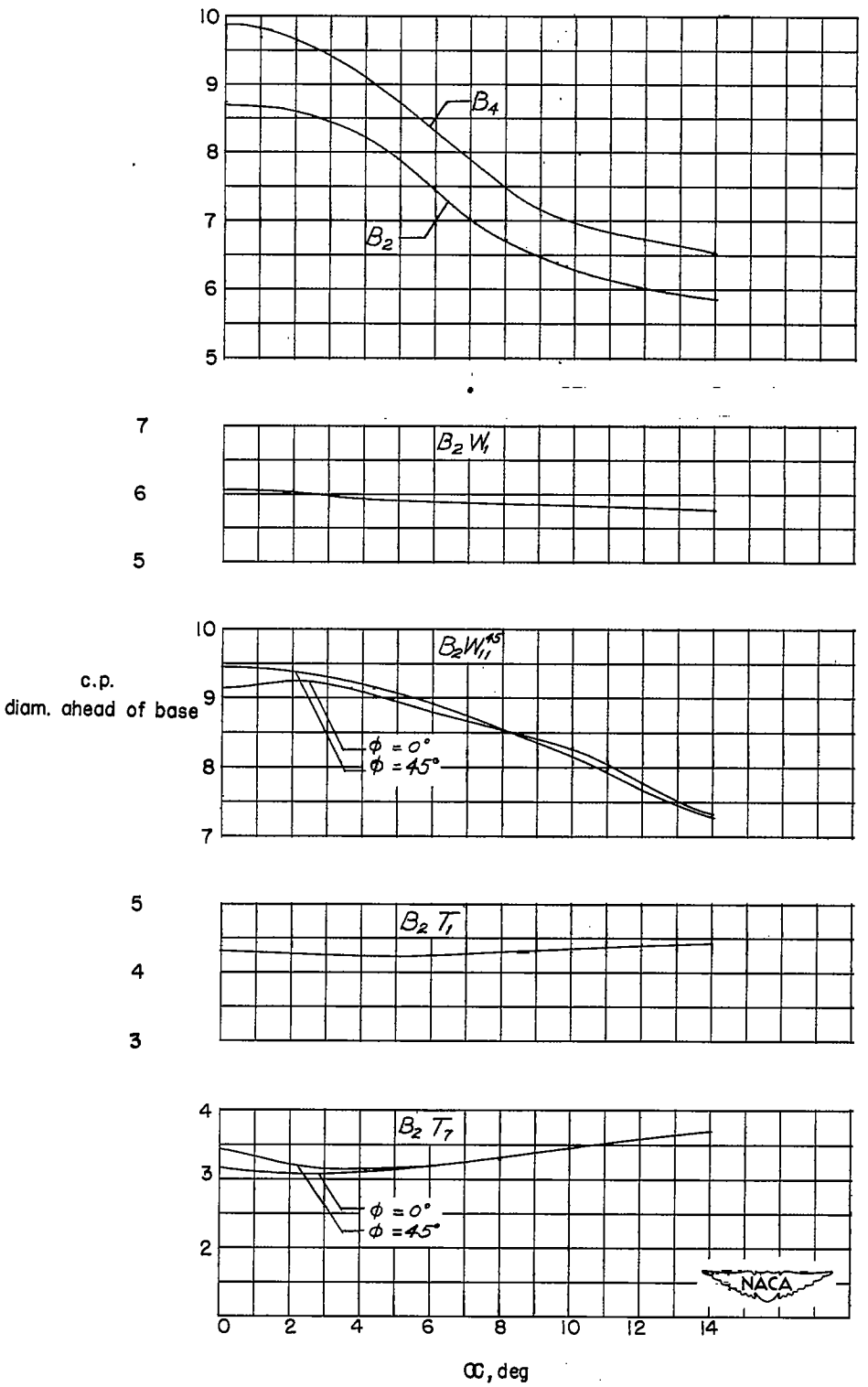

Figure 22.- Variation of center-of-pressure location with α of B, BW, and BT at M = 2.40.

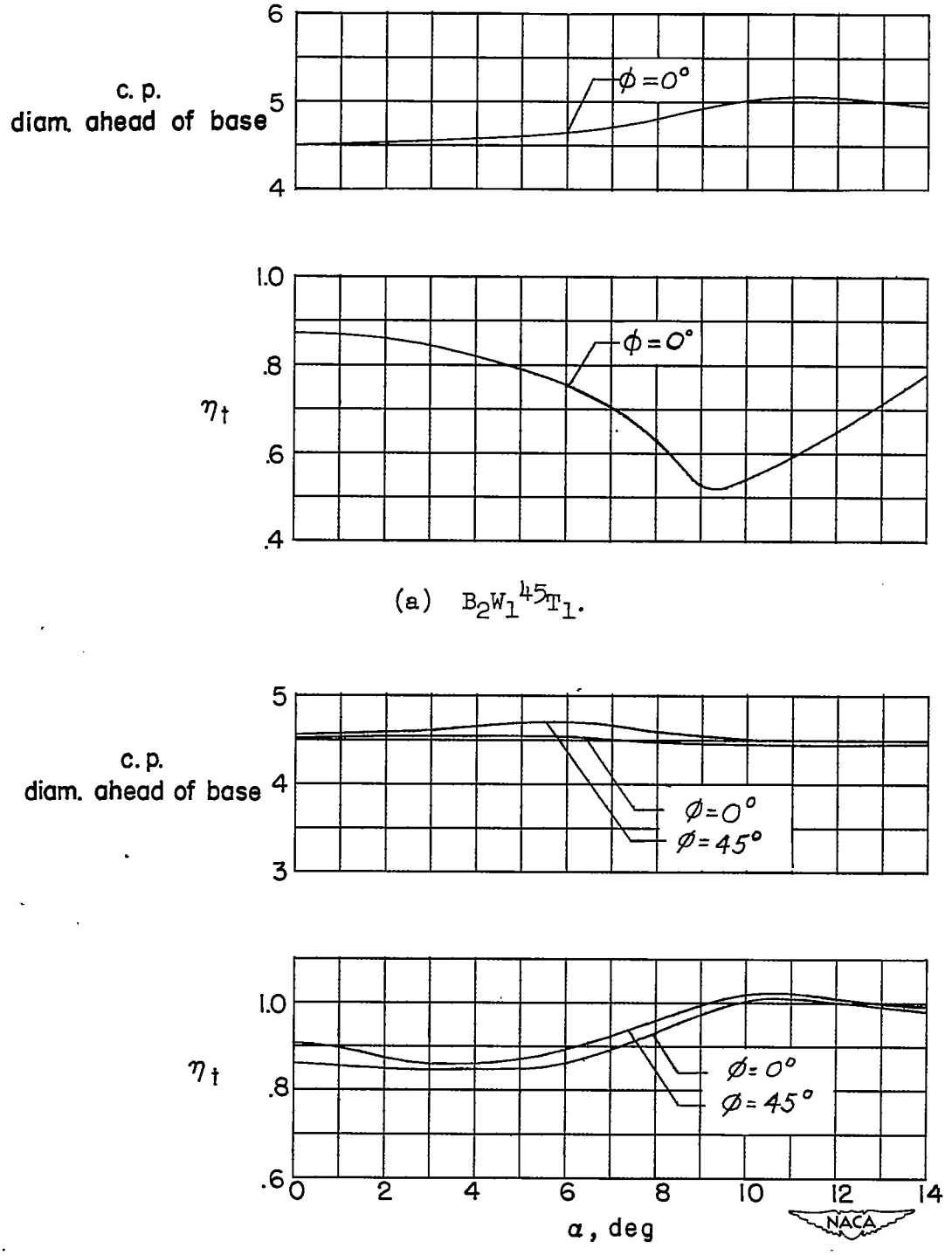

(a) $B_2W_1{}^{45}T_1$.

(b) $B_4W_{11}{}^{45}T_7$.

Figure 23.- Variation of center-of-pressure and η_t with α of BWT at M = 2.40.

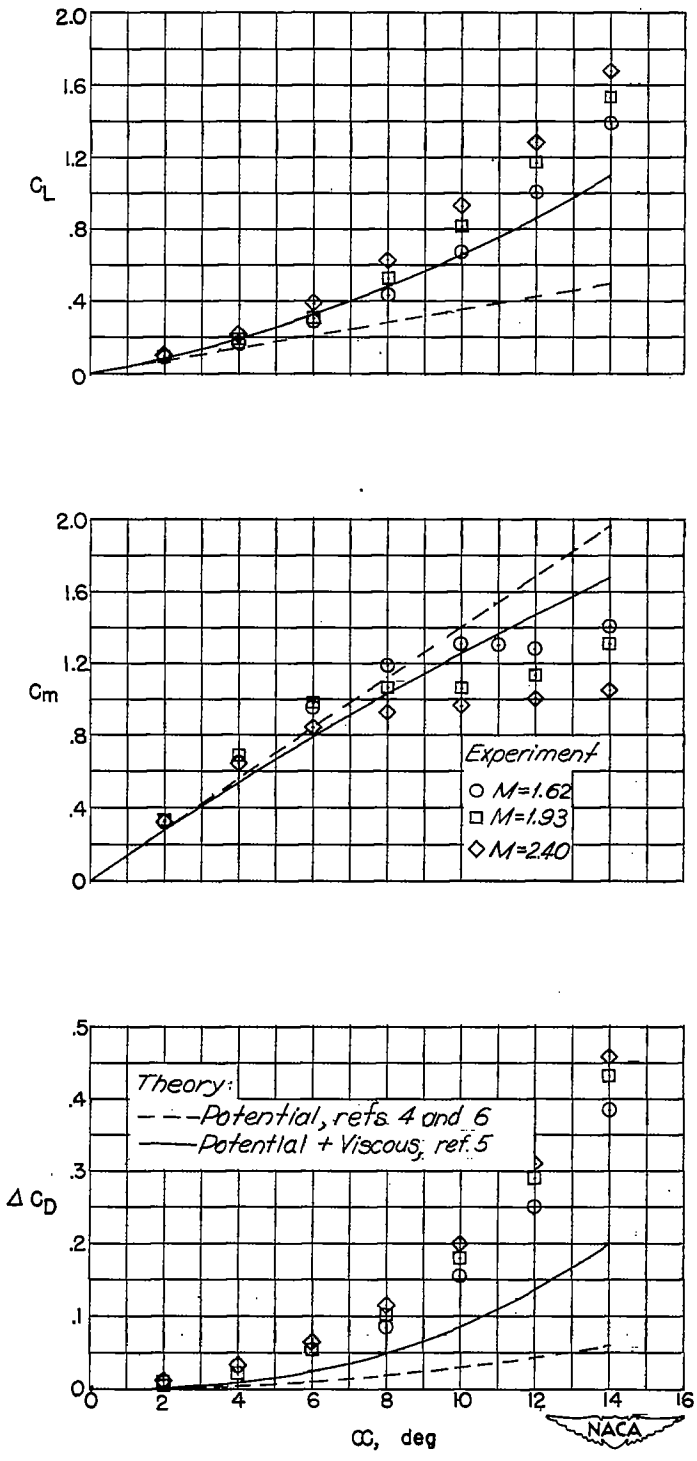

(a) B_2.

Figure 24.- Comparison of experimental and calculated lift, incremental drag, and pitching moments of B.

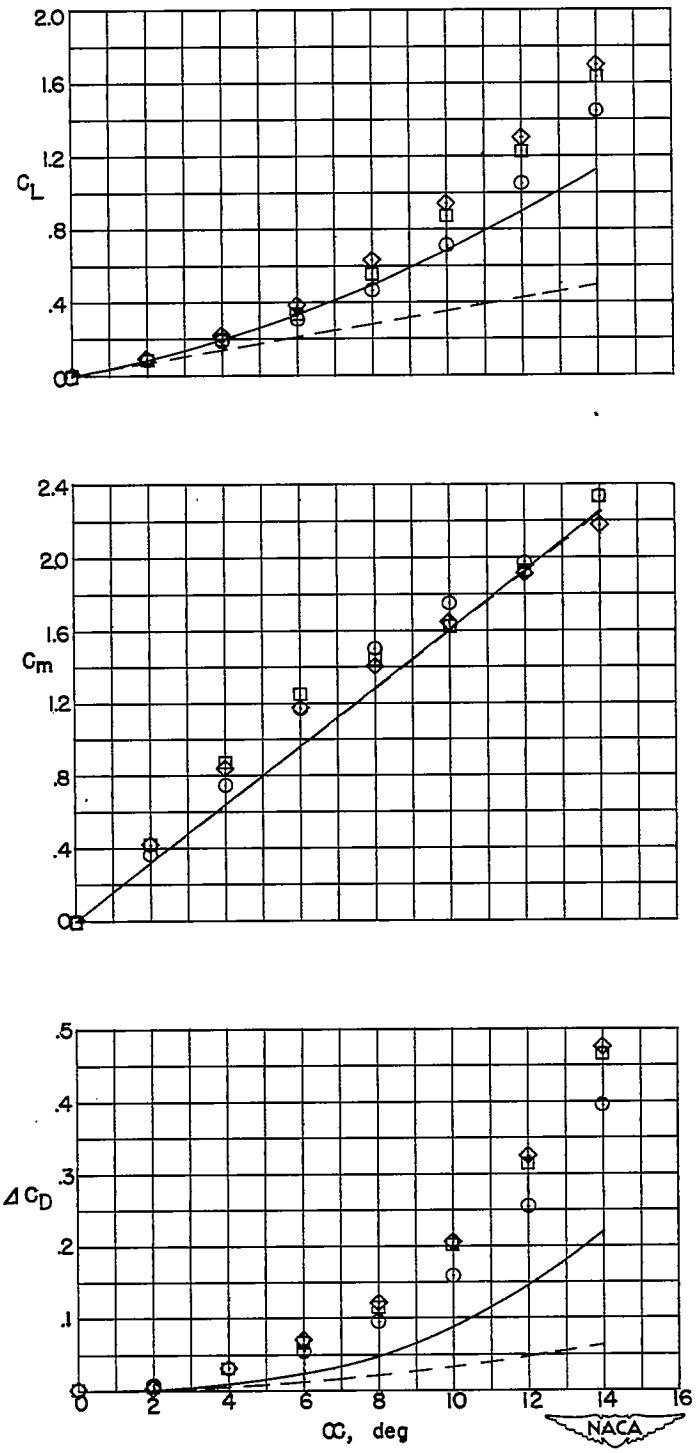

(b) B_4.

Figure 24.- Concluded.

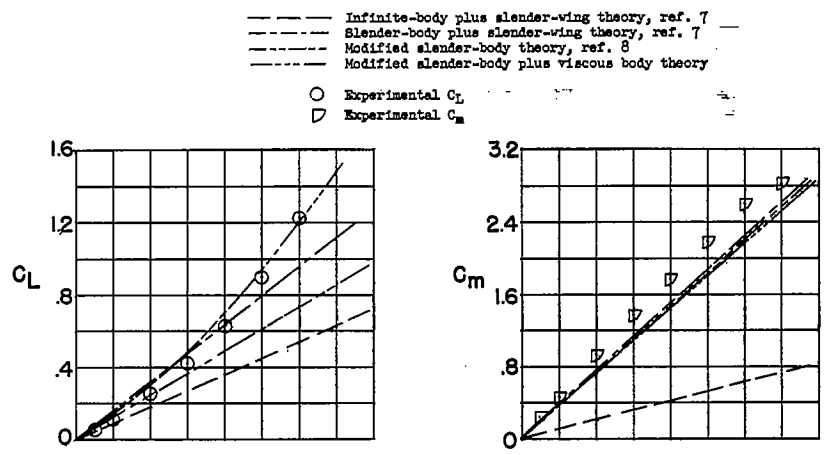

(a) $B_4W_7{}^0$.

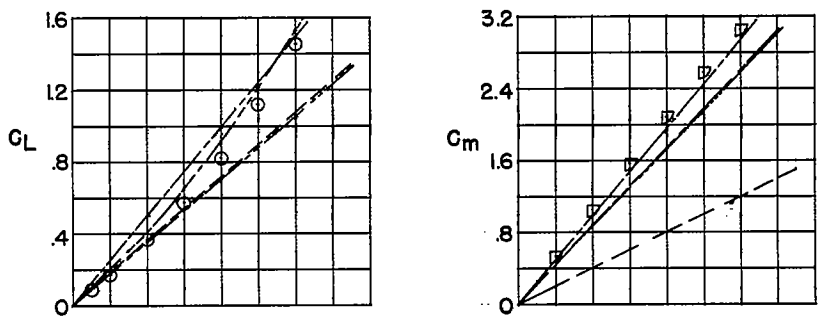

(b) $B_4W_8{}^0$.

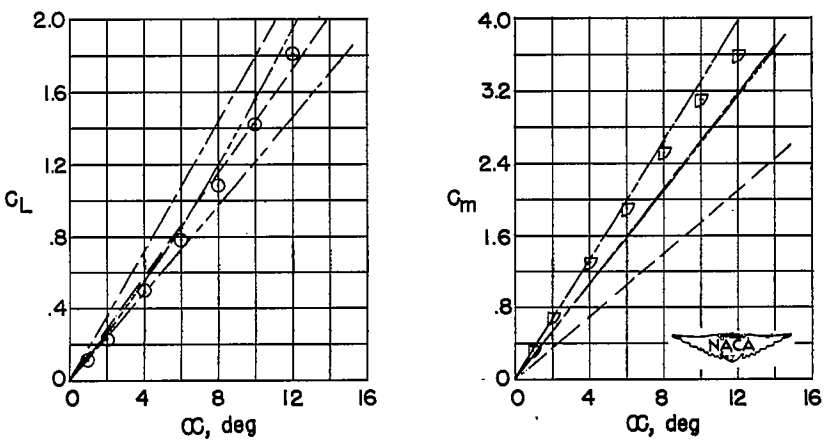

(c) $B_4W_9{}^0$.

Figure 25.- Comparison of calculated and experimental lifts and pitching moments of BW at M = 1.93 at zero roll angle.

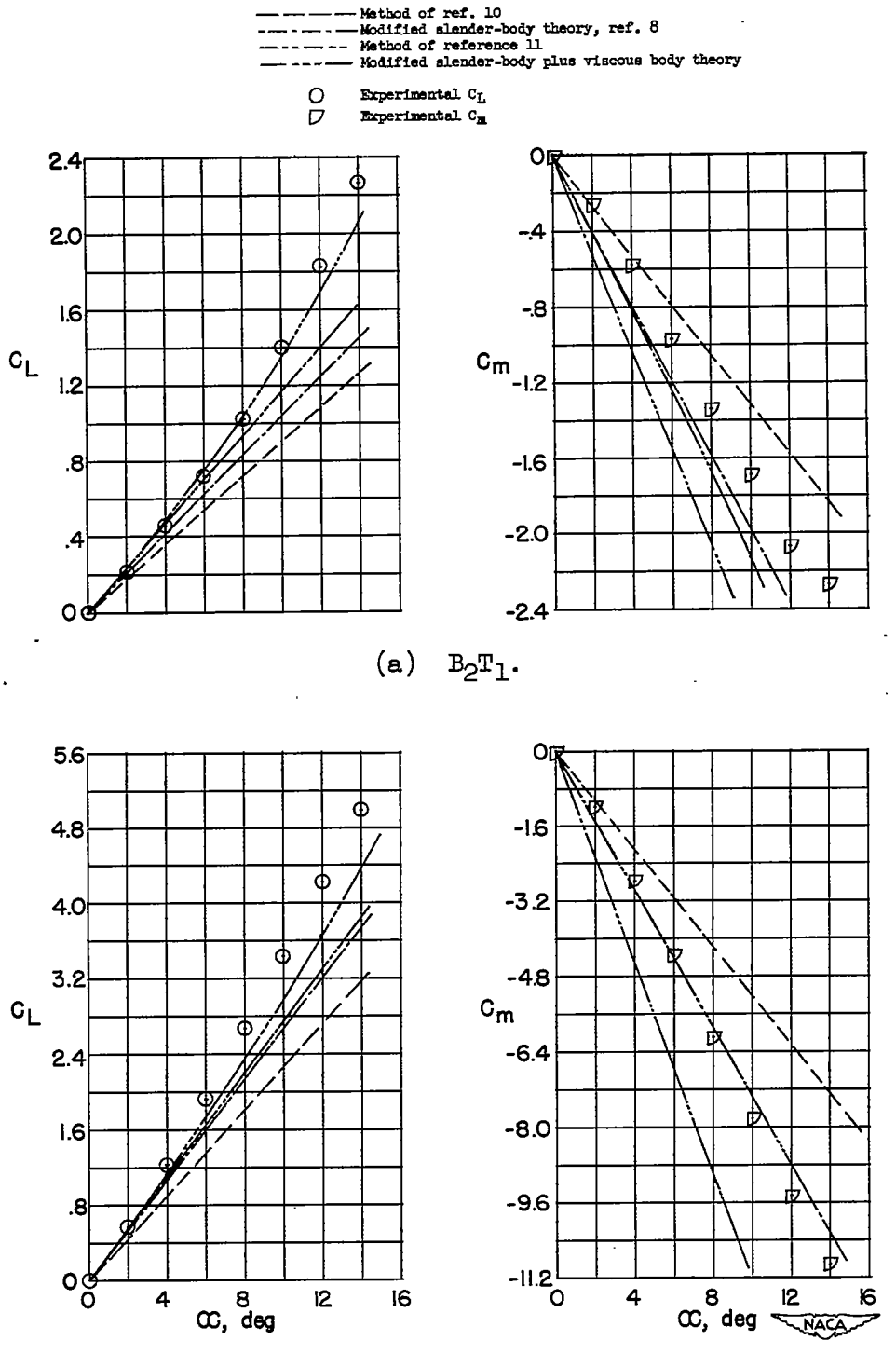

(a) B_2T_1.

(b) B_4T_5.

Figure 26.- Comparison of calculated and experimental lifts and pitching moments of BT at M = 1.93 at zero roll angle.

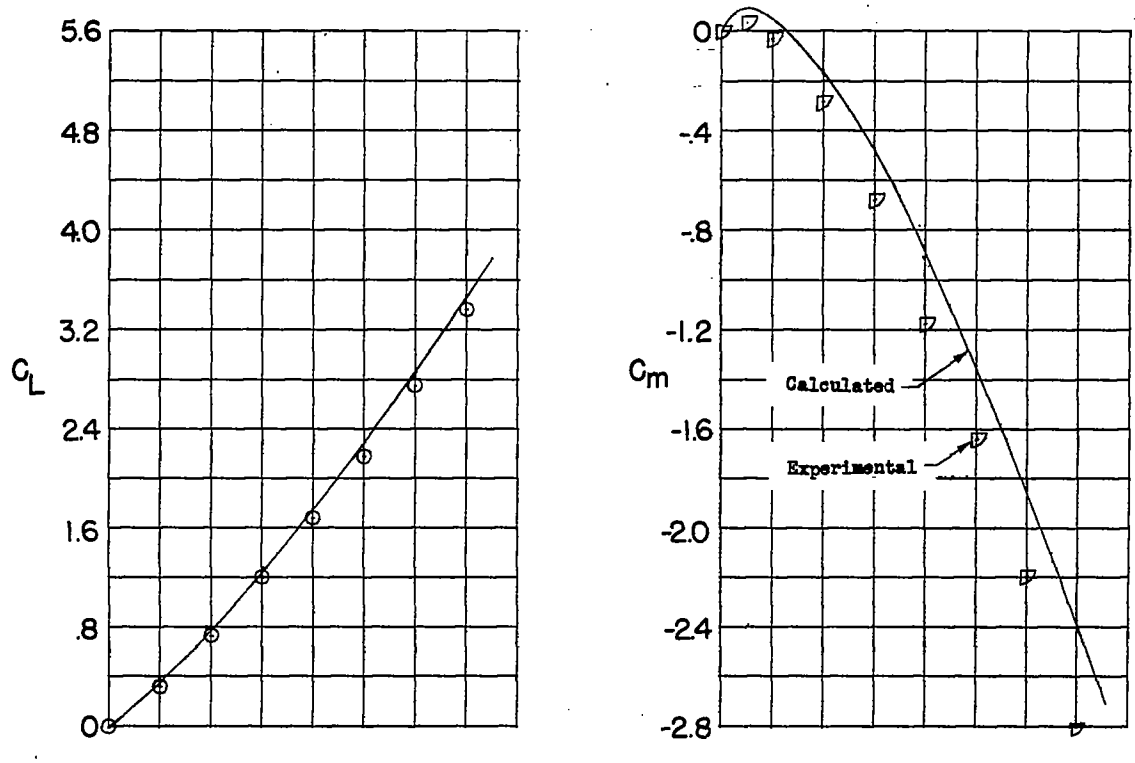

(a) $B_2W_1{}^0T_1$.

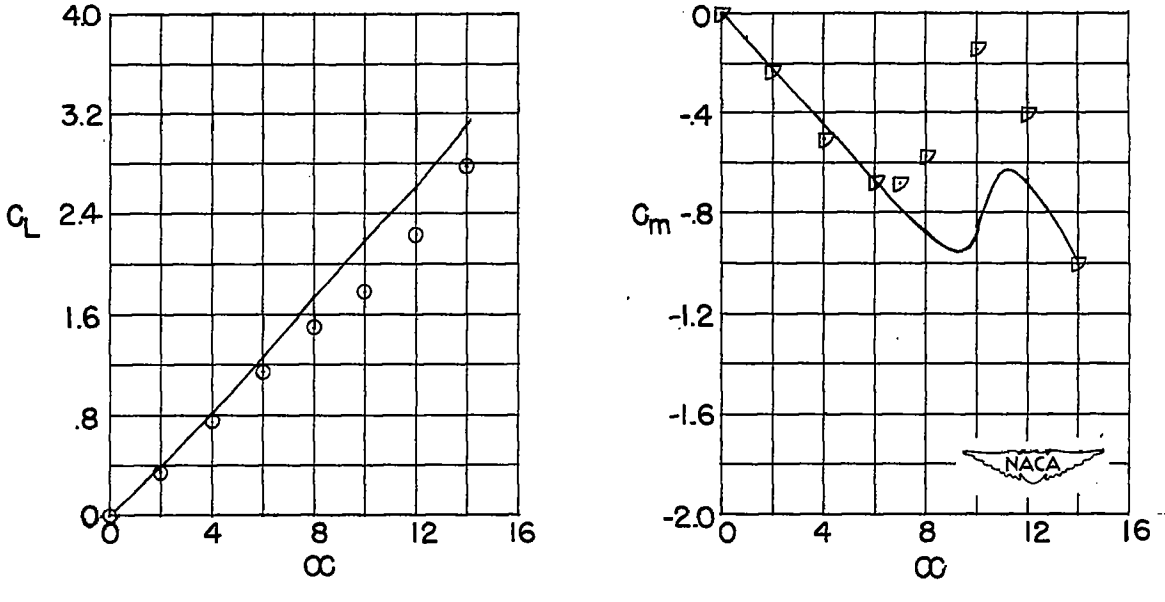

(b) $B_2W_1{}^{45}T_1$.

Figure 27.- Comparison of calculated and experimental lifts and pitching moments of BWT at M = 1.93 and zero roll angle.

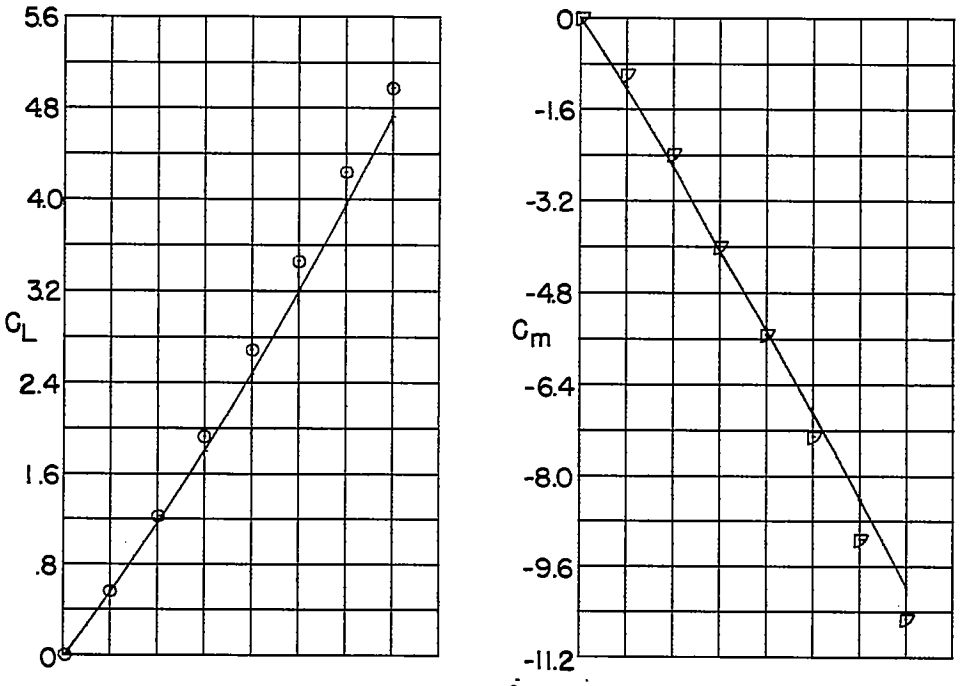

(c) $B_4W_7{}^0T_5$.

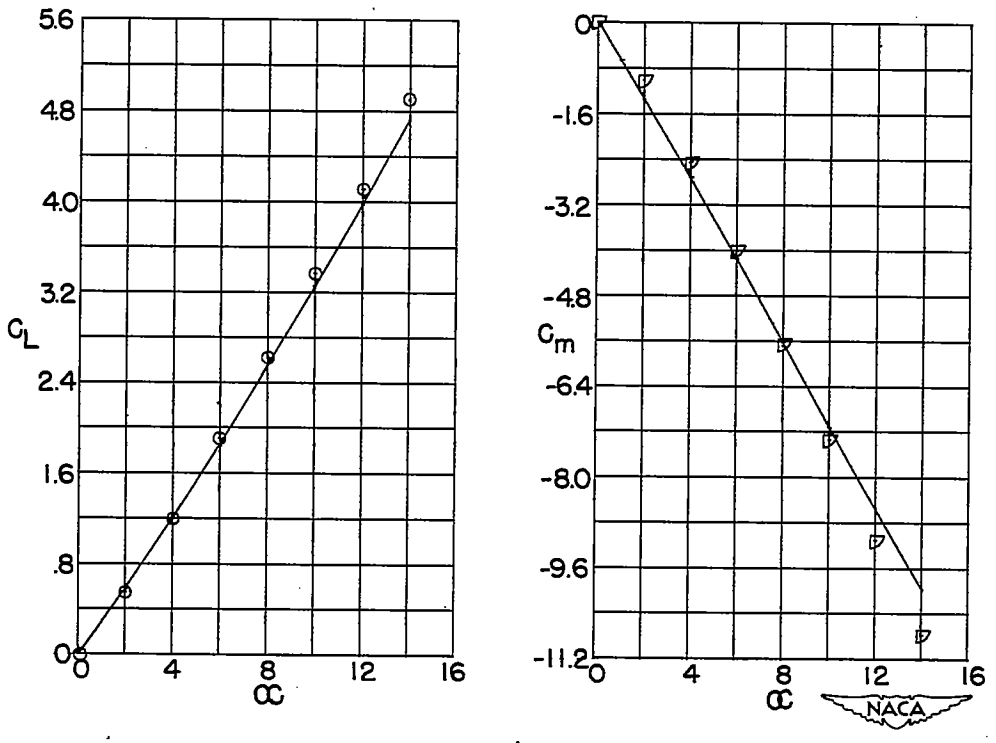

(d) $B_4W_7{}^{45}T_5$.

Figure 27.- Continued.

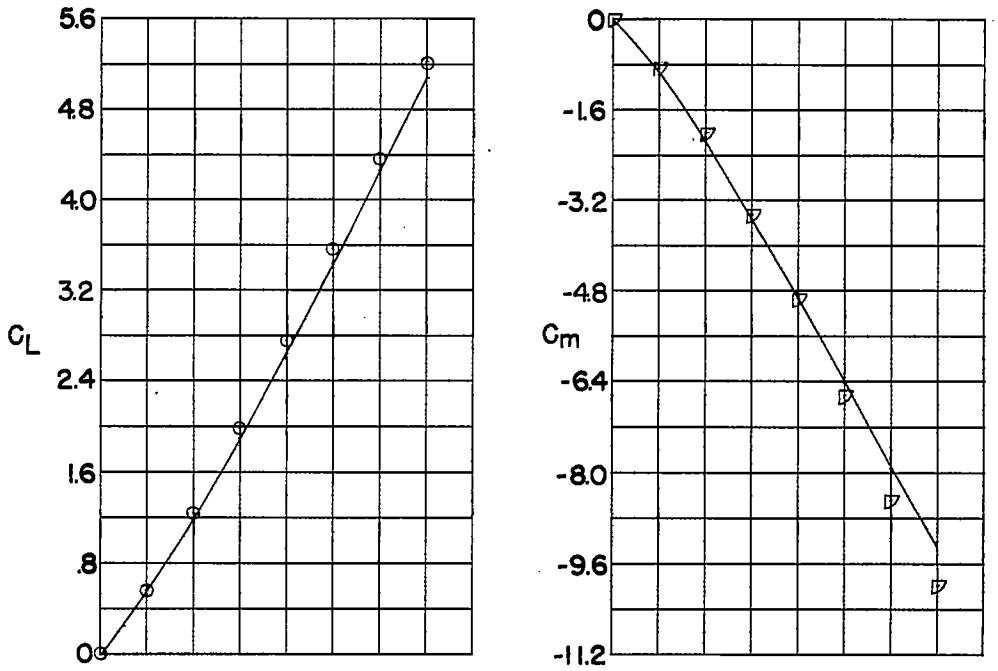

(e) $B_4W_8{}^0T_5$.

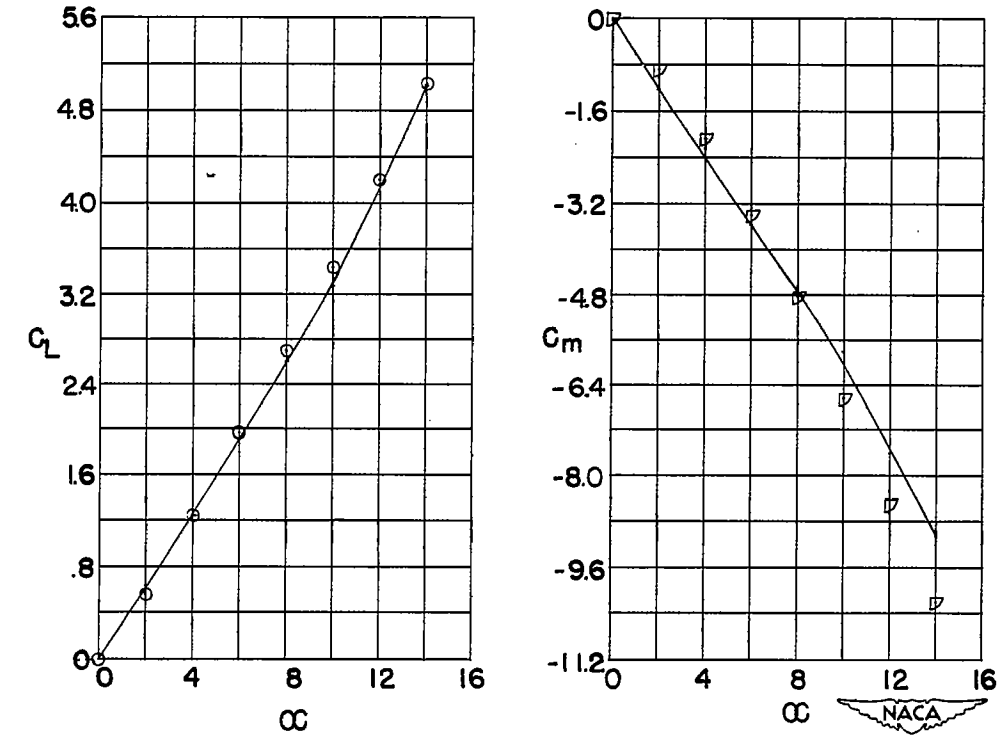

(f) $B_4W_8{}^{45}T_5$.

Figure 27.- Continued.

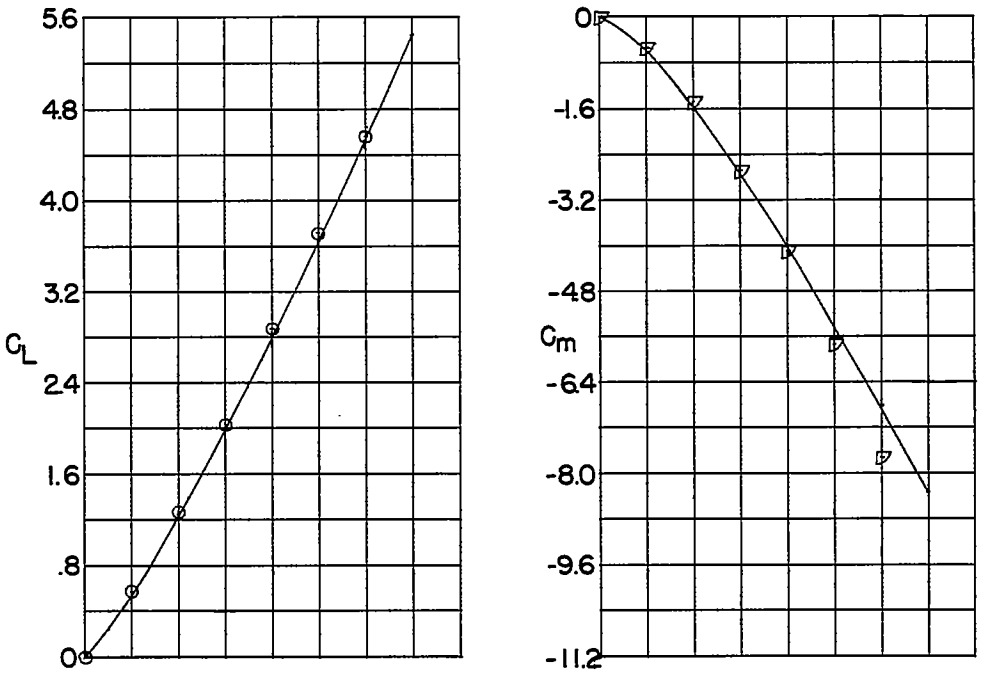

(g) $B_4W_9{}^0T_5$.

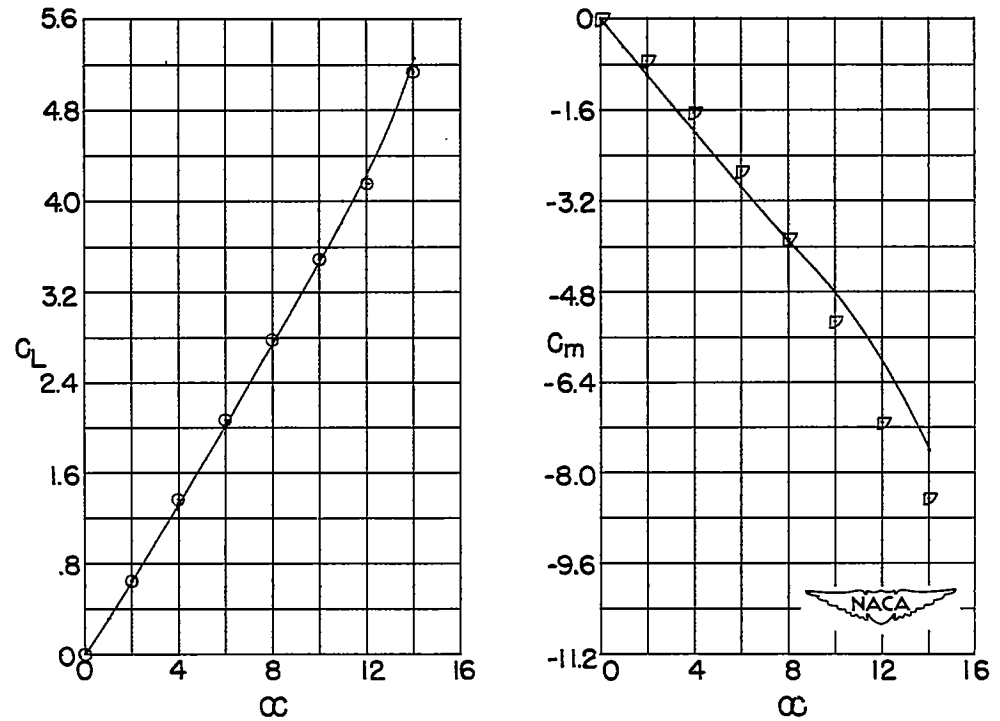

(h) $B_4W_9{}^{45}T_5$.

Figure 27.- Concluded.

[redacted]

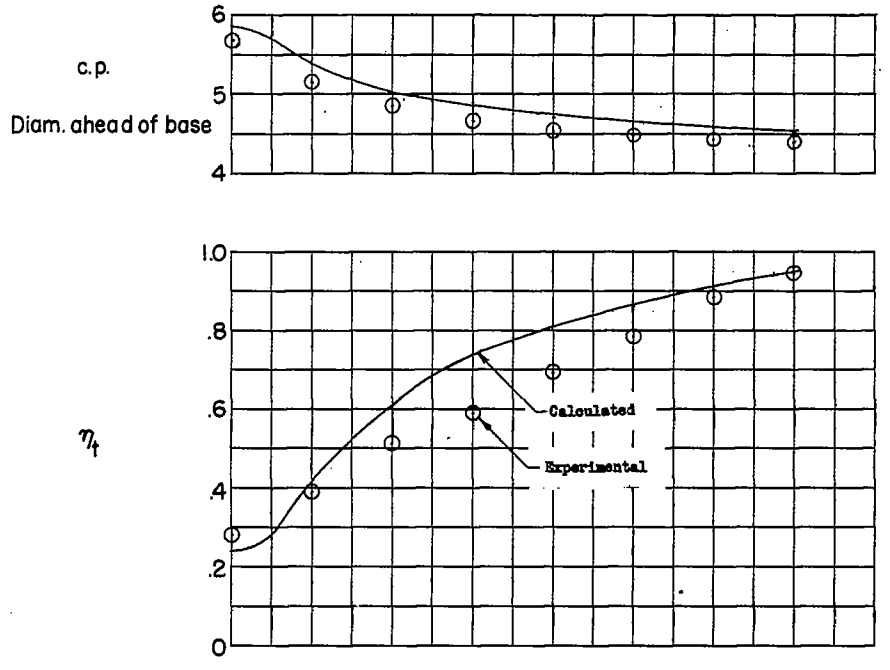

(a) $B_2W_1{}^0T_1$.

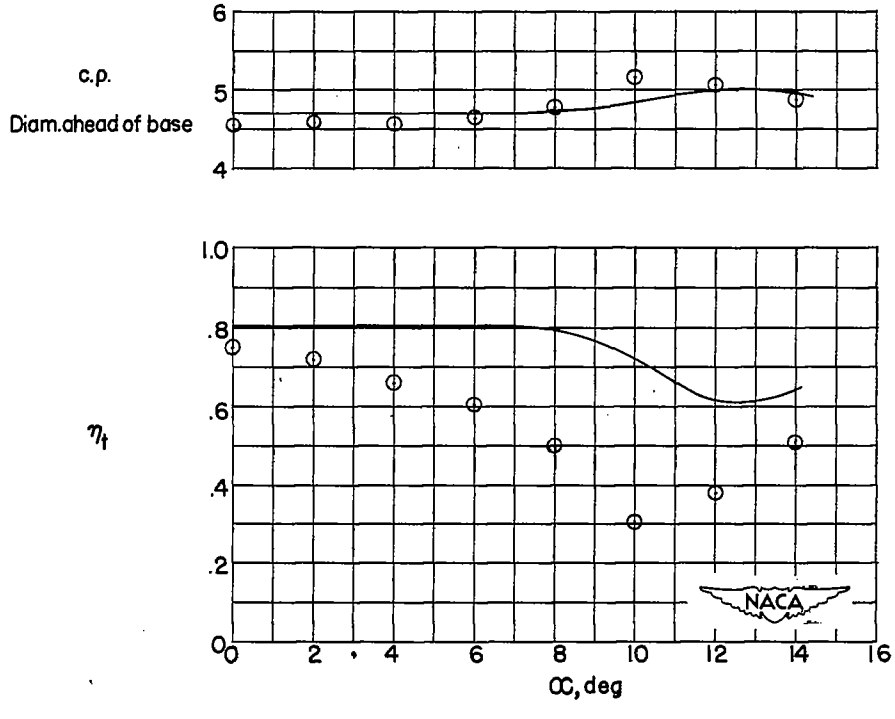

(b) $B_2W_1{}^{45}T_1$.

Figure 28.- Comparison of calculated and experimental center-of-pressure locations and tail efficiencies of BWT at M = 1.92 and zero roll angle.

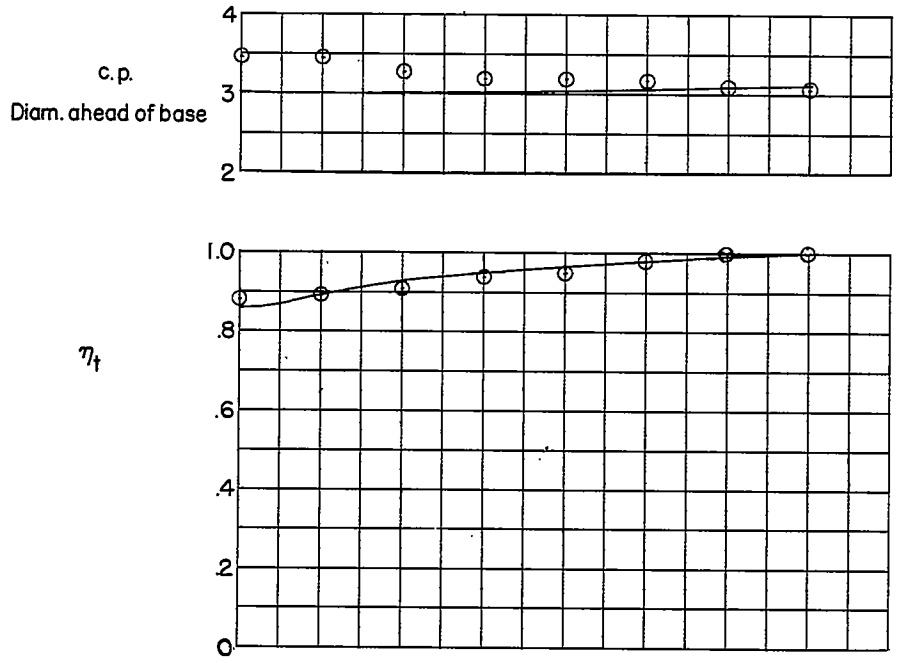

(c) $B_4W_7{}^0T_5$.

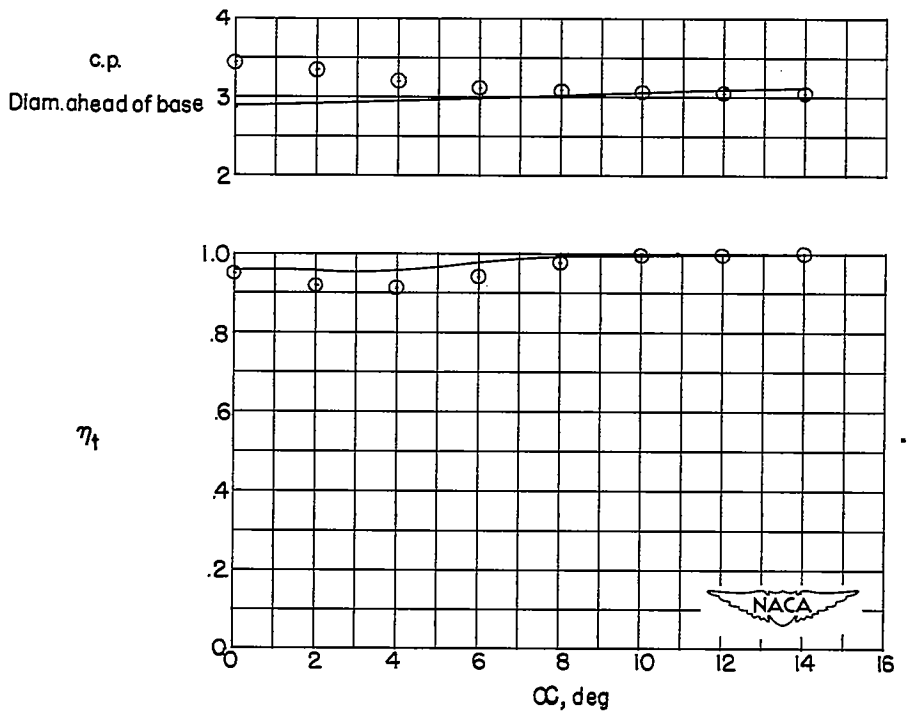

(d) $B_4W_7{}^{45}T_5$.

Figure 28.- Continued.

[redacted]

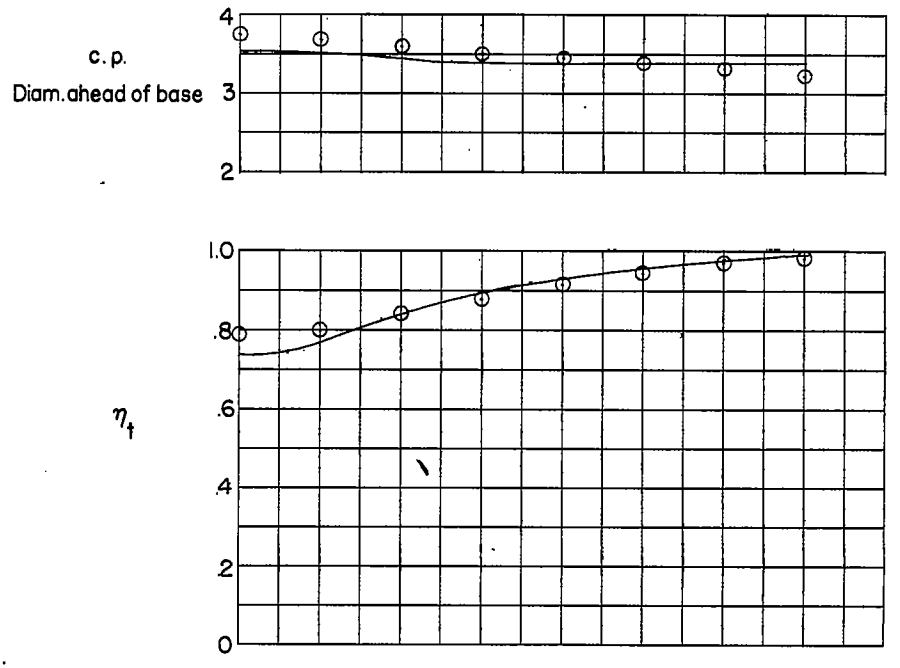

(e) $B_4W_8{}^0T_5$.

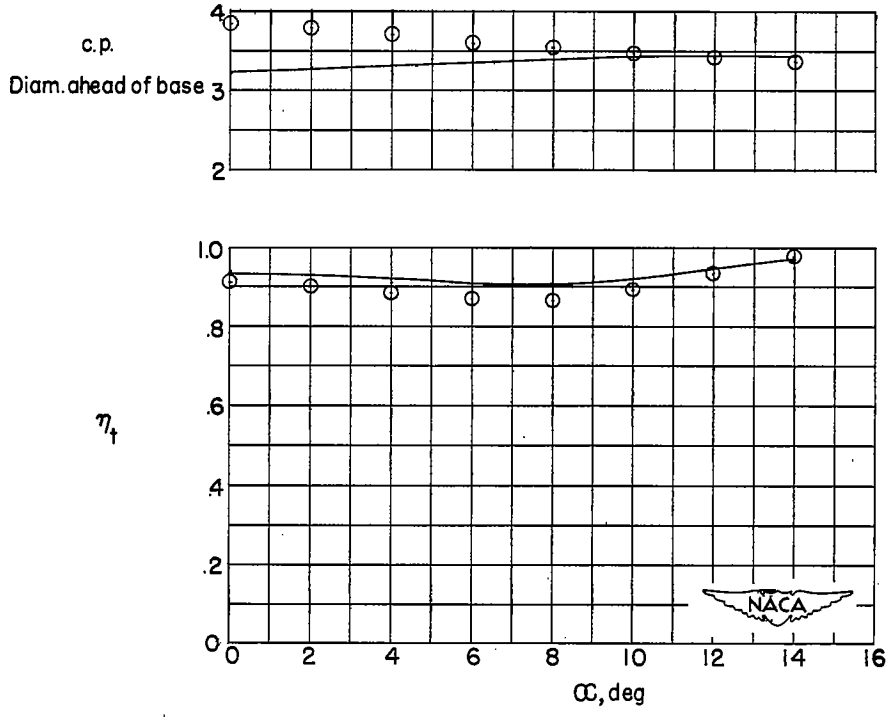

(f) $B_4W_8{}^{45}T_5$.

Figure 28.- Continued.

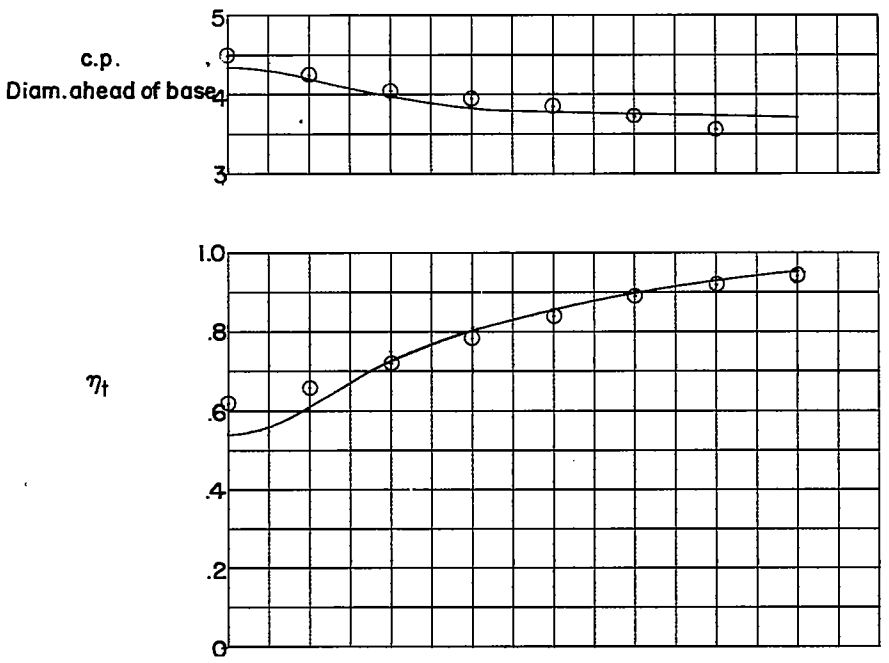

(g) $B_4W_9{}^0T_5$.

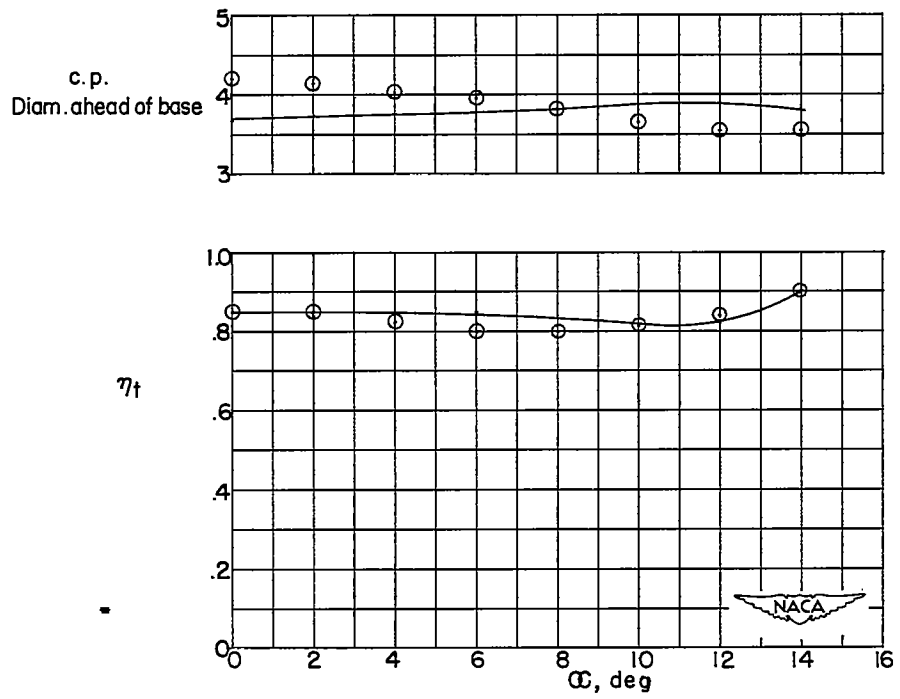

(h) $B_4W_9{}^{45}T_5$.

Figure 28.- Concluded.

[redacted]

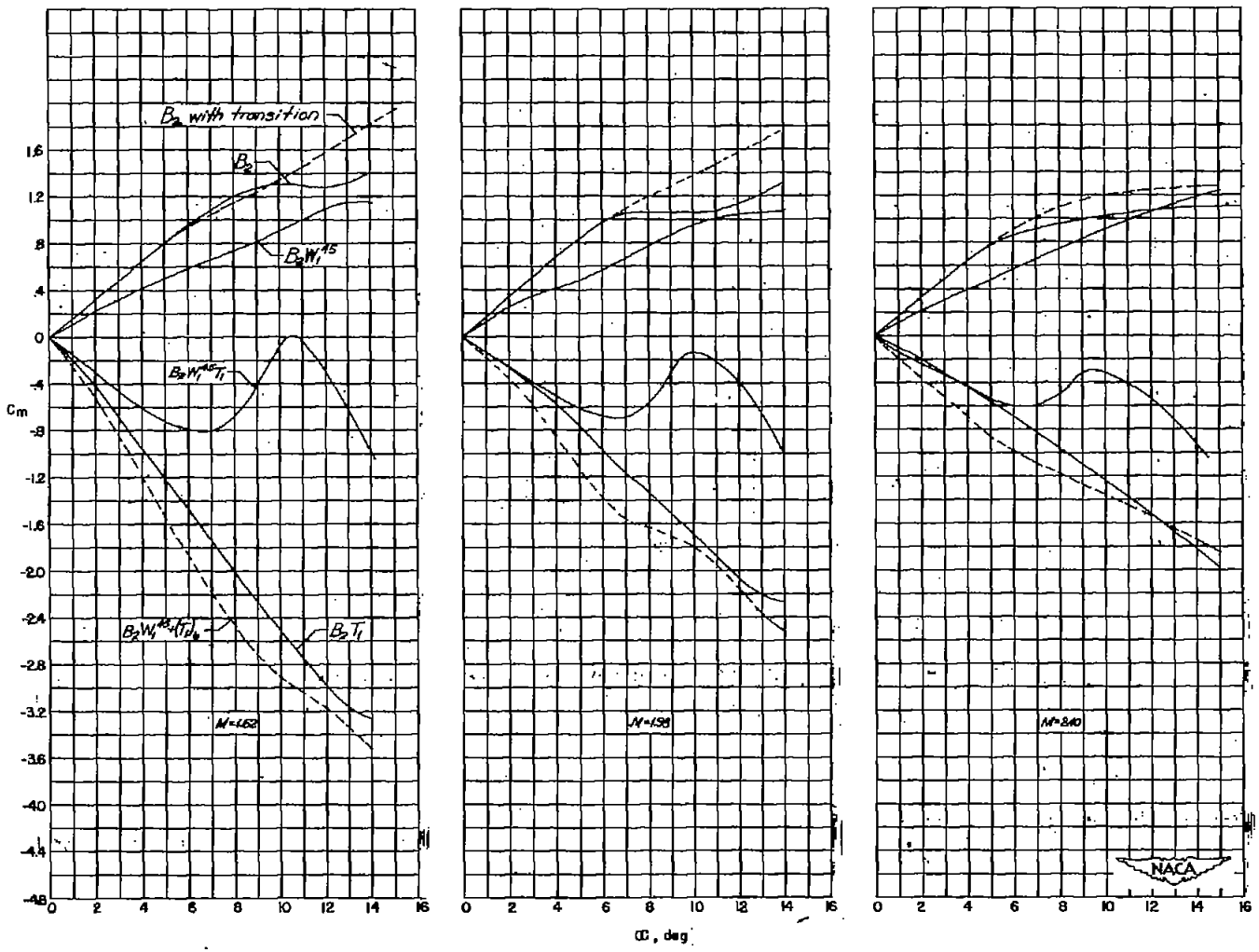

(a) $B_2W_1^{45}T_1$.

Figure 29.- Pitching moments of components and combinations of components.

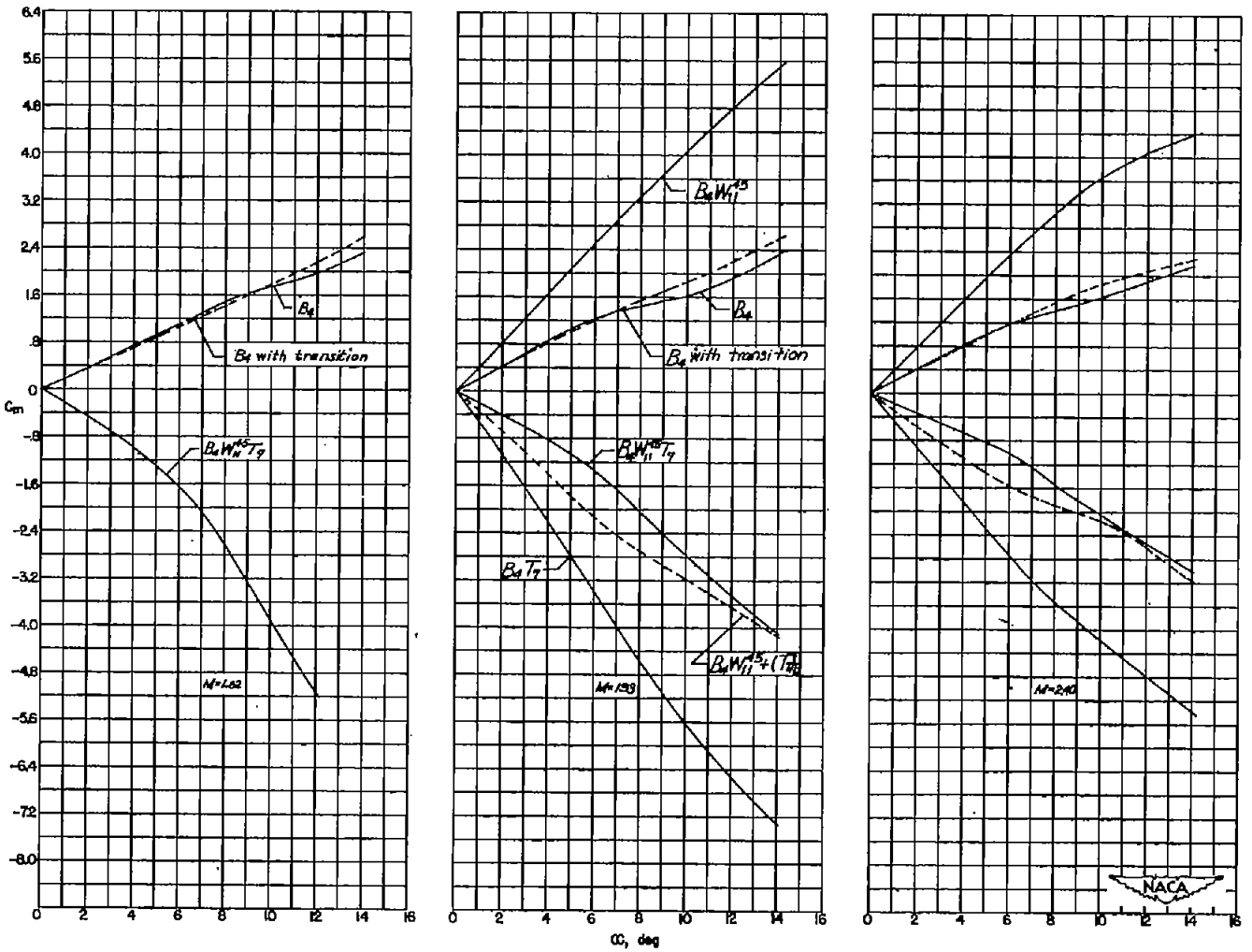

(b) $B_4W_{11}{}^{45}T_7$.

Figure 29.- Concluded.

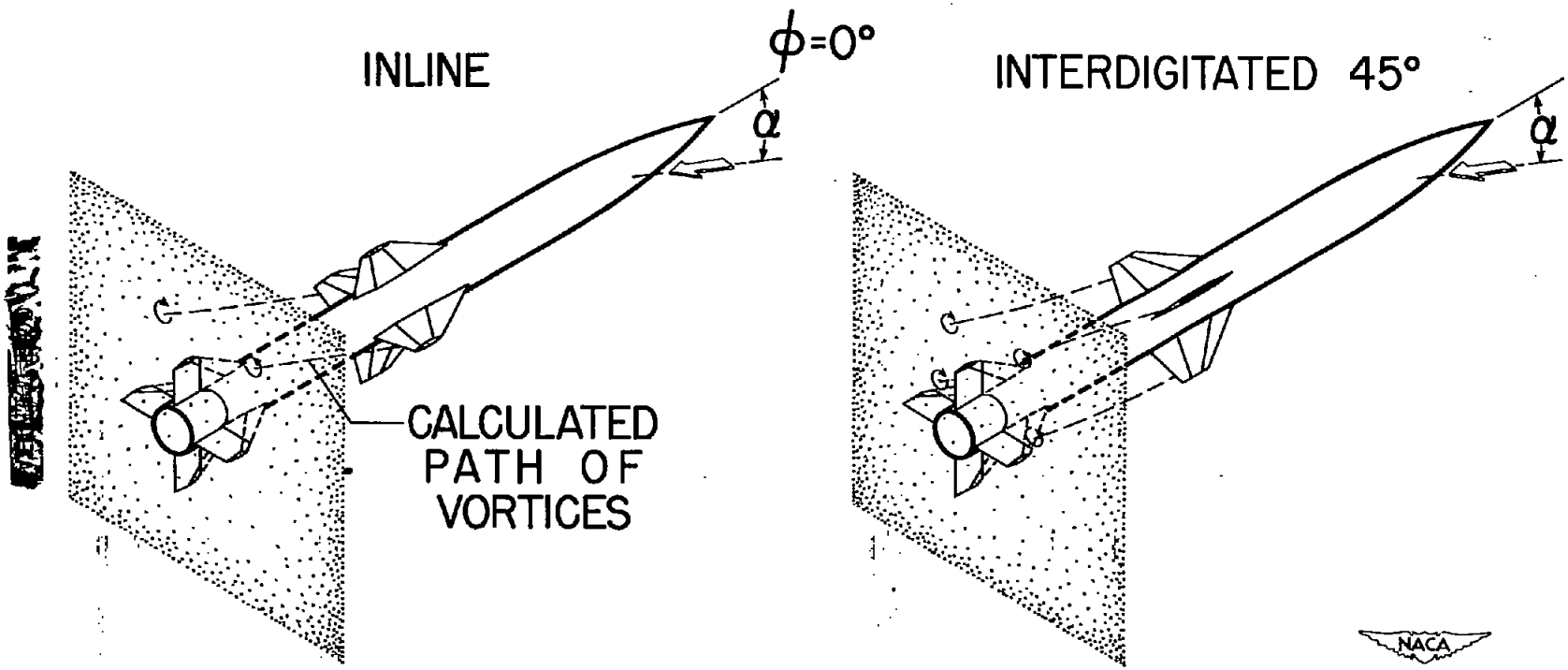

Figure 30.- Assumed vortex pattern for calculations.

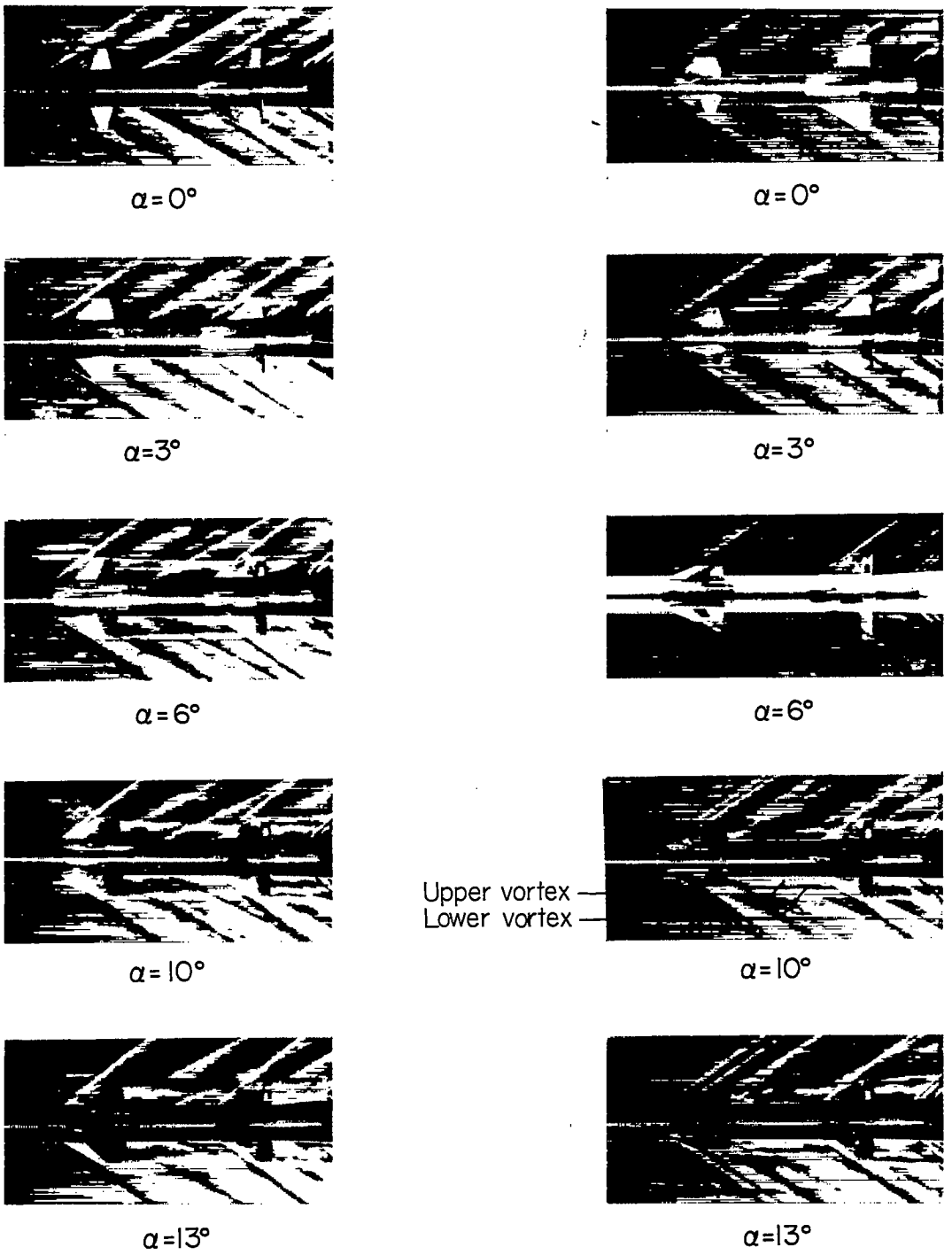

(a) $B_2W_1{}^0T_1$.

(b) $B_2W_1{}^{45}T_1$.

NACA L-75149

Figure 31.- Schlieren photographs of two missiles at M = 1.93 and zero roll angle.